An X-ray analysis of an *XMM-Newton* Sample of Compton-thick AGN

Masterarbeit
im Studiengang Physik am Lehrstuhl für Astrononmie

vorgelegt von
Annika Kreikenbohm

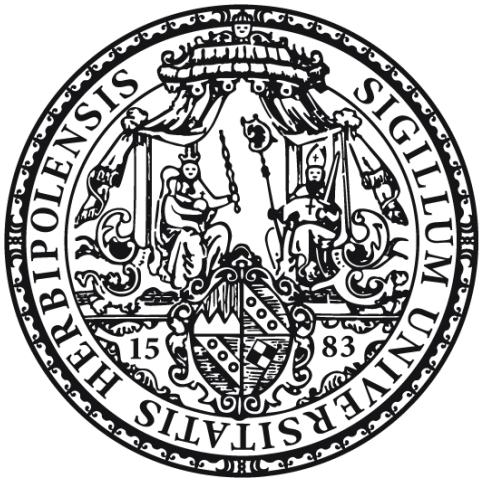

Würzburg, den 4. Februar 2013

Fakultät für Physik und Astronomie
Julius-Maximilians-Universität Würzburg

Verantwortlicher Hochschullehrer	Prof. Dr. M. Kadler
Zweitgutachter	Prof. Dr. J. Wilms

"All models are wrong!
But some are useful!"
(Box & Draper, 1987)

Zusammenfassung

In dieser Masterarbeit werden die Ergebnisse der Analyse von Röntgenspektren eines Samples von stark absorbierten Aktiven Galaxienkernen (AGN) präsentiert. Dazu wurden für jede Quelle Archivdaten von Beoachtungen des *XMM-Newton* Space Observatory der ESA reduziert und Modellierung der Spektren analysiert.
Die Röntgenanalyse des stark absorbierten AGN ermöglicht die Untersuchung der innersten Region des Galaxienkerns, da die dichte, umgebene Materie die primäre Röntgenstrahlung entlang Sichtlinie absorbiert. Das beobachtete Spektrum wird daher von Strahlung, die mit den Strukturen im Zentrum des AGN wechselwirkt, dominiert. Ein wichtiger Prozess ist dabei die Reflexion von Röntgenstrahlung an dichter Materie durch Comptonstreuung. Dadurch ergibt sich ein charakteristisches Kontinuumsspektrum sowie starke Fluoreszenzlinien, die vor allem für Eisen sehr markant sind.
Die Analyse des Bereichs zwischen 2–10 keV ergibt, dass für alle Quellen ein signifikanter Anteil der Reflexion, durch Streuung an neutraler Materie stattfindet. Diese wird im Allgemeinen mit einem neutralen, ringförmigen Torus assoziert, der das Zentrum des AGN umgibt und es entlang der Sichtlinie verdeckt. Allerdings weisen Fluoreszenzlinien von ionisiertem Eisen auch auf die Existenz ionisierter Materie hin, dessen Urspung und Verteilung noch unbekannt ist.
Von den bestehenden Theorien zur Ursache des ionisierten Linienspektrum wurden in der Masterarbeit zwei verschiedenen Möglichkeiten getestet. Einerseits die Streuung des primären Kontinuums an heißem, durch Kollisionen getriebenem Plasma, andererseits das Szenario ionisierter Reflexion, die möglicherweise von der inneren sichtbaren Oberfläche des Torus stammt. Beide Szenarien führen neben ionisierten Eisenlinien zusätzlich zu einem ausgeprägten Linienspektrum im weichen 0.3–2 keV Röntgenbereich. Die vier hellsten Quellen des Samples im Bereich 0.3–10 keV von *XMM-Newton* modelliert.Die Analyse ergab, dass die Modelle beider Szenarien Schwierigkeiten haben die Daten vollständig selbstkonsistent zu beschreiben. Ferner ist es statistisch nicht möglich, das eine Model dem anderen vorzuziehen. Die ungewöhnlich niedrigen Metallhäufigkeiten, die sich im Fall von Streuung an thermalem Plasma ergeben, deuten jedoch darauf hin, dass das Model nicht für einen signifikanten Anteil des Spektrums verantwortlich sein kann. Die wichtigsten Ergebnisse der Analyse des 0.3-10 keV Bereichs sind, dass das Spektrum aus der Wechselwirkung in einer oder mehreren Regionen mit unterschiedlichen Ionisations- und Temperaturzuständen resultiert. Außerdem kann ionisierte Reflexion einen Teil der Röntgenemission erklären und sollte in zukünftigen Analysen in Betracht gezogen werden.

Abstract

This thesis presents the analysis of the X-ray spectrum of a sample of heavily obscured Active Galactic Nuclei (AGN). The spectra for each source were reduced from archival observations performed by the *XMM-Newton* Space Observatory of ESA.
X-ray analysis of such AGN allows to probe the innermost regions of the nucleus, because the primary X-ray continuum is absorbed by highly-dense matter in the line of sight. Thus the spectrum is characteristically altered due to the interaction of the radiation with the circumnuclear matter. Using the method of spectral model fitting, it is possible to constrain the physical processes, responsible for the reprocession of the primary X-ray emission and interpret them in the context of geometry and physical conditions of the inner region.
An important process is Compton-reflection, which is the back-scattering of X-rays through Compton-scattering at highly-dense matter. It leads to a characteristic continuum with prominent fluorescence lines of iron. The analysis of the 2–10 keV energy band shows, that for all sources a significant amount of the iron line is caused by reflection from neutral matter. This is commonly associated with a putative, donut-shaped torus, which surrounds and obscures the central X-ray source from direct view. However, the line spectrum shows evidence of ionized emission, whose origin is largely unknown. There are different theories for how this ionized emission can occur. Two scenarios are tested in this thesis. The first one is the scattering scenario, where the ionized emission comes from a hot thermal plasma along the line of sight, heated by collision. The second one is the reflection scenario, which is caused by Compton-reflection of ionized material, possibly at the inner surface of the torus.
The spectrum of the four brightest sources of the sample are analyzed between 0.3-10 keV, where the line spectrum dominates over the continuum spectrum. The analysis shows that both models have difficulties to describe the whole spectrum. Furthermore, it cannot be unambiguously distinguished between the two scenarios, but the unlikely under-abundances of metals measured by the scattering model indicates, that this model most likely does not pay a significant contribution to the spectrum. The main results of the analysis between 0.3–10 keV are, that the X-ray reprocession originates in one or multiple regions of different ionization states and temperatures, and that ionized reflection may account for part of the X-ray emission seen in Compton-thick AGN.

Contents

1. Preface **3**

2. Theoretical Background of Active Galactic Nuclei **5**
2.1. Active Galactic Nuclei 5
2.1.1. AGN Taxonomy 7
2.1.2. Unification scheme 9
2.1.3. The Standard Model of an Active Galactic Nucleus 10
2.2. X-ray emission in obscured AGN 13
2.2.1. Radiative transfer 13
2.2.2. Compton-scattering and Inverse Compton-scattering 15
2.2.3. Atomic processes 16
2.2.4. X-ray reprocession 20
2.3. Compton-Thick AGN 22

3. The XCTA sample **27**

4. The XMM-Newton observatory **31**
4.1. The X-ray multi-Mirror telescopes 32
4.1.1. Point-Spread Function and Effective Area 33
4.1.2. The European Photo Imaging Camera 34
4.1.3. The Reflecting Grating Spectrometer 36

5. Data reduction **41**

6. Statistical Methods and spectral modeling **47**
6.1. Spectral modeling 47
6.2. The F-Test 48
6.3. Two-Sample Kolmogorov-Smirnov Test 48
6.4. Correlation coefficients 49

7. Analysis of the hard X-ray spectrum of the XCTA-Sample **51**
7.1. Motivation 51
7.2. Spectral Analysis 51
7.3. Results 56

7.4. Discussion of the hard X-ray spectrum . . . 68
7.4.1. The Fe Kα line complex . . . 68
7.4.2. Dependency of the Fe Kα equivalent width on the column density 69
7.4.3. The distribution of observed luminosities . . . 74
7.4.4. The X-ray Baldwin Effect . . . 76

8. Analysis of the broad band spectrum **77**
8.1. The phenomenological view . . . 77
8.2. The scattering scenario . . . 78
8.3. The reflection scenario . . . 81
8.4. Results of the broad-band analysis . . . 83
8.5. Discussion of the broad band analysis . . . 90
8.5.1. On the phenomenological model . . . 90
8.5.2. Scattering vs. Reflection . . . 96
8.5.3. Comparison with published results . . . 102

9. Summary and outlook **107**

Bibliography **111**

A. Appendix **119**
A.1. Contour Plots . . . 120
A.2. XMM-Newton EPIC PN Spectra . . . 122
A.3. Soft X-ray Emission lines . . . 129

List of Tables **131**

Danksagung **133**

1. Preface

An Active Galactic Nucleus emits radiation over the whole electromagnetic spectrum and it is commonly assumed this the extreme release of energy is powered by accretion onto a super massive black hole (e.g. Rees 1984). In the standard model, an AGN consists of a small number of ingredients: the super massive black hole, surrounded by an accretion disk, different regions of plasma and a donut-shaped circumnuclear torus, which is regarded responsible for the anisotropic emission of AGN (e.g. Bianchi et al. 2012).
AGN are sources of strong X-ray emission, which is assumed to be produced in the corona of the accretion disk. The primary X-ray emission is reprocessed in the circumnuclear matter and carries imprints of the geometrical and physical properties of these structures. The relevant processes responsible for X-ray reprocession are basically known, however, the detailed structure of the circumnuclear region and its effects on the X-ray spectrum is still not fully understood. Recent studies show, that the standard model of an AGN is too simple.
Compton-thick AGN play a key role in the study of the inner regions. The primary X-ray continuum is heavily obscured in these sources, most likely by the putative torus, thus allowing a clear view on the reprocessed spectrum. In order to study the properties and mechanisms of X-ray reprocession directly. This thesis concentrates on analyzing the X-ray spectrum of a sample of Compton-thick AGN in order to analyze the contributing physical processes and tests for two possible scenarios, which can be responsible for the observed spectrum.
First, Chapt. 2, gives an introduction into the theory of AGN and the physical processes, which are relevant for the understanding of the X-ray spectrum and X-ray reprocession. Statistical methods used during the analysis as well as the *XMM-Newton* space observatory are explained in Chapt. 6 and Chapt. 4, respectively. The *XMM*-Compton-thick-AGN (XCTA) sample is defined in Chapt. 3, which includes the sample selection criteria as well as the data reduction of the *XMM-Newton* data for all sources. Chapt. 7 focusses on the analysis of the 2–10 keV spectrum and the results of the spectral fitting are discussed in Sect. 7.4. In Chapt. 8 the four brightest sources of the sample are analyzed in the 0.3–10 keV band. Besides the definition of a phenomenological model, which gives information about the basic components of the spectrum, two scenarios (the scattering and reflection scenario) are defined and tested. The results are discussed in Sect. 8.5. Furthermore, they are put in context with previous works for each source. Finally, Chapt. 9 summarizes the results and gives an outlook on possible future projects.

2. Theoretical Background of Active Galactic Nuclei

2.1. Active Galactic Nuclei

The expression active galactic nucleus (AGN) refers to the center of a galaxy which exhibits powerful energetic phenomena in the central region, which cannot be directly associated with the stellar emission of the host galaxy. The inner regions of AGN present extreme physical conditions which classify them as unique laboratories for a variety of different fields of physics. First indications for a new type of galaxies was found by Carl Seyfert 1943 who systematically studied galaxies with optical emission lines of highly excitated elements. He also found that those galaxies present high surface brightnesses in the core region, which was later estimated to be smaller than 100 pc. Fig. 2.1 shows three optical images of the AGN NGC 4151. From left to right the images were taken with increasing exposure time. In Fig. 2.1 a) only the compact and bright core is visible. The host galaxy is too weak to be detected and is only observed for long exposure times (Fig. 2.1 c).
Assuming gravitational boundaries of the emitting gas, the central region has an energy density corresponding to a super massive black hole (SMBH). The high luminosity and short timescales of flux variability support their existence in the center of the AGN with masses ranging from 10^6 up to 10^9 solar masses (Peterson 1997). Accretion onto SMBH and re-procession of the intrinsic radiation by surrounding matter is nowadays a widely accepted explanation for the energetic emission (e.g. Rees 1984, Rees & Volonteri 2007). Even though the basic mechanism is thought to be the same, AGN present a wide variety of observational properties that led to the division into several subclasses.
The classification scheme of active galactic nuclei is based on observed phenomenological and spectral properties, e.g. luminosity or emission lines in the optical spectra. A first division is done according to their radio-loudness R, which expresses the ratio of the radio flux at 5GHz to the optical flux in the B-band (Kellermann et al. 1989). Further sub-classes arise according to different spectral properties in the optical band. But a classification of a single object should be taken with a grain of salt with respect to a considered energy range and observational method. Furthermore AGN may evolve from one class to another as their power can be highly variable and different components might dominate the emission in different states, which makes classification even more complex. Despite the diversity there are common properties observed in the majority of AGN.

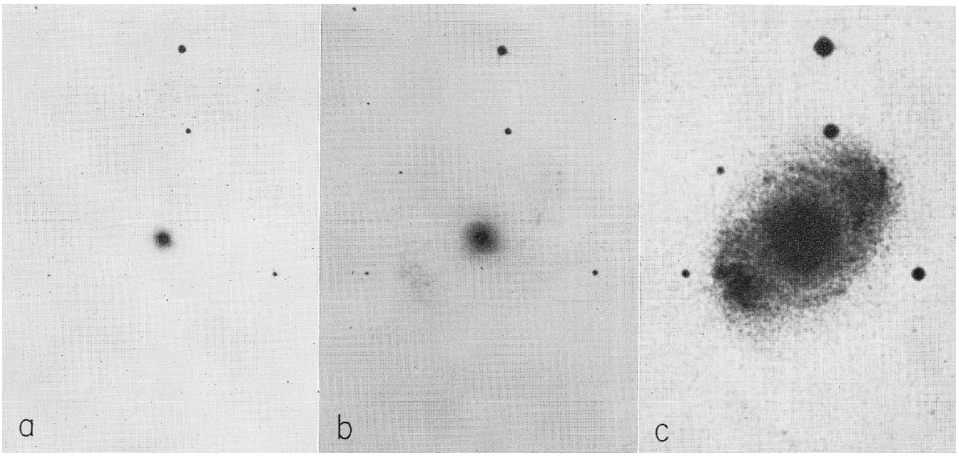

Figure 2.1.: Optical images of NGC 4151 with increasing exposure times from left to right. Credit: Morgan (1968).

For example, contrary to normal galaxies which have a rather narrow spectral energy density (SED) mainly in the optical and UV band, AGN show a very broad SED (e.g. Elvis et al. 1994) from radio up to γ-rays with similar emission of energy per frequency range (see Fig. 2.2). They are amongst the most luminous objects with bolometric luminosities ranging from 10^{42} to 10^{47} erg/s. Compared to normal galaxies they exhibit high X-ray/optical-flux ratios and as for Quasars and Blazars (see Sect. 2.1.1) strong radio emission. The continuum shows variability in flux across the whole electromagnetic spectrum as well as high polarization (up to 16% in the optical band, Antonucci et al. 1994). On the basis of observational evidence Antonucci (1993) summarized a unified model, which over the years has developed into the *standrad model* of AGN. It proclaims that all AGN are intrinsically of the same structure and for a given intrinsic luminosity spectral differences are solely related to different orientation to the line-of-sight. This is because the central region is surrounded by an optically -thick, rotationally symmetric torus, which obscures radiation from the central region, when seen from large inclination angles, while spectra of objects seen from small angles also include radiation from the central region. Even though the model differs between AGN with strong radio emission and those which exhibit weak radio emission, the strong radio emission is treated as an added feature of radio loud AGN to the radio quiet structure. Despite its simplicity the unified model is able to explain basic spectral differences of AGN on a general view, but recent studies suggest a more complex structure of the central region and extensions of the unified model (e.g. Nenkova et al. (2008) or Elitzur & Shlosman (2006)) with additional parameters like the covering factor of the obscuring material, or the accretion disk.

The following Sect. 2.1.1 will give a brief overview of AGN types, and their unification scheme in Sect. 2.1.2. Sect. 2.1.3 explains the standard structure of an AGN based on the unified model. If not stated otherwise all information of this chapter is based on the

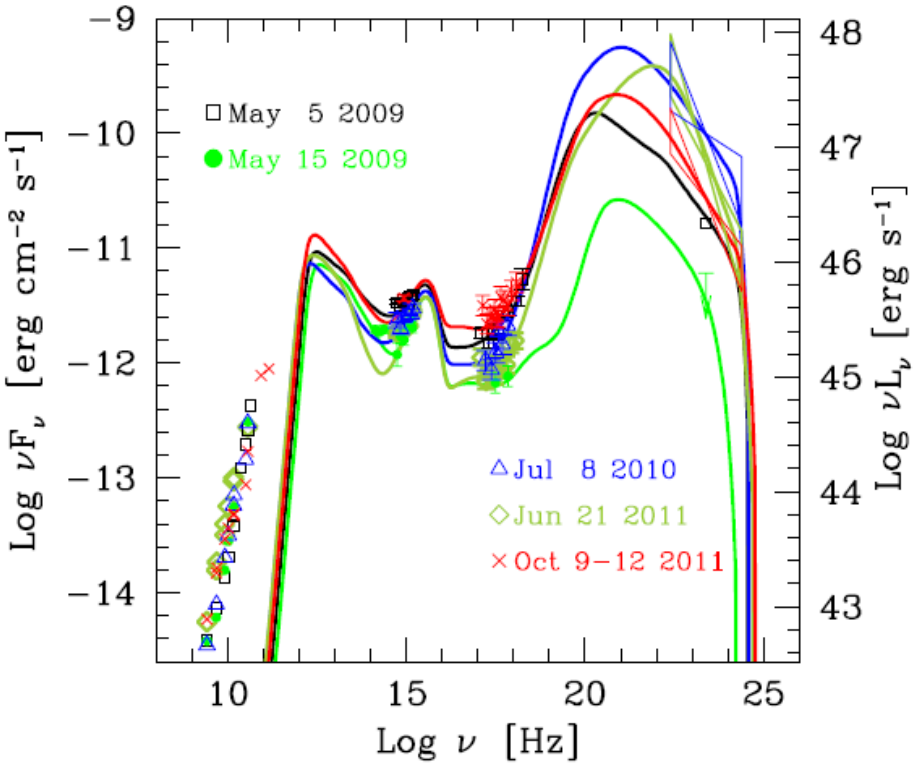

Figure 2.2.: Spectral energy distribution of the AGN PMN J0948+0022. Credit: Abdo et al. (2009).

textbooks Krolik (1999), Peterson (1997) and Schneider (2008).

2.1.1. AGN Taxonomy

A first sub-division is according to the radio-loudness R of the AGN (Kellermann et al. 1994). Radio-strong AGN with R$\geq$ 10 are called "radio-loud" (RL) and present powerful relativistic outflows, called jets, while radio weak sources with R$\leq$ 10 are called "radio-quiet" (RQ). It is assumed that radio-quiet AGN also carry a jet that is, however, much less powerful and therefore in general hard to detect. In addition, optical emission line properties mark a second distinctive feature. AGN with only narrow allowed and forbidden lines (with Doppler width of 200–700 km s^{-1}) from a hot gas and a weak continuum are classified as type 2 AGN, whereas type 1 AGN present both narrow as well as broad emission lines (with Doppler widths $\leq$ 500km s^{-1} up to a few 10^4km s^{-1}from hot, fast moving gas and a bright continuum. A third class may be defined as a type 0 with unusual optical spectra. In the following the most common AGN classes are briefly described.

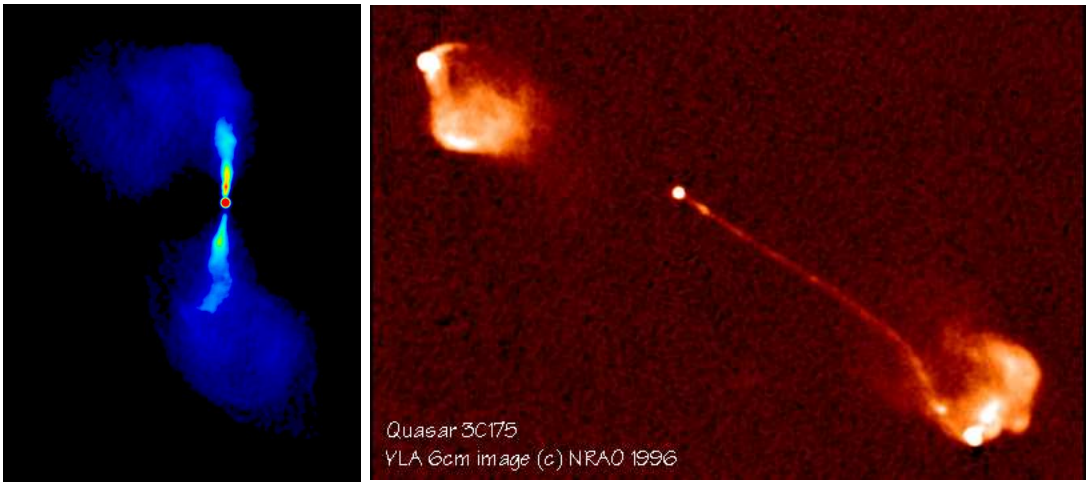

Figure 2.3.: Left panel: typical FRI AGN 3C271 (Laing & Bridle 1987). Right panel: typical FRII AGN 3C 175. Credit A. Bridle.

Seyfert Galaxies Seyfert Galaxies are radio-quiet and have relatively low luminosities compared to Quasars (e.g. Koehler et al. 1997) and their host galaxy is observable. Seyfert are known to be hosted predominantly by Spiral Galaxies, with bright central regions. They are divided in the two subclasses Seyfert type 1 and type 2. In the development of a unified model for AGN Seyferts played a key role, because polarized broad emission lines, that were detected in the Seyfert type 2 NGC 1068 (Antonucci & Miller 1985) gave first evidence for a similar central engine with a hidden broad line emitting component in type 2 AGN.

LINER (Low-Ionization-Emission-Region) Those AGN have an optical spectrum which is very similar to the ones of Seyfert 2 galaxies, but with a weaker continuum and relatively strong low-ionization emission lines. LINERs belong to the class of low-luminosity AGN and are typically radio-quiet.

Radio Galaxies AGN which exhibit high radio emission and carry a powerful jet, seen at large viewing angles with respect to the line-of-sight, are called radio galaxies. There are two sub-classes, Narrow-Line Radio Galaxies (NLRG) and Broad-Line-Radio Galaxies (BLRG), equivalent to the Type 1 and 2 classification in Seyferts. Based on their radio morphology they are sub-divided according to Fanaroff and Riley's classification (Fanaroff & Riley 1974a), which is based on the relative position of regions of high or low surface brightness in the lobes and cores of the radio source. FRI Radio Galaxies present a two-sided jet with highest surface brightness in the center, that decreases with distance. On the other hand, FRII Radio Galaxies show luminous hot spots in their lobes, while only a one-sided jet can be observed. Even though in absolute terms the core and jet are brighter than in FRI RG, in relative terms with respect to the hot-spots they are fainter.

Blazars Blazar combine radio-loud objects with a compact radio morphology and highly variable continuum. The radio structure indicates a powerful jet seen at small viewing angle ($\leq 5°$). Many of them are strong γ-ray emitters (Mukherjee et al. 1997) and depending on their phase they either present weak emission lines in the optical or a powerlaw-dominated spectrum. They comprise BL lac objects, Optically Violently Variable (OVV) and Flat-Spectrum Radio Quasars (FSRQ).

Quasars The term QSO or Quasar (Quasi Stellar Objects or Quasi Stellar Radio sources) historically refers to strong radio sources with unresolved (star-like) optical counterparts. They are among the most luminous objects and mostly found at high redshifts, which is however a selection effect due to their high luminosity. They feature a rich (star-like) emission line optical spectrum, but exhibit a higher luminosity than Seyfert galaxies. Hence they were called QSO/Quasar. Quasars are found to be both radio-loud and quiet. Nowadays, a Quasar is a compact or point-like source which presents a Seyfert-like optical spectrum. Since the classification puts no constraints on the radio-loudness there are both RL- and RQ Quasars and QSOs.

2.1.2. Unification scheme

First unification models for radio-quiet AGN were developed by Rowan-Robinson (1977), Lawrence & Elvis (1982) and Antonucci & Miller (1985), which where later reviewed and extended for radio-loud AGN by Antonucci (1993). The latter assumed that radio-loud AGN are intrinsically radio-quiet AGN but with an additional component of a jet responsible for the high radio emission. Based on this assumption the main goal of the unified model was the unification of type 1 and 2 AGN. In his model Antonucci presents a simple approach to organize the AGN zoo by saying that observed differences in the optical spectrum are solely effects of anisotropic, but rotationally symmetric radiation in AGN and different orientations from the line of sight with respect to the rotation axis of the accretion disk, i.e. the inclination angle. A standard AGN consists of a SMBH and an accretion disk, a broad line emitting region, an obscuring torus and a narrow line emitting region. The torus is a crucial component of the model as it's rotationally symmetric shape obscures part of the inner regions when seen edge-on (see Fig. 2.4). In this framework type 1 AGN are observed at small inclination angle, for which the inner region, responsible for the broad emission lines is visible. Type 2 AGN are seen at large inclination angle, hence, obscured by a optically thick and dusty torus which also weakens the observed continuum because of photo-absorption. Evidence for the anisotropic obscuring torus arise from polarization measurements and observations from the infrared spectrum.
Urry & Padovani (1995) reviewed and extended this model for radio-loud AGN by analyzing a possible connection between high luminosity RL AGN (Quasars and luminous RG) and low luminosity RL AGN (Blazars and less luminous RG). They conclude that

both groups are probably powered by the same engine and luminosity differences are due to difference inclination angles and viewing angles with respect to the jet axis. Tab. 2.1 shows the "period diagramm of AGN classes".

radio properties	optical properties		
	Type 1	Type 2	Type 0
RQ	Sy1 NLS1 RQ-QSO	Sy2 NELG LINERS	
RL	RL-NLS1 NLRG (FR I, FRII)	SSRQs, FSRQs BLRG	BL Lac objects OVV

Table 2.1.: Period diagram of AGN classes based on Urry & Padovani (1995) and Antonucci (1993). Also included are Narrow Line Seyfert 1 galaxies (NLS1) and Narrow Emission Line Galaxies (NELG).

2.1.3. The Standard Model of an Active Galactic Nucleus

The common assumption is that there is a super-massive black hole (SMBH) in every galaxy. The primary process for the generation of the observed luminosities is explained by accretion, e.g. of the interstellar medium. In-falling material accumulates in a disk, as a result of the conservation of its angular momentum and collisions. The differential velocities due to friction and turbulence inside the accretion disk yield a transport of angular momentum outwards while a stream of matter is directed to the center of the disk. The latter eventually reaches the innermost stable orbit and enters the Event Horizon of the SMBH. However, the detailed mechanism of accretion is still not fully understood.

As the material moves to the center it transfers potential energy of the gravitational field into kinetic and thermal energy. The temperature profile of the disk depends on the accretion rate and distance to the center. In a simple model of an optically thick and geometrically thin accretion disk the emitted spectrum constitutes the superposition of Planck Spectra emitted at different radii for a narrow range of temperature. In this case the maximum temperature of the disk decreases with increasing black hole mass, the thermal emission AGN accretion disks is dominant in the optical and UV band.

The luminosity L of the accretion process is proportional to the accretion rate $\dot{M}$. It is limited by the hydrostatic balance of radiation pressure and gravitation, called the Eddington Limit, meaning the emitted radiation causes a radiation pressure on in-falling matter which counteracts accretion. Assuming a stationary accretion flow and isotropic radiation this limit is determined by the Eddington Luminosity

$$L_{\mathrm{Edd}} = 4\pi \mathrm{G} c m_{\mathrm{p}} \sigma_t^{-1} M_{\odot} \approx 1.3 \times 10^{38} \left(\frac{M}{M_{\odot}} \right) \mathrm{erg/s},$$

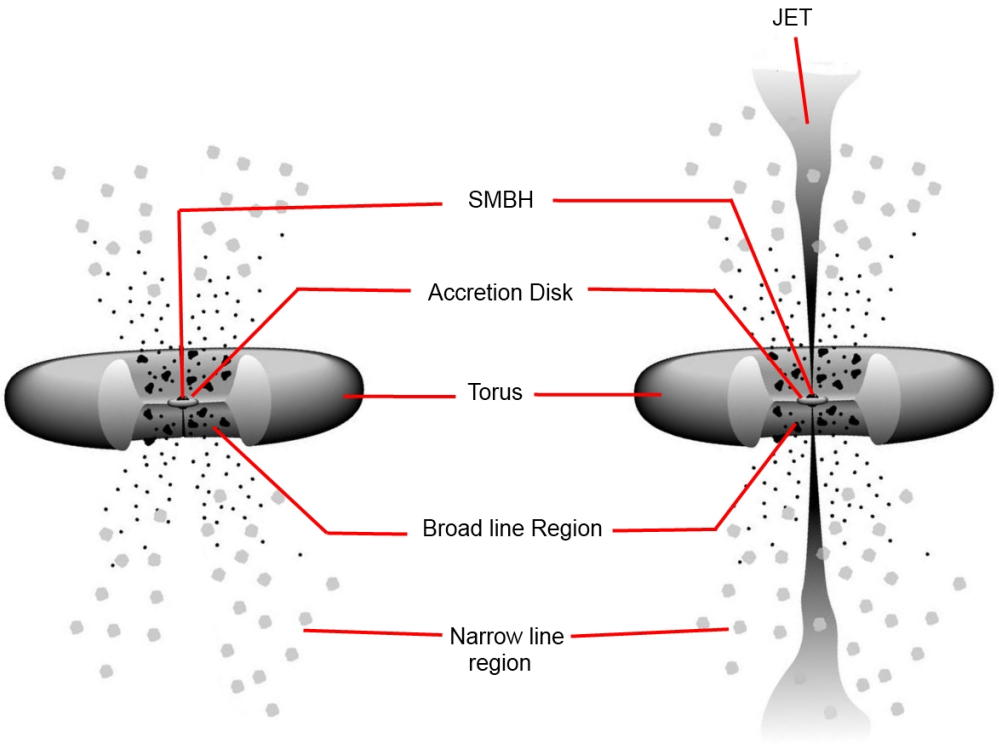

Figure 2.4.: The schematic structure of a radio-quiet (left) and radio-loud (right) AGN based on the unified model. A super-massive black hole in the center is surrounded by an accretion disk and a broad line region, embedded by a dusty torus in the orbital plane and the narrow line region on further distance. The image also shows the collimated jet along the rotation axis of the accretion disk, which is observed in radio-loud AGN. Based on the inclination angle different region are obscured by optically thick matter which determine the classification of the AGN. (Illustration based on Urry & Padovani 1995)

where G is the Gravitational constant, c is the speed of light, m_p the mass of a proton, σ_t the Thomson cross section and $M_\odot$ the solar mass. In case of anisotropic radiation, the apparent luminosity may become super-Eddington. Vice versa the bolometric luminosity can give a simple estimation of the central mass. However, since the generated luminosity is proportional to the accretion rate, it greatly depends on the form of accretion flow. In conclusion the Eddington-approximation is only a rough estimation of the black hole mass and more accurate measurements can be obtained for example by reverberation mappings (e.g. Peterson 1993, Peterson et al. 2004).

The Surrounding Matter

The primary continuum of the accretion disk interacts with the surrounding material that is commonly distinguished in three regions: the narrow line region (NLR), broad line region (BLR) and an optically thick torus. A scheme of the AGN structure is illustrated in Fig. 2.4 based on the unified model of Urry & Padovani (1995) and Antonucci (1993).

The broad line region is located at sub-parsec scale (e.g. Bianchi et al. 2012) and contains fast moving gas which is ionized by the primary continuum and winds of the accretion disk. BLR emission line profiles are characterized by widths ranging from $500\ \mathrm{km\,s^{-1}} \lesssim \Delta v_{\mathrm{FWHM}}$ up to several $10^4\ \mathrm{km\,s^{-1}}$ due to the large velocities of the gas in the proximity of the accretion disk. Observations of variable flux of broad lines with respect to the underlying continuum on timescales of days to a few hours suggest that the BLR consists of clouds of optically thick plasma with sizes of the order of $10^{-5}\,\mathrm{pc}$ (Bianchi et al. 2012) instead of large extended structures.

The BLR clouds and accretion disk are embedded in an anisotropic distribution of dust and cold gas on $1-10$ pc-scale, commonly referred to as the torus. First evidence for the existence of a torus were obtained by near infrared studies, that revealed the presence of dust close to the sublimation radius. A first image of the torus was obtained for NGC 1068 (Jaffe et al. 2004), which reveal two components of dust. A hot, elongated inner component with temperatures $\mathrm{T}\approx 800\,\mathrm{K}$ and a more extended, geometrically thicker and colder component with $\mathrm{T}\approx 300\,\mathrm{K}$. In a simplified view the torus is assumed to be a homogeneous donut-shaped distribution of dust, that depending on the inclination angle obscures the BLR and central region of the AGN. However, recent IR and radio observations suggest a more complex and clumpy structure (e.g. Elitzur & Shlosman 2006) It has been suggested that the torus and the BLR clouds form a seamless distribution (Nenkova et al. 2008).

A second region exhibiting line emission of ionized elements, the NLR, is located on $10-100$ pc scale (Bianchi et al. 2012). Its velocity dispersion and density is smaller than that of the BLR based on its larger distance to the center. Typical line width range from $200 \lesssim \Delta v_{\mathrm{FWHM}} \lesssim 900\ \mathrm{km\ s^{-1}}$. The observation of narrow forbidden lines such as [OIII]λ5007 suggest that, opposed to the gas properties of the BLR, the electron densities in NLR clouds are low enough to allow forbidden transitions and ionization is dominated by photo-ionization of the primary continuum instead of collisional ionization. In that case the NLR is expected to have a biconical morphology since the ionizing UV/X-ray source is hidden by the torus.

Even though the separation of the circumnuclear matter in different regions (BLR, NLR and dusty torus) is valid on a general view and explains the diversity of AGN spectra in the framework of the unified model as explained in Sect. 2.1.2, observational evidence, especially from X-ray absorption variability studies, show that the surrounding material has a more complex structure which is still not fully understood.

Jets

About 10% of AGN carry a relativistic jet which is emanating along the rotational poles of the AGN. Their sizes can exceed the scale of the host galaxy, reaching up to Mpc-scale. To those large distances large amounts of power in form of radiation and kinetic energy of plasma and fields is carried out. Therefore, the interaction of jets with the interstellar medium (ISM) and intergalactic medium (IGM) is of great interest for the understanding of AGN feedback during its host galaxy evolution.the plasma motion is highly relativistic. For very small viewing angles ($\lesssim 5°$) beaming effects may therefor amplify the observed luminosities (Marscher 2009). For those jets, the SED is dominated by the spectrum of the jet emission only. Like AGN, jets show a wide diversity as well. They vary in shape and power ranging from slow, weak and poorly collimated outflows in Seyfert Galaxies to relativistic and ultraluminous jets in Blazars and RL Quasars (e.g. Rosario et al. 2008). A morphological classification of the objects with jets on kpc-scale seen from the side is given by Fanarroff and Riley (Fanaroff & Riley (1974b) or see Sect. 2.1.1).

2.2. X-ray emission in obscured AGN

This chapter treats the X-ray emission observed in radio-quiet obscured AGN. The following section gives a brief description of relevant processes needed to explain the production and re-procession of X-rays in obscured AGN. In radio-quiet AGN the primary X-ray emission is associated with Compton-scattering from an extended region such as a hot corona around the accretion disk (e.g. Haardt & Maraschi 1993). This refers to thermal radiation originated from the accretion disk, which is up-scattered in the corona due to the inverse Compton-scattering effect (Sect. 2.2.2). The up-scattering of optical and UV photons generates a powerlaw spectrum which extends up to energies $\geq 100\,\mathrm{keV}$ and which presents an exponential cut off around 150...200 keV (Georgantopoulos 2012, de Rosa et al. 2012). Alternatively X-rays might originate in a small region of strong particle acceleration (e.g. Henri & Pelletier 1991). The primary X-ray continuum irradiates the accretion disk as well as the surrounding gas and plasma in which photons are redirected and down-scattered by Compton-scattering and absorbed by photo-ionization. On the other hand new photons are emitted through recombination and fluorescence.
If not stated otherwise formulas are based on Krolik (1999) or Rybicki & Lightman (1979).

2.2.1. Radiative transfer

The propagation of radiation is macroscopically expressed by the its flux F, which is defined as the amount of energy passing through an element of unit area and unit time.

$$dE = F\, dA\, dt \tag{2.2.1}$$

For an isotropic source the flux scales inversely with the distance-squared from the source of radiation. For the luminosity L, that is the energy emitted by the source in unit time, the flux is then given as

$$F = \frac{L}{4\pi\, r^2} \tag{2.2.2}$$

In the general case, the flux is defined by the specific intensity I_ν, which is the energy crossing an element of unit area per unit time, in a frequency range $d\nu$ for a given solid angle $d\Omega$. If there is no source or sink of energy the specific intensity along the line of sight is constant, due to energy conversion. Thus, the energy density in a given solid angle $u_\nu(\Omega) = I_\nu/c$ is also constant along the line of sight. The total flux in a specific frequency range can be obtained by integrating the specific intensity over the frequency range and all solid angles. If radiation passes through matter it can be affected by emission, absorption and scattering processes. These processes add or subtract energy from the radiation field and change the specific intensity. This is expressed by the transfer equation

$$\frac{dI_\nu}{ds} = -\alpha_\nu\, I_\nu + j_\nu \tag{2.2.3}$$

The first term on the right expresses the change of intensity due to absorption. It is determined by the absorption coefficient $\alpha_\nu = n\,\sigma_\nu$. For a given medium the amount of energy that is absorbed depends on the particle number density n in the medium and the cross section σ_ν for absorption. In general this includes both absorption and stimulated emission. The latter can be neglected if the number of photons per atom is small ($n_{\mathrm{pho}} a_0^3 \ll 1$, where a_0 is the Bohr radius). On the other hand energy can be added to the radiation field by spontaneous emission of a photon. This is described by the emission coefficient j_ν. For an isotropic radiation this is defined by the emissivity of the medium and its mass density, such that $j_\nu = \epsilon_\nu \rho (4\pi)^{-1}$. By introducing the optical depth along a path ds of an absorbing medium

$$\tau_\nu = \int \alpha_\nu(s')ds' \tag{2.2.4}$$

the transfer equation can also be expressed by

$$\frac{dI_\nu}{d\tau} = -I_\nu + S_\nu \tag{2.2.5}$$

where $S_\nu = j_\nu \alpha_\nu^{-1}$ is the source function. In the optically thin case, $\tau \ll 1$, the radiation can pass through matter without significant change of intensity, whilst in the optically thick case, $\tau \gg 1$ most of the radiation is absorbed. Another effect that can influence the intensity of a radiation is scattering.

2.2.2. Compton-scattering and Inverse Compton-scattering

Compton scattering describes the process of photons that scatter off electrons or ions which are at rest in lab frame. The photons lose energy ΔE in recoil which results in a kinetic energy gain of the particle . Since the cross section scales with the reciprocal mass of the scattering particle, Compton scattering is most effective for electrons and can be neglected for protons and nuclei. Assuming an initial and final four-momentum of p_{i}^{μ}, p_{f}^{μ} for the electron and k_{i}^{μ}, k_{f}^{μ} for the photon, the conversion of energy and momentum yields the Compton recoil formula in case of a stationary electron is

$$k_{\mathrm{f}} = k_{\mathrm{i}} \left(1 + \frac{k_{\mathrm{i}}}{m_e}\left[1 - \hat{e}_{\mathrm{i}} \cdot \hat{e}_{\mathrm{f}}\right]\right)^{-1} . \tag{2.2.6}$$

The scalar product $\hat{e}_{\mathrm{i}} \cdot \hat{e}_{\mathrm{f}} = \cos\theta$ defines the angle θ between the initial and final direction of the scattering photon. Thus the relative energy loss of a photon per single scatter is of the order of $\frac{k_{\mathrm{i}}}{m_{\mathrm{i}}}(1 - \cos\theta) \ll \frac{k_{\mathrm{i}}}{m_{\mathrm{i}}} \ll 1$ and scales directly with the initial energy of the incident photon. For the low energy limit the scattering is approximately elastic and reduces to the classical Thomson Scattering. The total angle averaged Thomson cross section is $\sigma_{\mathrm{T}} = \frac{8\pi}{3}\left(\frac{e}{m_{\mathrm{e}}^2 c}\right)^2$ is constant for all frequencies. However, from Eq. 2.2.6 it is evident that the energy loss depends on the scattering angle. In fact the differential Thomson cross section for unpolarized incident photons shows an angle-dependence with forward-backward symmetry:

$$\frac{d\sigma_{\mathrm{T}}}{d\Omega} = \frac{3}{16}\sigma_{\mathrm{T}}(1 + \cos^2\theta) \tag{2.2.7}$$

If the energy of the photon is comparable to the rest energy of the electron, quantum effects have to be considered. These appear in the kinematics of the scattering and its cross section. The quantum mechanical cross section is given by the Klein-Nishina-cross-section:

$$\frac{\partial\sigma_{\mathrm{KN}}}{\partial\Omega} = \frac{r_0^2}{2}\left(\frac{k_{\mathrm{f}}}{k_{\mathrm{i}}}\right)^2 \left(\frac{k_{\mathrm{i}}}{k_{\mathrm{f}}} + \frac{k_{\mathrm{f}}}{k_{\mathrm{i}}} - \sin^2\theta\right), \tag{2.2.8}$$

where $r_0 = e^2/m_e c^2$ is the classical electron radius. With rising photon energy compared to electron energy the angular distribution becomes more concentrated in the forward direction. In the low energy limit the Klein-Nishina cross section reduces to the Thomson limit ($k_{\mathrm{f}} \approx k_{\mathrm{i}}$).
Inverse Compton scattering occurs when the kinetic energy of the electron is sufficiently high compared to photon energy and it cannot be treated stationary in lab frame. In this case a photon might gain net energy of the electrons and get up-scattered to higher frequencies. Considering non-stationary electrons with a velocity $\vec{\beta}$ in units of the speed of light and a Lorentz factor $\gamma = \frac{1}{\sqrt{1-\beta^2}}$, for the non-relativistic case, $\gamma^2 - 1 \ll k_{\mathrm{i}}/m_e c^2$,

the photon energy in electron lab frame is low enough to scatter elastically and Thomson scattering applies. One can show, by transforming back to lab frame and averaging over all angles, with each inverse Compton scattering the photon energy gets amplified by a factor $\left\langle \frac{k_\mathrm{f}}{k_\mathrm{i}} \right\rangle \sim \gamma^2$, and $\left\langle \frac{k_\mathrm{f}}{k_\mathrm{i}} \right\rangle \sim \frac{4}{3}\gamma^2$ in case of relativistic electrons. The emitted power of the photons in lab frame is

$$\frac{dE}{dt} = c\sigma_\mathrm{T}\gamma^2(1+\frac{1}{3}\beta^2)U_\mathrm{ph}, \tag{2.2.9}$$

where U_ph is the energy density of the incident photons. In general the change of the initial energy of the photons is

$$\frac{dE}{dt} = -c\sigma_\mathrm{T}U_\mathrm{ph}, \tag{2.2.10}$$

thus the electrons transfer a net energy to the photons equal to

$$\frac{dE}{dt} = \frac{4}{3}c\sigma_\mathrm{T}\gamma^2\beta^2U_\mathrm{ph}. \tag{2.2.11}$$

In case of inelastic scattering in the electron's rest frame one has to consider a correction factor $\left(1-\frac{63}{10}\frac{\gamma<E^2>}{mc^2<E>}\right)$, where $<E^2>$ and $<E>$ are mean values integrated over U_ph. The final spectrum of the photons depends on the initial distribution of electrons and number of scattering. In case of multiple scattering an arbitrary distribution of electrons yield a powerlaw distribution of photons.

$$I(E) \sim I(E_0)\left(\frac{E}{E_0}\right)^\alpha \tag{2.2.12}$$

where α is the spectral index and E_0 is the mean energy of the initial photon distribution.

2.2.3. Atomic processes

The soft X-rays of Seyfert galaxies exhibit a forest of different emission and absorption lines, which can serve as a diagnostic tool for the region where the lines originate from. Line emission is caused by the transition between atomic energy levels (from initial level E_i to final state E_f). The power emitted through line emission per unit volume of a plasma depends on the population N_i of atoms in level i, the energy difference $\Delta E = h\nu_\mathrm{if}$ and the transition rate, expressed by the Einstein coefficient A_if:

$$\frac{dP}{dV} = N_\mathrm{i}h\nu_\mathrm{if}A_\mathrm{if}. \tag{2.2.13}$$

The Einstein coefficient A_{if} describes the probability of transition by spontaneous emission. The quantum mechanical derivation in electric dipole approximation gives

$$A_{\mathrm{if}} = \left(\frac{8\pi^2 \mathrm{e}^2}{m_{\mathrm{e}} \mathrm{c}^3}\right) \nu_{\mathrm{if}}^2 f_{\mathrm{if}}, \tag{2.2.14}$$

where f_{if} is the oscillator strength. It is motivated by the assumption that the electron behaves like an oscillator with frequency ν_{if} between two the two energy levels E_{i} and E_{f} during the transition. The spontaneous emission is related to absorption by the Einstein coefficient B_{fi}, which excites an electron of a lower energy level E_{i} to a higher state E_{f}. They are related via

$$A_{\mathrm{if}} = \frac{2h\nu_{\mathrm{if}}^2}{c^2} B_{\mathrm{fi}}. \tag{2.2.15}$$

The possible bound-bound transitions that can occur in an atom are constrained by conservation of spin, orbital and total angular momentum. These are expressed by the selection rules that determine allowed transitions in dipole approximation. If the atom is in ground state, these lines are called resonance lines. They have a transition rate of $A_{\mathrm{if}} \sim 10^8 – 10^{13}\,\mathrm{s}^{-1}$. However, there are forbidden lines, that results from the contribution of higher orders of electric dipole and magnetic dipole moments. They are called forbidden lines, for they do not submit to the selection rules and happen at a much smaller rate of the order of $A_{\mathrm{if}} \sim 10 – 10^4\,\mathrm{s}^{-1}$.

The emitted line has a natural line width that results from the finite life time of an atomic state and the corresponding energy uncertainty of the level. The profile of the line is a Lorentz profile. In addition, thermal motion of atoms causes a Doppler broadening due to the Doppler effect. For a Maxwell-Boltzmann distribution of the radial velocities of ions, the line profile is described by a Gaussian profile with a Doppler width. So far, only bound-bound transition inside the atom were regarded. In a plasma atoms can be ionized and recombine, thus emit fluorescence and recombination lines. Ionizations (recombinations) are bound-free (free-bound) transitions. In ionization an electron in bound state absorbs a photon or collides with a free electron and is excited into a free continuum state. For photo-ionization, given an ionization potential χ and a photon energy $h\nu$, the kinetic energy of the free electron is $E = h\nu - \chi$. The cross section σ_{bf} for photo-ionization rises abruptly when the photon energy equals the ionization potential of an energy level n ($h\nu_{\mathrm{n}} = \chi_{\mathrm{n}}$) and decreases roughly with $E_{\mathrm{ph}}^{-3} = (h\nu)^{-3}$ afterwards. Fig. 2.5 illustrates the behavior of $\sigma_{\mathrm{bf}} E_{\mathrm{ph}}^{-3}$ with respect to the photon energy E_{ph}. The jumps are called absorption edges.

In recombination free electrons are caught in an excitated state of an ion with a subsequent radiative decay into ground state. The probability of a recombination event can be expressed by the Milne relations, which connect the cross section for free-bound transitions to the one of photo-ionization. For a thermal electron distribution and a

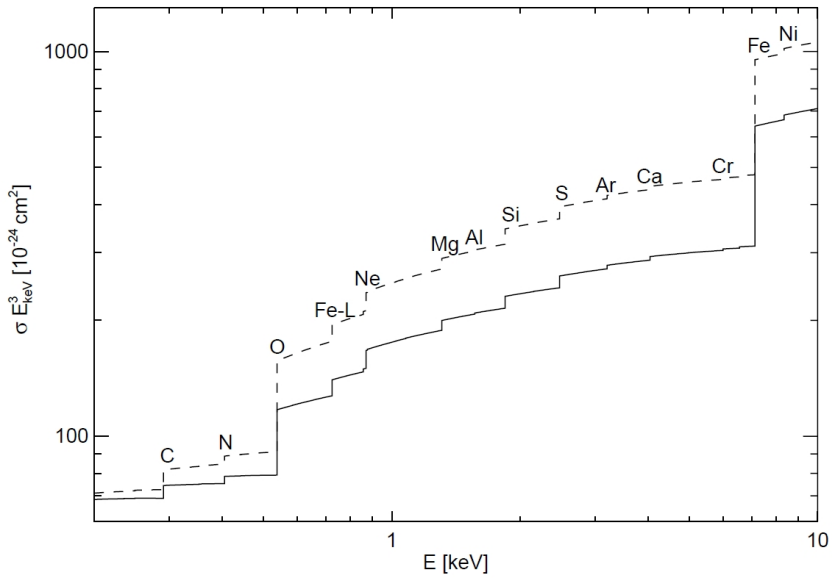

Figure 2.5.: Absorbtivity per hydrogen atoms for solar abundance (dashed lines) and theoretical abundance of the ISM, by Wilms et al. (2000).

Planck radiation field, the Milne relations area

$$\frac{\sigma_{\mathrm{bf}}}{\sigma_{\mathrm{fb}}} = \frac{m^2c^2\nu^2}{v^2h^2}\frac{g_{\mathrm{e}}g_{+}}{2g_{\mathrm{n}}} \tag{2.2.16}$$

where g_{i} is the degeneracy of ions (+), electrons (e) and neutral atoms (n), defining the ionization state of the plasma.
The ionization balance is described by the rate equation. For a number of elements $n_{\mathrm{Z}}(z)$ with atomic number Z in ionization state z, the rate equation including collisional (de)-excitation, photo-emission and photo-absorption is:

$$\frac{dn_{\mathrm{Z}}(z)}{dt} = -n_{\mathrm{f}}n_{\mathrm{e}}C_{\mathrm{fi}} + n_{\mathrm{f}}A_{\mathrm{if}} + n_{\mathrm{i}}n_{\mathrm{e}}C_{\mathrm{if}} - n_{\mathrm{f}}B_{\mathrm{fi}}, \tag{2.2.17}$$

where the subscript i labels the initial state, f the final state and n_{e} the electron density. For a general plasma the rate equation includes all possibles physical processes, like photo-ionization, collisional ionization, radiative recombination, dielectric recombination, photo- and collisional de-excitation, Auger effect and auto-ionization. A derivation of the equation rate in an astrophysical optically-thin plasma is given, e.g. in Kinkhabwala et al. (2003), who particularly calculated the solution for rate equations in photo-ionized plasma, including relevant processes depicted in Fig. 2.6. In astrophysics plasma is distinguished in collision-driven plasma and photo-ionized-plasma. Collisional plasma is heated mechanically, through collisions. The line emission is mainly radiative decay following collisional excitation. Photo-ionized-plasma is irradiated by a powerful exter-

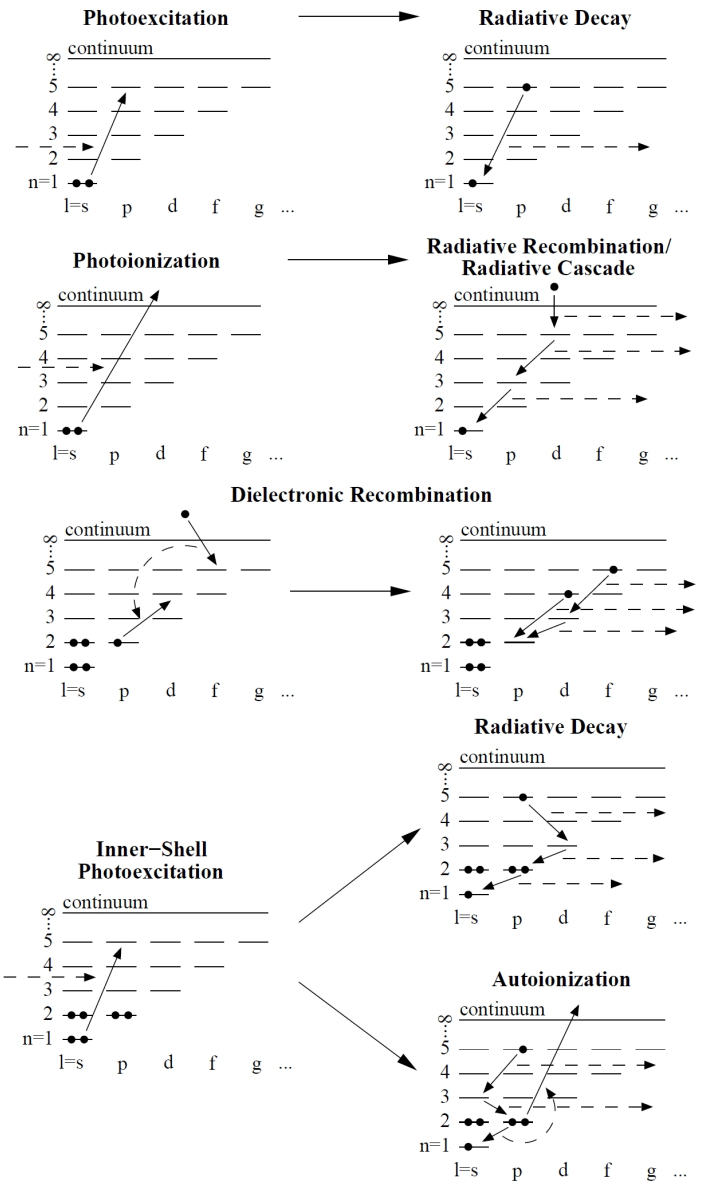

Figure 2.6.: Simplfied diagrams of relevant processes for photo-ionized plasma, by Kinkhabwala et al. (2003)

nal source and line emission is caused by recombination and radiative cascade, which follows photo-ionization as well as radiative decay following photo-excitation. In general a mixture of both is possible, e.g. in accretion disks.

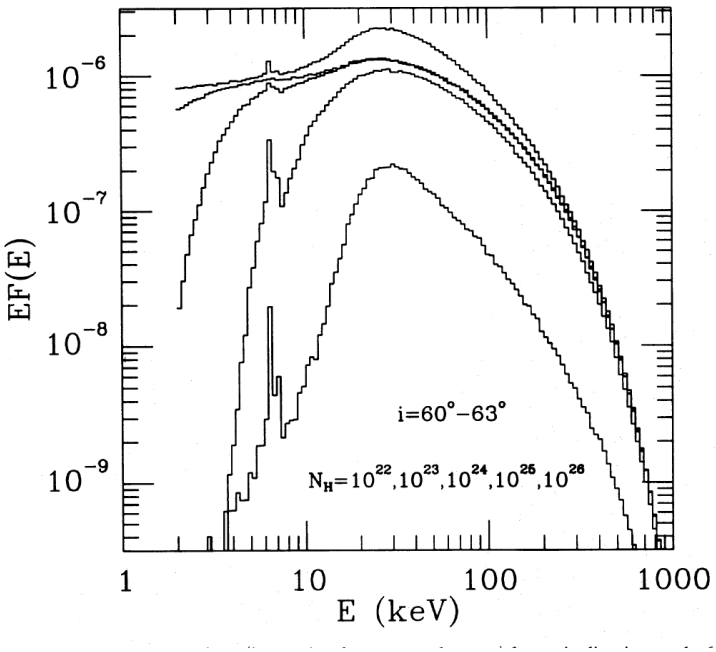

Figure 2.7.: Reflection spectrum for different column densities $\log N_{\mathrm{H}} = 22, 23, 24, 25, 26$ from top to bottom, calculated by Ghisellini et al. (1994a).

2.2.4. X-ray reprocession

The process of X-ray reflection was first introduced by Basko et al. (1974) for a galactic X-ray binary, and describes the process of X-ray backscattering from an irradiated medium. The back-scattered spectrum is commonly referred to as reflected spectrum and consists of a continuum defined by the contribution of photo-absorption and Compton-scattering, as well as line emission following photo-absorption. At 10 keV the cross section of Compton-scattering-scattering and photo-absorption is about unity. The inverse Compton up-scattered continuum is again down-scattered by Compton-scattering where the photons lose energy according to Eq. 2.2.6. At lower energies the absorbtivity of the reflecting matter increased with decreasing energy. A combination of Compton-scattering-scattering and absorption effects yield a prominent Compton-scattering hump, which peaks at ~ 20 keV (Magdziarz & Zdziarski 1995), and is a prominent feature of the reflected spectrum. The strength of the reflected spectrum depends on the optical depth of the reflector, thus its (column) density. A reflection spectrum for different column densities is depicted in Fig. 2.7. The reflected spectrum differs in shape and intensity depending on the geometry, ionization state and density of the absorber, as well as the inclination angle of the line of sight. It is differed between cold and ionized reflection, where the first assumes a weak local radiation field, and a neutral or low ionized reflector. The albedo of reflection then only depends in the competition of Compton-scattering-scattering and photo-absorption. First studies of the reflection spectrum from accretion

disk came from e.g. White et al. (1988), Guilbert & Rees (1988), Felsteiner & Opher (1976) or Magdziarz & Zdziarski (1995). The latter calculated the Compton-scattering reflection continuum of a cold slab of electrons and whose model `pexrav` is still mainly used to model neutral reflection.

Following photo-absorption the excited atoms emit fluorescence lines, whose strength depend on the transition rate and abundance. The most prominent line is the Fe Kα line at $\sim$ 6.4 keV (e.g.Matt et al. 1996a), which can be seen in Fig. 2.7, due to its high iron abundance and transition rate. It can serve as a diagnostic tool to determine the properties of the reflecting material (e.g. García et al. 2011). The narrow line from single-scattering in the reflector is often accompanied by a so-called 'Compton-scattering Shoulder' (Matt 2002b), which is caused by multiple scattering in the reflector of line photons.

Ionized reflection occurs when the radiation field is high enough to ionize at least the surface of the reflector. The ionization of the medium is expressed by the ionization parameter (Tarter et al. 1969)

$$\xi = \frac{4\pi F}{n}, \tag{2.2.18}$$

where F is the flux of the radiation and n is the number density of the reflecting medium. The reflection from ionized material differs from neutral one, as can be seen in Fig. 2.8, (e.g. García & Kallman 2010, Życki et al. 1994 or Ross et al. 1999). The figure shows the reflection spectrum in the 1 eV–100 keV range for different orders of the ionization parameter $\log \xi$. For cold medium ($\xi \sim 0.01$) heavy elements are weakly ionized, the optically thick medium causes a prominent Compton-scattering hump and a forest of fluorescence lines following photo-absorption and radiative recombination following photo-ionization. The original powerlaw distribution is significantly altered, because of the photo-absorption in the 0.1-10 keV energy range. The more ionized the medium gets, the more elements are fully ionized and the opacity of the reflecting medium decreases. In effect, the albedo of the reflecting medium increases and the continuum reflection becomes more efficient. This smears the fluorescence lines, which decrease in strength for increasing ionization. Due to changing abundances and different contribution of ionized lines, the absorption edges are smeared out.

Ikeda et al. (2009) calculated the spectrum that is reflected from a donut shaped torus, for an isotropic irradiation of an X-ray source in its center. They distinguish between the reflection that occurs at the inner walls of the far-side of the torus and the component that is reflected through the torus and an absorbed component, seen through the torus. The simulated spectrum of these three components is shown in Fig. 2.9. These components behave differently with geometrical parameters of the torus. The continuum that is reflected from the inner wall of the torus greatly depends on its inclination Θ_i and opening angle $\Theta_{\rm oa}$. The first ($\Theta_{\rm i} \geq \Theta_{\rm oa}$, for Sy2 galaxies) affects the visibility of the inner walls, since with increasing $\Theta_{\rm i}$ the observed area of the inner wall decreases. The opening angle $\Theta_{\rm oa}$, on the other hand, affects the size of the projected area of the

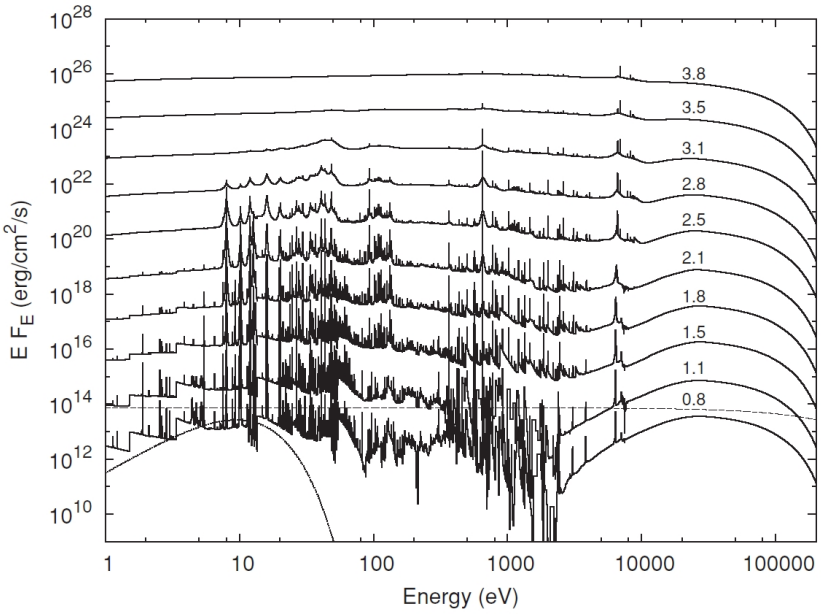

Figure 2.8.: Reflected spectra, simulated by García & Kallman (2010), for different values of the ionization parameter $\log \xi$ (solid lines). For clarity the curves are shifted by an arbitrary factor. Dotted line: Intrinsic accretion disk flux, that is up-scattered through inverse Compton-scattering-scattering that yields a powerlaw X-ray continuum (dashed line for the case $\log \xi = 0.8$).

inner walls with respect to the line of sight. Among those parameters the strength of the reflected continuum is dominated by the inclination angle (Ikeda et al. 2009). As for the transmitted component, the dependency of the inclination and opening angle is vice-versa. This component shows small dependency on Θ_i and mainly depends on the opening angle and column density, as this affects the covering factor and fraction of the transmitted continuum (Ikeda et al. 2009). As can be seen in Fig. 2.9, above 6 keV the absorbed reflection spectrum is very similar to the absorbed intrinsic powerlaw. For energies below 6 keV, though, due to the absorption, the direct reflection dominates the soft spectrum.

2.3. Compton-Thick AGN

According to X-ray surveys a large fraction of AGN in the nearby universe are obscured with equivalent hydrogen column densities $N_H \geq 10^{22}\,cm^{-2}$ (e.g. Maiolino et al. 1998, Risaliti et al. 1999, Malizia et al. 2009). The relative percentage differs from survey to survey depending on the sensitivity and observed energy range of the instrument. As obscuring matter is transparent to X-rays in the 2–10 keV up to $N_H \leq 10^{24} cm^{-2}$ hard

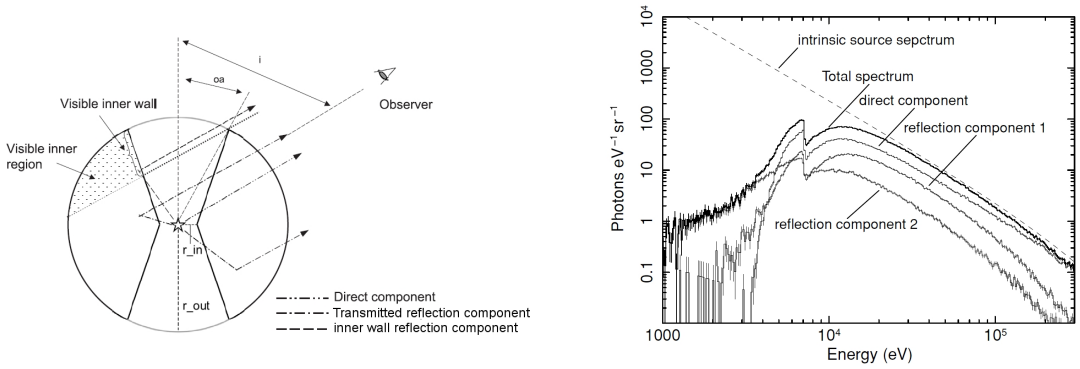

Figure 2.9.: Different components of the reprocessed spectrum assumed by Ikeda et al. (2009). The direct component is associated with the absorbed primary continuum, while they distinguish between directly observed reflection coming from the inner wall of the torus and the one seen through the torus.

X-ray surveys like *Chandra*[1] deep-field survey or deep *XMM-Newton*[2] surveys as well as *Integral*[3] and *Swift*[4]-BAT surveys are powerful tools to detect and observe obscured AGN. Below 10 keV obscuration can be associated with photoelectric absorption, but for higher energies Compton-scattering-scattering becomes non-neglible as the cross section for photoelectric absorption and Compton-scattering is approximately equal at 10 keV. This causes a Compton down-scattering of high energy photons to lower energies and subsequent photoelectric absorption. For high column densities the entire high energy X-ray spectrum is down-scattered and absorbed in the obscuring matter. This causes that even *Integral* and *Swift*-BAT surveys which observe in the 15–200 keV range miss heavily obscured AGN with column densities exceeding $10^{25}\,\mathrm{cm}^{-2}$. Risaliti et al. (1999) (RMS99 hereafter) analyzed hard X-ray *ASCA*[5] and *BeppoSAX*[6] data of 37 Seyfert 2 galaxies, among which they find 75% to be obscured by column densities $N_H \geq 10^{23}\,\mathrm{cm}^{-2}$. On the other hand a more recent study of *Integral* data of 88 AGN by Malizia et al. (2009) found $\sim$ 43% obscured AGN. It should be noticed, though, that in contrast to RMS99 both Seyfert type 1 and 2 galaxies are included. Only regarding type 2 Seyfert galaxies the fraction of obscured galaxies with $N_H \geq 10^{23}\,\mathrm{cm}^{-2}$ increases to 55%. This is still lower than what was found by RMS99, which, according to Malizia et al. (2009), is because of a higher flux detection limit in their sample. The evolution of the Compton-Thick fraction with redshift is still poorly known.
With increasing column density the contribution of Compton-scattering to the resulting

[1]Chandra mission: http://chandra.harvard.edu/
[2]XMM-Newton mission:http://sci.esa.int/science-e/www/area/index.cfm?fareaid=23
[3]Integral mission: http://sci.esa.int/science-e/www/area/index.cfm?fareaid=21
[4]Swift mission: http://swift.gsfc.nasa.gov/docs/swift/swiftsc.html
[5]ASCA mission: http://heasarc.gsfc.nasa.gov/docs/asca/ascagof.html
[6]BeppoSAX mission: http://www.asdc.asi.it/bepposax/

energy density increases. Therefore obscured AGN are roughly classified as (Comastri 2004):

- **Compton-thin** for $10^{22}\,\mathrm{cm}^{-2} \leq \mathrm{N_H} \leq 10^{23}\,\mathrm{cm}^{-2}$,
- **mildly Compton-thick** for $10^{23}\,\mathrm{cm}^{-2} \leq \mathrm{N_H} \leq 10^{24}\,\mathrm{cm}^{-2}$,
- **heavily Compton-thick** for $10^{24}\,\mathrm{cm}^{-2} \leq \mathrm{N_H}$.

But these boundaries differ from author to author and should be regarded as guidelines rather than characteristic values. The inverse of the Thomson cross section at 10 keV for cosmic abundance is a commonly used boundary to separate Compton-thin and Compton-scattering-thick AGN as it marks the density for unity optical depth for Compton-scattering (Comastri 2004).
For Compton-thick AGN (C-thick AGN) most, if not all, of the nuclear emission is down-scattered and/or absorbed by the obscuring matter. The absorbed luminosities are re-emitted at larger wavelength, i.e. in the mid- and far-infrared (MIR, FIR). C-thick AGN therefore contribute to the IR background as well as they are postulated and non-neglible for synthesis models of the Cosmic X-ray background (XRB) in order to account for the peak XRB emission at 30 keV.
The soft X-ray emission below 10 keV is thought to be scattered nuclear emission, which is not effected by obscuration. A possible and accepted scenario is that the scattered light originates in an extended gas outside the obscuring matter (Guainazzi et al. 2005b) (see Fig. 2.10). Furthermore thermal emission from starburst and star formation related processes like X-ray binaries in the host galaxy may also contribute (Brightman & Ueda 2012).
In general C-thick AGN present a complex X-ray spectrum which cannot be sufficiently explained by a single absorbed powerlaw. The main characteristics of a C-thick spectrum are

- a flat spectrum for $\mathrm{E} \leq 10\mathrm{keV}$, resulting from the down-scattering and absorption of high energy photons to lower energies, as well as X-ray reflection at the backside of the obscuring matter (Georgantopoulos 2012).
- a prominent Fe Kα line with equivalent width (EW) $\approx$ 1 keV (Fukazawa et al. 2011), even though exceptions with EW$\cong$ 300 eV have been observed e.g. in Mrk 231 (Braito et al. 2004).
- an exponential cut-off of the spectral energy density at $\mathrm{E} \approx 100-200$ keV depending on the column density (Georgantopoulos 2012, de Rosa et al. 2012).
- a X-ray reflection component with a broad Compton-scattering hump peaking at 20-30 keV affected by Compton-scattering and photoelectric absorption at both high and low energies. The relative intensity of the reflected spectrum depends on

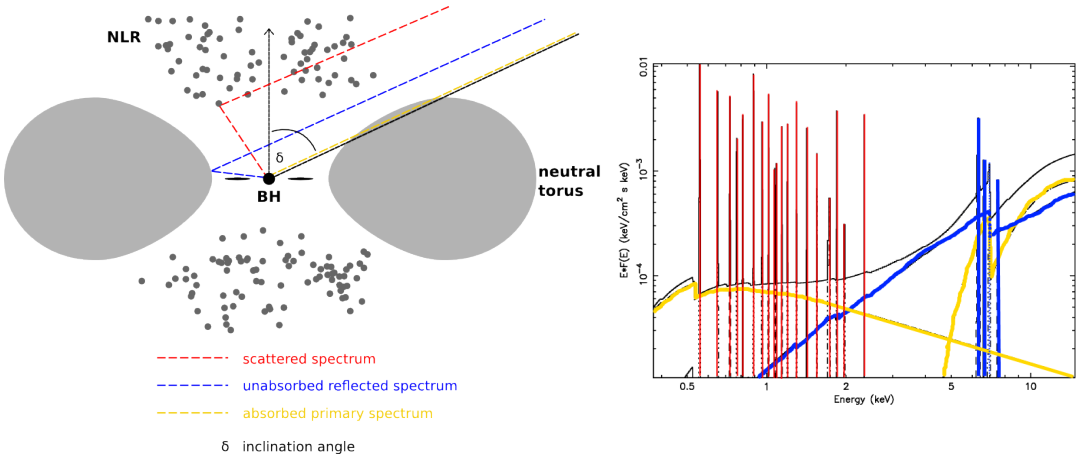

Figure 2.10.: Illustration of a scenario causing the spectral components seen in Compton-thick spectra under an inclination angle δ. A reflected component with an Fe Kα line (blue dotted line), a heavily absorbed powerlaw (yellow dash-dotted line), and scattered emission line features (red solid line). The right panel shows a modified example model of Mrk 3. Credit: Bianchi et al. (2005).

the column density, ionization state and metallicity of the obscuring matter. (e.g. Comastri 2004, Fabian & Ross 2010 or Matt 2002a).

The prominent iron line results from the suppression of transmitted continuum. Naturally there is a correlation between the column density and the EW of the iron line (Comastri 2004). But a high EW can also be obtained by high inclination angles or a large covering factor of the obscuring matter (Levenson et al. 2002). Nevertheless, the intensity of the iron line remains a powerful diagnostic for the presence of C-thick matter. Whether it is produced by transmission (Leahy & Creighton 1993) or reflection (Ghisellini et al. 1994b, Matt et al. 1996a) is still a matter of debate.
In general X-ray obscuration is associated with type 2 AGN. However, there is observational evidence for a mismatch between optical and X-ray classification. For example, Guainazzi et al. 2003 found obscured AGN with broad optical emission lines, or Maiolino et al. 2003 report on objects without any Seyfert-like signatures in the optical spectrum. The classification is even more complicated by the high amplitude variability of X-ray obscured AGN (Guainazzi et al. 2005a, G05 hereafter), where a transmission of C-thin to C-thick properties and vice versa is observed in multiple objects within timescales of years.
Following the type 2 classification the obscuring gas was first identified with the dusty torus in the framework of the unified model (see Sect. 2.1.2). This assumption is challenged by the observation of fast changes in the X-ray obscuring column densities indicating smaller distances of the C-thick matter to the central SMBH than a pc-scale torus (Bianchi et al. 2009). However the covering factor and density of the BLR are too low to account for heavy obscuration in AGN. This demonstrates that the exact location,

structure and distribution of the obscuring matter is still unknown and more complex than a homogeneous torus. Guainazzi et al. (2005b) suggested a multiple absorber scenario based on a study of X-ray emission with respect to the presence of dust in the host galaxy, and suggest X-ray obscuration to take place at different scales. Despite compact matter responsible for obscuration in the nuclear region, extended dust lanes of the host galaxy can also contribute to the X-ray obscuration. Multiple absorber were measured by Matt et al. (2001) and Matt et al. (2003a) with the lowest column densities consistent with densities of dust lanes of the host galaxy. G05 concluded that compact distributions of gas are more likely to cause C-thick absorption, while more extended gas distributions may account for rather C-thin or mildly C-thick obscuration.
Further X-ray studies are necessary to analyze the geometrical and physical properties of the circumnuclear matter. Because in C-thick AGN the primary continuum is heavily suppressed they are well suited to study the reprocessed emission which have marks of the obscuring and scattering matter.

3. The XCTA sample

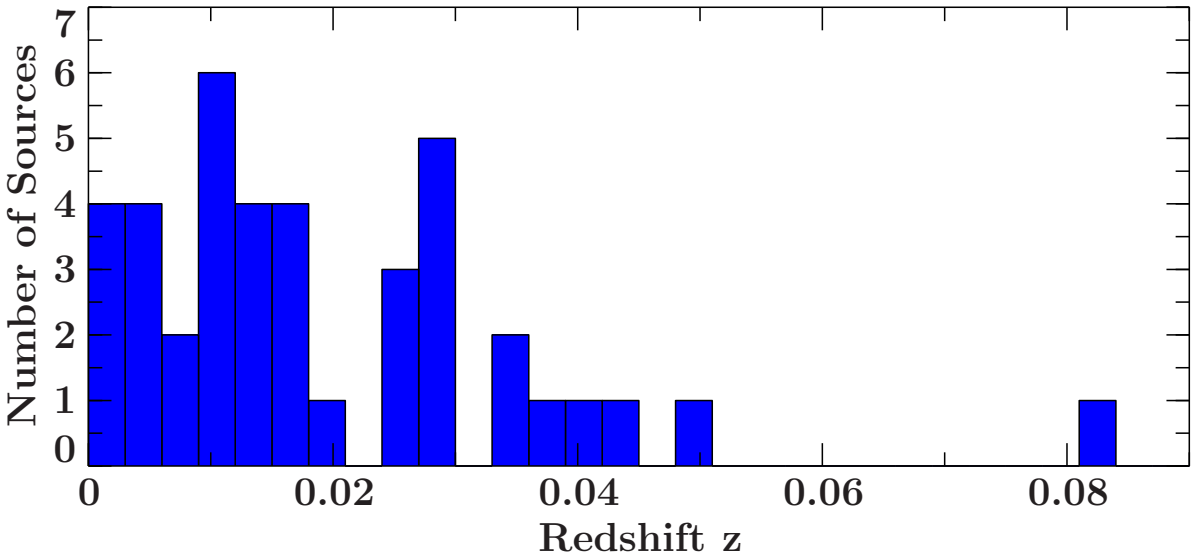

Figure 3.1.: Redshift distribution of the XCTA-Sample.

The motivation for the X-ray analysis of compton-thick Seyfert II galaxies was to obtain obtain statistical information about the iron line properties of these sources. The first selection of sources was based on a literature search by G. Miniutti[1], which comprised 56 sources published as compton-thick obscured Seyfert II galaxies. Compton-thick AGN present a complex spectrum in the 0.2-10 keV range with different continuum and line emission components (see Sect. 2.2.4). In order to model these components it is important to obtain good quality data. This is achieved by using data of the EPIC PN camera of the *XMM*-Newton space telescope. Among the current X-ray telescopes[2] *XMM*-Newton has the largest effective area and provides high spectral resolution that is required for this analysis. There are 46/56 sources of the first selection which have been observed by *XMM*-Newton for at least 10ks. After data reduction each spectrum was checked individually: background dominated spectra with a background-to-source flux ratio $\geq 50\%$ were neglected as well as those with less than 120 spectral data counts

[1] Centro de Astrobiologia, Dep. de Astrofisica, ESA, P.O.Box 78, 28691 Madrid, Spain

[2] In July 2012 *NuStar* was launched. The new X-ray mission from NASA, *NuStar* observes in the 3-79 keV energy range, with an effective area comparable with the one of XMM-Newton at 6 keV and a spectral resolution of 0.4 keV at 6 keV.

in the 2-10keV range. Eventually, the sample used for the hard X-ray analysis in the 2-10keV range consists of 32 sources listed in Tab. 3.1, labeled as HX-subsample. During the analysis of the HX-subsample, Severgnini et al. (2012) published a survey with 35 newly classified compton-thick sources, seven of which met the selection criteria and may therefore be included in the sample. These sources are also included in Tab. 3.1, labled as S12-subsample. The analysis was only performed on the HX-subsample, so far. The final XMM-Compton-Thick-AGN (XCTA) sample consists of 39 sources in the redshift range of 0.001 to 0.08 , see Fig. 3.1.

The XCTA-Sample

Source name (NED)	z	ObsID	t_{obs} [ks]	ObsDate	Region	GTI	#counts	t_{exp} [ks]	SubSample
2MASX J1238+0927	0.082902	0504100601	26	2007-06-21	28/28	0.1	2.23E+003	17.45	HX
2MASX J115704+5249	0.035501	0504100901	22	2007-12-09	15/15	0.4	8.23E+002	20.71	HX
2MFGC2636	0.028286	0307000201	16	2005-08-05	40/40	0.4	8.13E-001	12.6	S12
CGCG 218-007	0.027276	0504101601	37	2007-11-21	12/12	0.4	6.91E+002	11.73	HX
CGCG 420-015	0.029390	0307000401	16	2005-08-30	40/40	0.4	1.42E+003	12.59	S12
Circinus	0.001448	0111240101	110	2001-08-06	30/20	0.1	8.04E+004	66.22	HX, Xbr
ESO 137-G34	0.009144	0307001901	22	2009-02-13	45/25	0.4	2.00E+003	17.29	HX
ESO 138-G1	0.009140	0405380201	34	2007-02-16	30/30	0.06	2.96E+003	15.64	HX, XBr
	0.009140	0405380901	25	2007-03-25	14/14	0.1	4.17E+003	8.2	HX, XBr
ESO 362-G8	0.015748	0307001401	18	2006-02-13	30/30	0.4	4.41E+002	14.45	S12
IC 2560	0.009757	0203890101	82	2003-12-03	40/15	0.4	5.40E+003	71.75	HX
IC 4995	0.016094	0200430601	12	2004-09-25	40/25	0.4	9.58E+002	8.95	HX
IGR J20286+2544	0.013900	0312192301	14	2006-04-23	27/27	0.05	2.34E+003	10.81	HX
IRAS F08216+3009	0.025325	0504102001	24	2007-11-03	22/22	0.4	2.21E+003	19.02	HX
MKN 231	0.042170	0081340201	22	2001-06-07	20/20	0.1	1.90E+003	16.4	HX
Mrk3	0.013509	0111220201	61	2000-10-19	30/30	0.01	4.30E+004	48	HX
	0.013509	0009220601	14	2001-03-20	30/30	0.01	7.71E+003	9.11	HX
	0.013509	0009220701	9	2001-03-28	30/30	0.04	3.55E+003	4.27	HX
	0.013509	0009220401	9	2002-03-10	30/30	0.03	4.52E+003	5.2	HX
	0.013509	0009220901	8	2001-09-12	30/30	0.01	3.77E+003	4.22	HX
Mrk 266	0.027863	0055990501	23	2002-05-15	15/15	0.15	4.89E+002	16.22	HX
Mrk 573	0.017179	0200430701	12	2004-01-15	12/12	0.4	2.37E+003	9.04	HX
Mrk 78	0.037150	0307001501	16	2006-03-11	35/35	0.4	2.48E+003	10.88	S12
NGC 424	0.011764	0550950101	127	2008-12-07	30/30	0.1	4.17E+004	110.23	HX
NGC 1068	0.003793	0111200101	35	2000-06-29	40/40	0.04	3.88E+005	34.59	HX
	0.003793	0111200201	35	2000-06-30	40/40	0.04	3.82E+005	33.83	HX
NGC 1194	0.013596	0307000701	16	2006-02-19	35/35	0.4	4.84E+002	12.5	S12
NGC 1320	0.008883	0405240201	17	2006-08-06	12/12	0.4	2.55E+003	13.37	HX
NGC 1386	0.002895	0140950201	17	2002-12-29	16/16	0.4	2.69E+003	14	HX
NGC 2273	0.006138	0140951001	13	2003-09-05	15/15	0.4	1.01E+003	9.9	HX
NGC 3079	0.003723	0110930201	25	2001-04-13	13/13	0.4	1.60E+003	17.16	HX
NGC 3393	0.012509	0140950601	16	2003-07-05	13/13	0.4	2.07E+003	11.7	HX
NGC 3690	0.010411	0112810101	22	2001-05-06	25/25	0.1	7.43E+003	15.33	HX
NGC 4666	0.005101	0110980201	58	2002-06-27	20/20	0.35	3.16E+003	47.95	HX

Continued on next page

Table 3.1 – continued from previous page

Source name (NED)	z	ObsID	Duration [ks]	ObsDate	Region	GTI	#counts	ExpTime [ks]	SubSample
NGC 4945	0.001878	0112310301	24	2001-01-21	20/20	0.4	2.78E+003	17.85	HX
	0.001878	0204870101	65	2004-01-11	20/20	0.4	1.16E+004	53.99	HX
NGC 4968	0.009863	0200660201	18	2004-07-05	20/20	0.01	6.24E+002	9.06	HX
NGC 0591	0.015167	0200431001	12	2004-01-12	13/13	0.4	6.54E+002	9.05	HX
NGC 5194	0.001544	0112840201	21	2003-01-15	30/30	0.4	5.30E+003	17.12	HX
NGC 6240	0.024480	0101640101	30.1	2009-09-22	50/50	0.2	2.01E+004	22.39	HX
	0.024480	0101640601	19	2002-09-12	50/50	0.4	1.19E+004	11.34	HX
	0.024480	0147420201	42	2003-03-14	50/30	0.4	1.58E+004	19.42	HX
	0.024480	0147420401	14	2003-08-13	50/30	0.25	6.16E+003	10.27	HX
	0.024480	0147420501	31	2003-08-21	50/30	0.4	4.98E+003	6.36	HX
NGC 6926	0.019613	0306050801	12	2005-11-19	35/35	0.4	1.25E+002	8.77	S12
NGC 7212	0.026632	0200430201	14	2004-05-20	20/20	0.35	1.28E+003	11.01	HX
NGC 7674	0.028924	0200660101	10	2004-06-02	30/30	0.25	1.39E+003	8.11	HX
NGC 7582	0.005254	0112310201	23	2001-05-25	30/30	0.4	3.15E+003	17.94	S12
	0.005254	0204610101	102	2005-04-30	30/30	0.4	1.39E+004	82.62	S12
SWIFT 1009.3-4250	0.033537	0501210101	26	2007-06-14	25/25	0.1	5.31E+003	21.17	HX
UGC 5101	0.039367	0085640201	35	2001-11-12	13/13	0.01	6.51E+002	25.72	HX

Table 3.1.: List of sources in the XCTA-Sample. For further information about the selection criteria see the text. The list includes source identifications and redshifts, taken from NASA Extragalactic Database (NED, http://ned.ipac.caltech.edu/), as well as information about the extracted observations. This comprises the observation ID number, duration of observation and date. Information about the extraction criteria, i.e. extraction radius, good time intervall filter and final number of counts and exposure time are also given.

4. The XMM-Newton observatory

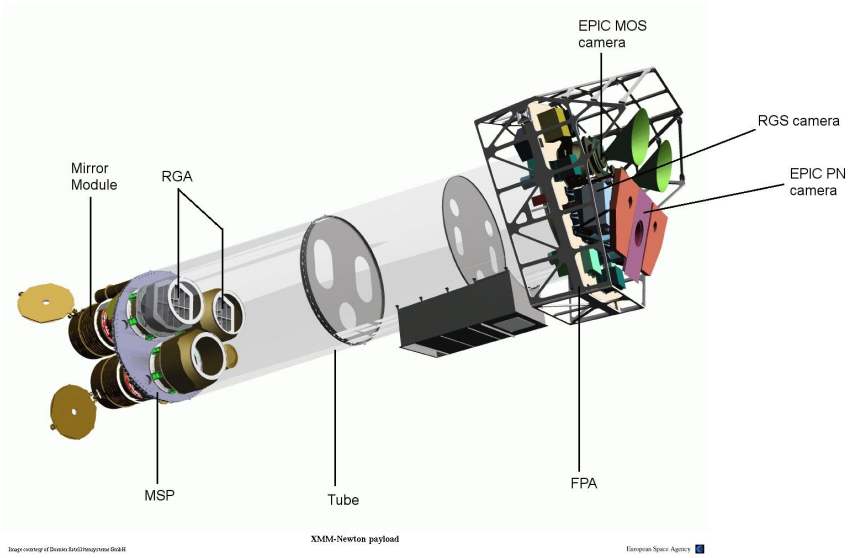

Figure 4.1.: Sketch of the *XMM-Newton* payload. In the lower left the mirror modules and Reflecting Grating Arrays (RGA) are visible. The optical monitor (OM) is obscured by the Mirror Support Platform (MSP). At the upper right there is the Focal Point Assembly (FPA) hosting the EPIC MOS (green/black) and PN (violet) detectors, as well as the Reflecting Grating Spectrometer (RGS, light blue). Image courtesy of Dornier Satellitensysteme GmbH, modified.

The *X-ray Multi-Mirror* Mission (*XMM-Newton*, Jansen et al. 2001) of the European Space Agency (ESA) was launched in December 10th, 1999 and provides simultaneous observations from the Optical/UV to the X-ray band of the electromagnetic spectrum. It carries two distinct kinds of telescopes: three X-ray telescopes with three European Photo Imaging Cameras (EPIC) and two Reflection Grating Spectrometer (RGS) in total, furthermore a 30-cm Optical/UV telescope (Optical Monitor, OM). The mission was formerly planned to end in December 2012, but was extended to the end of 2014. The large effective area of a total of 4650 cm^2 at 1.5 keV, and the possibility to obtain long exposure observations up to 40 hours enables high sensitive, simultaneous measurements in the two energy bands.
With a payload of ≈ 4 t and a spacecraft size of 10 m it is the largest scientific satellite currently operating in space. A sketch of the *XMM-Newton* payload is shown in Fig. 4.1.

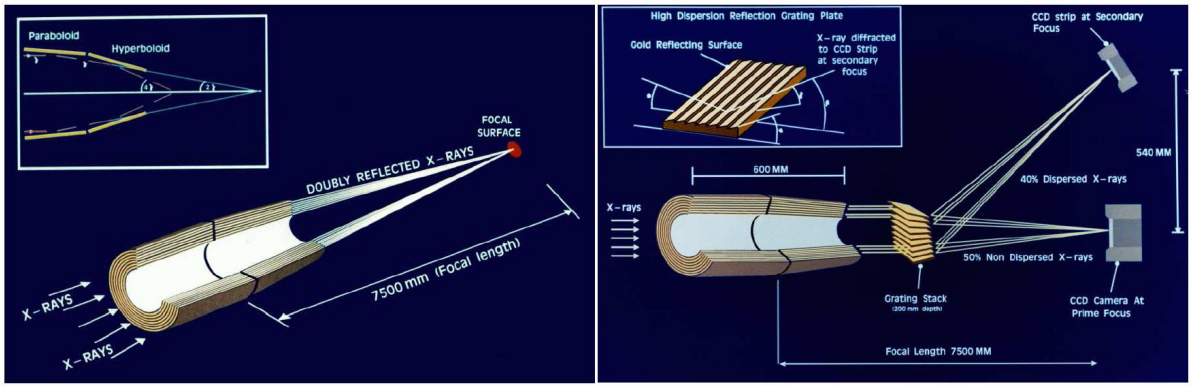

Figure 4.2.: Light paths of the X-ray telescopes. The mirrors are composed of a paraboloid ending in a hyperboloid, which focuses photons in the EPIC detectors located in the 7.5 m distant focal point. Two telescopes carry a RGA which diverts half of the incident flux on the RGS detectors. Credit: ESA/*XMM-Newton*

It consists of four main elements: the Mirror Support Platform (MSP) contains the mirror modules of the different X-ray telescope Assembly (FPA), which also contains data handling and power distribution units of the cameras. The MSP and FPA are maintained in relative position by a 6.8 m long telescope tube hosting two aperture stops. The fourth element, the Service Module Platform, is not shown in the sketch. It contains spacecraft subsystems and associated units, two solar-array wings, a telescope sun shield and two S-band antennas.

This chapter gives an overview of the X-ray telescopes and instruments EPIC and RGS, with special emphasis on the EPIC detectors, whose data is analyzed in this work. For a more detailed documentation interested readers are referred to the *XMM-Newton* Handbook (ESA (2012)) as well as the mission's official homepage of ESA[1].

4.1. The X-ray multi-Mirror telescopes

Using total external reflection to focus the incident photons, each X-ray telescope of *XMM-Newton* consists of 58 shells of high-precision Wolter-I mirrors, made of Nickel with a thin layer of gold. A sketch of a Wolter-I configuration is given in Fig. 4.2 together with the light paths of the telescopes. It is composed of a paraboloid which reflects photons on a concave surface of a hyperboloid, where they are eventually focused in the focal point and detected by EPIC detectors. Two of the telescopes carry an Reflecting Grating Array (RGA) just behind the mirror modules, which diverts 50% of the incident flux onto RGS cameras, also located in the focal plane, in order to allow high resolution spectroscopy. Taking into account further structural obscuration only

[1] ESA *XMM-Newton* Mission homepage: http://xmm.esac.esa.int/

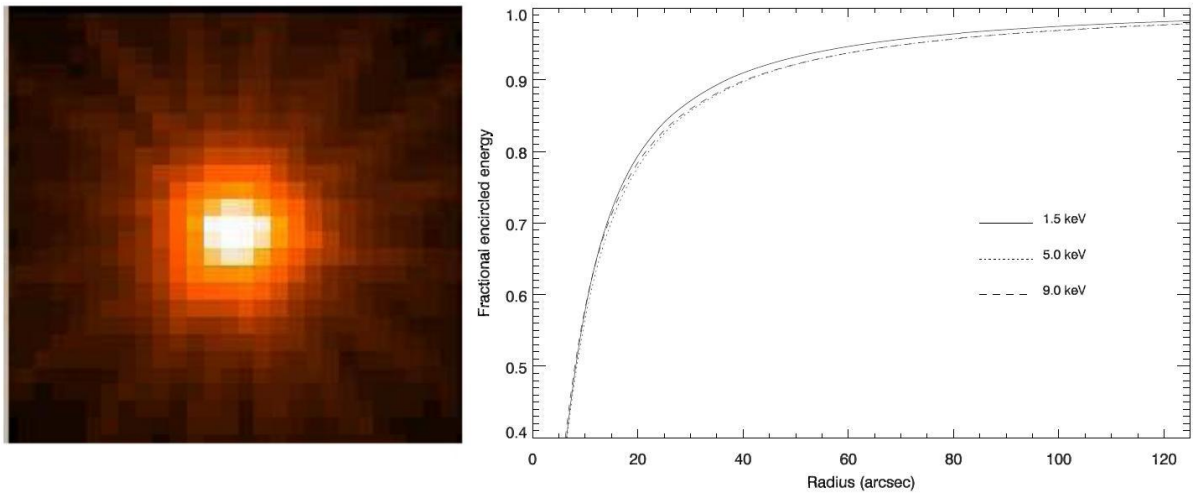

Figure 4.3.: Left panel: Shape of the on-axis Point Spread Function of EPIC PN. Right Panel: PN Encircled energy from PSF integration versus the angular radial distance from the peak of intensity. Credit: ESA/*XMM-Newton*

44% of the original flux converges in the EPIC detectors of these two telescopes. The third telescope has an unobstructed beam and collects all of the incident flux.

4.1.1. Point-Spread Function and Effective Area

The PSF expresses the ability of the mirror modules and its respective cameras to focus and resolve photons. The PSF of *XMM-Newton* is very narrow in the $0.1-6\,\mathrm{keV}$ energy range with slight increase for higher energies above 6 keV. The shape of the EPIC PN on-axis PSF and its encircled energy with angular distance to the maximum intensity is given in Fig. 4.3. As one can see, for a point-source the PSF is circular with substructures caused by the mirror holdings. Also visible is the slight energy dependence of the PSF. Nevertheless, 90% of a point-source is confined in a circle of approximately $30-40\,\mathrm{arcsec}$. With further distance to the optical axis the PSF becomes elongated as high energy photons are less confined but redistributed into wings of the PSF. Hence, the encircled energy depends on the extraction radius and position of the point-source in the field of view (FOV).
Another important parameter for the telescope performance is the effective area of the mirror modules, which is a measurement of how many photons can be collected and detected by the mirrors and its cameras. Fig. 4.4 shows the effective area of all science instrument (EPIC PN, MOS 1, MOS 2 and RGS 1, RGS 2), folded with the instruments response, i.e. the effective area of the mirrors scaled with the CCD camera's quantum efficiency. It shows that *XMM* mirrors are most effective in the $0.1-10\,\mathrm{keV}$ range, with a maximum at 1.5 keV. There is a pronounced edge near 2 keV associated with the M edge of Gold. Obviously, the effective areas of EPIC MOS cameras with RGA in the

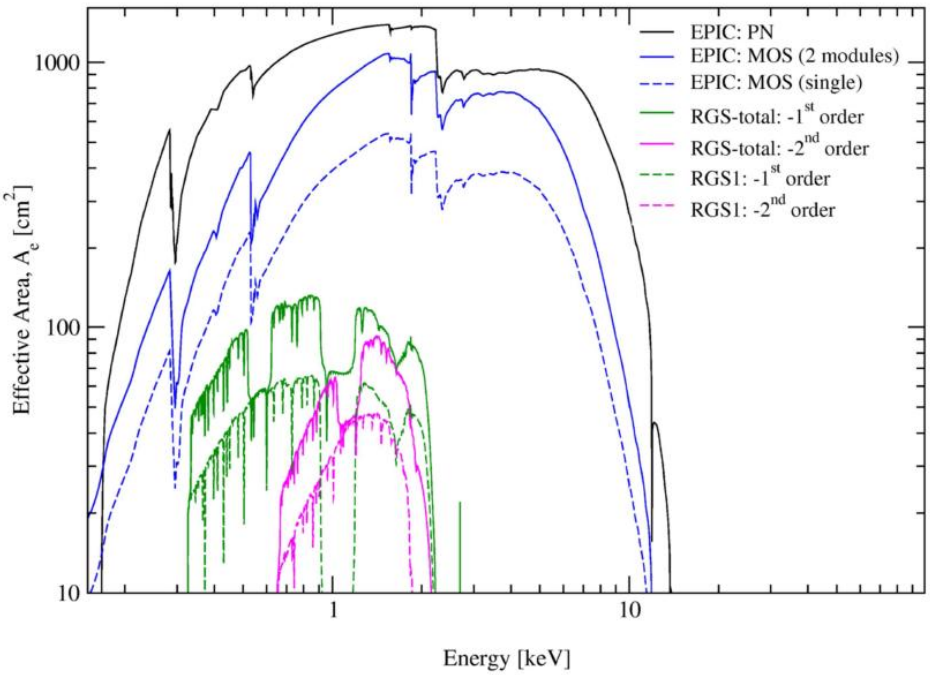

Figure 4.4.: Net effective area of all *XMM-Newton* X-ray telescopes, EPIC and RGS, in logarithmic scale. Credit: ESA/*XMM-Newton*

beam are lower than the one without, since they only detect part of the incident flux. The effective area of the RGS has broad gabs. These are due to inoperative CCDs on the RGS Focal Camera which have failed during the mission. Several absorption edges are visible associated with passive layers in the X-ray path within the telescope.

4.1.2. The European Photo Imaging Camera

The EPIC detectors of the two telescopes, that host RGA are Metal-Oxide Semiconductor (MOS) CCD cameras (called EPIC MOS 1 and 2, Turner et al. 2001) with seven identical front-illuminated CCD chips, with the central CCD being in the focal point of the converged X-ray beam. Its geometry is illustrated in Fig. 4.5. Each CCD is made of a matrix of 600x600 pixels. On the contrary, the third detector in the unobstructed beam is a PN semiconductor CCD camera (called EPIC PN, Strüder et al. 2001) of twelve identical backside-illuminated CCD chips in spatial uniform distribution, also shown in Fig. 4.5. Both cameras work in photon-counting mode, i.e. for every photon incident on a pixel, associated attributes (e.g. detector position, arrival time, photon energy) are written as a new line of an event list, that is created for every CCD chip. Despite that, both cameras are fundamentally different, especially in terms of chip geometry and readout times. For EPIC PN each channel of a CCD chip has its own readout node that works parallel. This allows fast readout times of 73 ms (down to 0.03 ms in timing

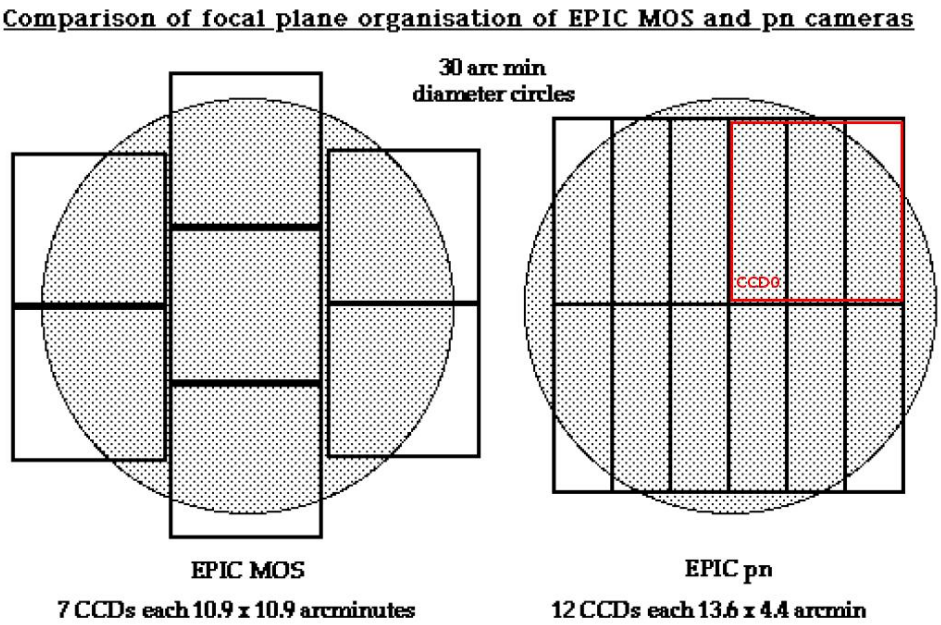

Figure 4.5.: Geometry of the two distinct EPIC detectors. EPIC MOS (left) has seven CCD chips with 600x600 pixels, read out sequentially with two readout nodes for every CCD chip. The focal point is in the center of the CCD array. In contrast EPIC PN (right) consists of twelve CCDs with 200x64 pixels and 64 readout nodes which allow parallel readout of 768 pixel channels. The focal point is on the lower half of the CCD0 in the first quadrant (red). Credit: ESA/*XMM-Newton*

mode). On the contrary, the EPIC MOS cameras are read out sequentially with only two readout nodes per CCD, with a basic readout times of 1.5 ms. Short readout times become important when bright X-ray sources are observed in oder to avoid pile-up, i.e. when more than one photon incidents overlap in time and position between two readouts times. This yields that multiple photons are regarded as one, which shifts soft X-ray photons to higher energies. A way to avoid pile-up is to shorten the integration times of the camera, which is done in different operation modes by reducing the area to be read out. EPIC detectors can operate in various different modes. An overview and description of the different operating modes of the EPIC detectors is given in the XMM Handbook (ESA 2012), Strüder et al. (2001), or Turner et al. (2001). Both types of cameras have a field of view (FOV) of approximately 30 arcmin and moderate energy resolution of $E/\Delta E \approx 20 - 50$. The energy resolution of the EPIC PN depends on the photon energy and event pattern. It is determined by statistical fluctuation of the ionization process inside the CCD and electronic noise of the readout nodes. The small pixel sizes of the CCD cameras (corresponding to less than 4 arcsec on the sky) yield that the angular resolution is determined by the point-spread function (PSF) of the mirror module.

Instrumental Background

When analyzing EPIC spectra a detailed knowledge of the camera background is required. EPIC background can be divided into electronic noise, particle induced background and X-ray photon background (XRB).

Electronic noise: Part of the instrumental background is electronic noise which originates from readout noise. In general this background shows no variation during an observation, (Carter & Read 2007).

Particle induced background: Another part of instrumental background comes from high energy particles and solar soft protons that interact with the detector itself or its surrounding and induce fluorescence detected by the CCDs. Soft protons of energies less than 100 keV may be reflected by *XMM* mirrors. The spatial distribution is restricted by the vignetting of the mirror modules and, thus, confined in the FOV (Carter & Read 2007). Its occurrence is highly unpredictable and in form of flares, which have count rates up to a hundred times higher than the quiescent level. Fig. 4.6 shows a background light curve observed with EPIC MOS 1 during an observation affected by a proton flare.

A more stable component is caused by high energy particles with only slight variations during observations. It affects the whole FOV, since it is not affected by vignetting. The spectrum of this background is rather flat with a number of fluorescence lines from the detector and surrounding. For PN, lines of Al-Kα, Cn-Kα, Ni-Kα and Z-Kα have been observed (see Fig. 4.6), (Carter & Read 2007 and ESA (2012)).

X-ray photon background This component can be divided into hard and soft X-ray photons. The former is due to unresolved AGN within the FOV and single-reflection into the FOV by out-FOV sources. Furthermore various unresolved sources, like the Galactic Halo/Disk as well as Solar winds Charge exchange, can contribute to the soft X-ray background. Both components are temporarily stable during observations. In times of low background this component dominates over the internal background below 5 keV. (Carter & Read 2007)

A full background spectrum of the EPIC PN camera is shown in Fig. 4.6, observed with closed filters in the 0.2-18 keV range. Prominent fluorescence lines due to internal particle interactions are visible, as well as, high detector noise below 0.3 keV that causes higher uncertainties in this energy range of the measured spectrum.

4.1.3. The Reflecting Grating Spectrometer

The RGS (den Herder et al. 2001) is *XMM-Newton*'s instrument best suited for high-resolution spectroscopy. It makes use of the dispersion of X-rays with different wavelength due to total external reflection off grating assemblies (RGA) in the converging

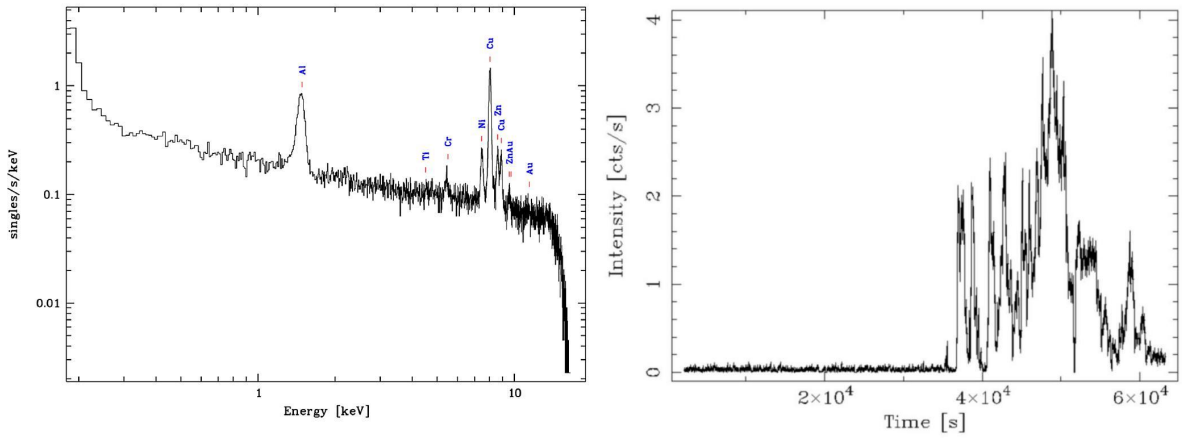

Figure 4.6.: Left panel: Background spectrum of EPIC PN. Right panel: An EPIC MOS lightcurves of an observation affected by a soft proton flare. There is a dramatic and highly variable increase of the count rate at the end of the observation. Credit:ESA/*XMM-Newton*

beam of two X-ray telescopes. They operate in the $0.35 - 2.5\,\mathrm{keV}$ $(38 - 5\,\text{Å})$ range, thus, covering a range with a high density of X-ray emission lines, including K-shell and L-shell transitions of light and heavy elements, such as Fe or Ni. The RGA intercept with the X-rays and reflect half of the incident flux on the RGS Focal Camera (RFC). The two RFC are located in the focal plane with a slight offset with respect to each other along the dispersion direction to ensure continuous coverage of the low and high energy range.
The X-rays strike the gratings with a grazing angle α and emerge with an dispersion angle of β (see Fig. 4.7). The dispersion angle β is related to α and the X-ray's wavelength λ through the dispersion equation

$$m\lambda = d(\cos\beta - \cos\alpha), \tag{4.1.1}$$

where m is the spectral order and d is the grating spacing. The first and second order are resolved in by the RFC. The third order already has a count rate eight times lower than the one of the second order. According to Eq. 4.1.1 the dispersion angle β, which is related to the position on the CCD, is associated with the photon's wavelength or energy. The order overlap of first and second oder maximum of different wavelengths is separated using the pulse height versus dispersion angle distribution (see Fig. 4.8). Different orders are clearly separated depending on the dispersion angle and photon energy, associated with the pulse height.
The Line-Spread-Function (LSF) of the RGS is a convolution of the mirror response function and the gratings, as well as with the detector response. Each component varies differently with photon wavelength which produces a number of different line shapes. The LSF presents broad and asymmetric wings, resulting from the convolution of the

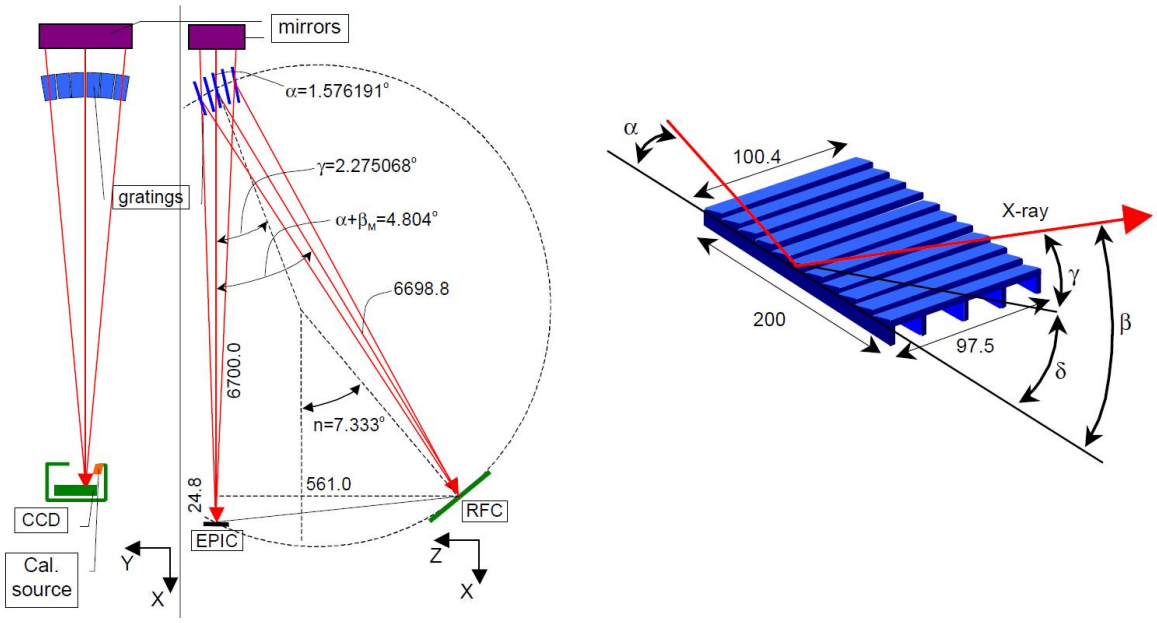

Figure 4.7.: Left: Scheme of the RGS design: X-rays (red) enter the mirror modules at the top and for two telescopes reflected the the RGS Focal Cameras (RFC). Right: Scheme of the a grating in the RGA. Also shown are the grazing angle α and dispersion angle β. Credit: den Herder et al. (2001)

three responses. The resolving power of the RGS is therefore constrained by the LSF. Nevertheless, the high-spectral resolution of the RGS is about $E/\Delta E \approx 1200$ at 15 Å in first order and $E/\Delta E \approx 700$ at 15 Å in second order. Thus, two magnitudes better than of EPIC. The wavelength accuracy is about 7 mÅ.

RGS Background

As in EPIC (Sect. 4.1.2) the background of the RGS instruments consists of multiple components. Because of the energy range of $0.35 - 2.5$ keV, minimum ionizing particles and soft protons can be rejected by on-board calibration, since most of their energy is deposited outside this energy range. Further background arises from cosmic rays and electrons which enter the telescope and cause fluorescence lines by interacting with the housing. Furthermore, internal calibration sources, i.e. the α emitter ^{244}Cm and the Al target or Teflon target, which produce Al Kα and F Kα fluorescence lines, can contribute to the background. However, these can be modelled as a two dimensional Gaussian distribution. Another stable component is the readout noise of the electronic register.

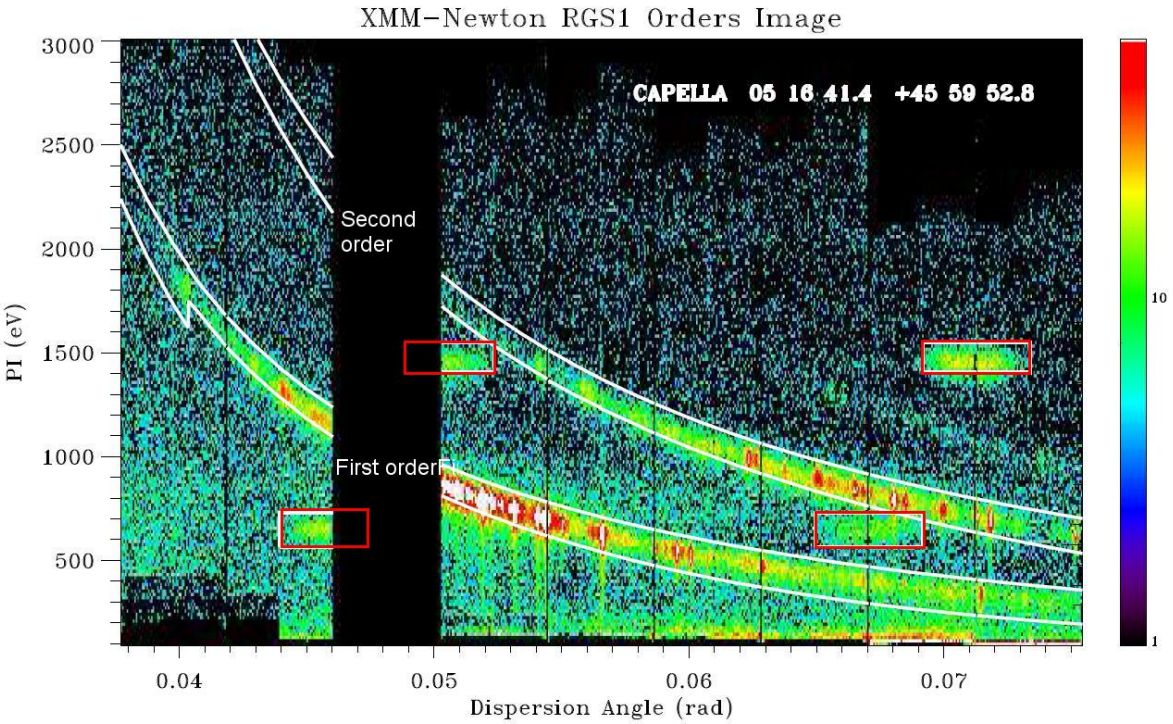

Figure 4.8.: Example of a spectral order image. The pulse height (PI), associated with the photon energy, is plotted against the dispersion angle β. The color scale represents logarithmic intensity scale. In this plot first and second order events are clearly separated. Emission of the calibration sources (red) are also visible, ESA (2012)

.

5. Data reduction

This section describes the data reduction which was performed manually for all sources. A detailed description of the reduction pipeline and commands can be found at ESA (2012) Handbook. All data was taken from the publicly available *XMM* Science Archive[1] that provides observation data files (ODF) created by the Survey Science Center standard pipeline processing. For the reduction the most important files of the ODF are event lists for every instrument and CCD and the auxiliary files. Reprocessing and analysis of the data, as well as, extraction of spectra was done with `SAS v11.0.0`[2]. A scheme of the reduction process is depicted in Fig. 5.1. The following subsections describe the reduction in more detail, but to give a short summary: for every observation images of the entire field of view were created to define the source and background region. Furthermore, light curves were extracted for the FOV, the source region and background region in order to check for flaring particle background associated with soft protons and to create filtered event lists. Source/background spectra were generated from these filtered event lists, so were the detector response files (rmf/arf).

[1] *XMM*-Newton Science Archive, XSA: http://xmm.esac.esa.int/xsa/
[2] Science Analysis Software, SAS: http://xmm.esac.esa.int/sas

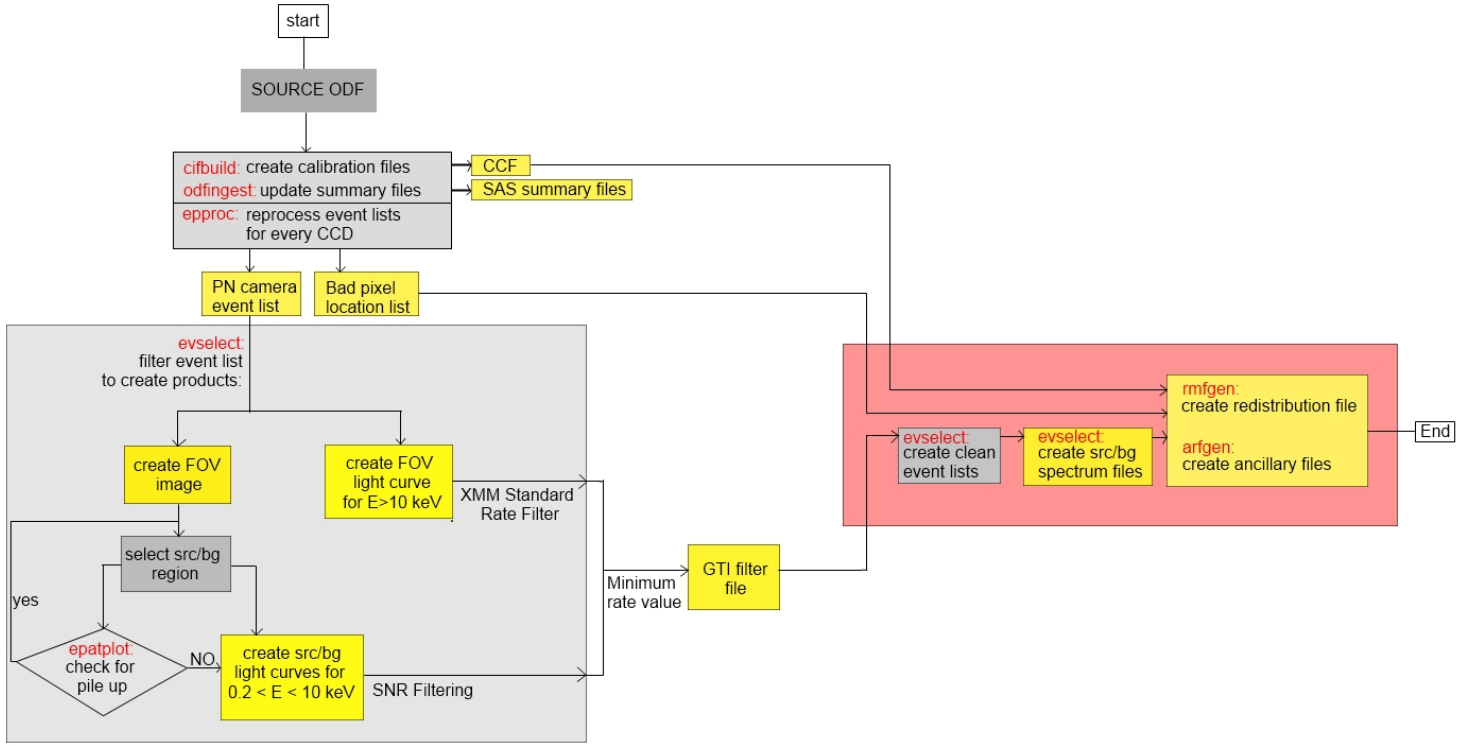

Figure 5.1.: Scheme of the data reduction process. Yellow boxes symbolize the creation of files, grey boxes represent tasks. For further information see text.

Data Preparation

For each observation the ODF were downloaded from the XSA and reprocessed in the following way:

- latest calibration files, until September 2011, were generated using the `cifbuild` command,
- in order to regard recent software developments and updated calibration files the pipeline products were reprocessed and updated using the EPIC PN reprocession meta task `epproc`. This produces updated imaging event lists for every CCD of the EPIC PN instrument and a list of bad pixel locations. Pixels flagged as bad are not taken into account in further data analysis.

All products (images, light curves, filtered events lists and spectra) can be obtained using the `evselect` command, which filters the image event list according to user-specific selection criteria.

Images and region definition

An an image is extracted with `evselect` for a coordinate binning of 80 pixels (standard bin size). The source region was defined as a circle centered at the the highest signal. The background region was defined from a source-free region from the same CCD like the source with similar distance to the readout node. This way the background region is effected by similar amount of electronic noise[3]. If this was not possible the background region was taken from a neighboring CCD, but with equivalent distance to the readout. All sources appear as point sources in the XMM FOV, with a maximum extraction region of 50 arcsec. Fig. 5.2 shows an *XMM* image of Mrk3, including the source and background region. Also shown is IXO 30. Bianchi et al. (2005) analyzed this X-ray source and found no significant contribution to the Mrk 3 spectrum.

Light curves and pixel patterns

Based on the selected source and background region light curves with a time bin size if 100 s were created for events in the energy range of 0.2-12 keV, in addition to one for the entire FOV and energies higher than 10 keV. The latter was extracted to check for flaring particle background following standards method described below (ESA (2012)). A further selection criterion was put on the pixel pattern of the events. Patterns of CCD pixels refer to the combination of pixels that are hit by one photon. Fig. 5.3 presents the 13 valid patterns for EPIC PN data. Higher patterns than quadruples are not created by single photons, but affected by pattern pile-up. Single patterns have the most accurate

[3]XMMCALIBRATION 0018 sec 5.2: available at http://xmm2.esac.esa.int/

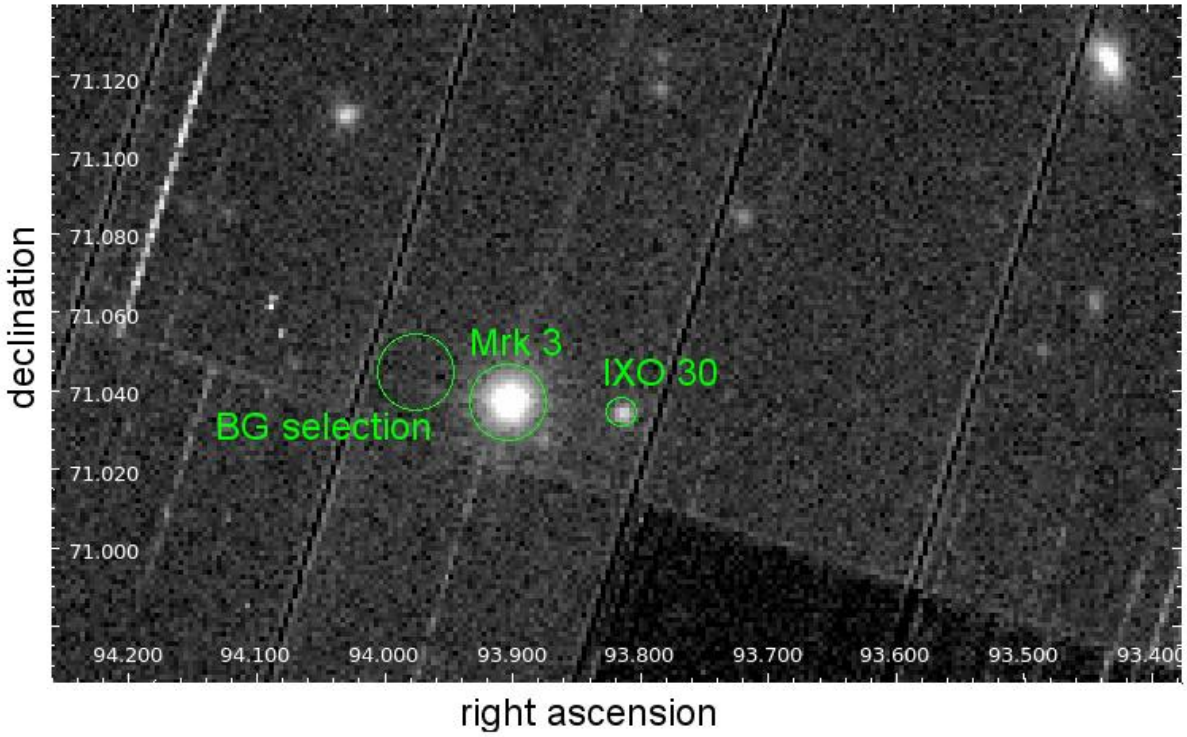

Figure 5.2.: XMM FOV image of Mrk 3, observation ID 0111220201. Large green circles mark the extraction region for the source and background spectrum of Mrk3. Also marked is IXO 30.

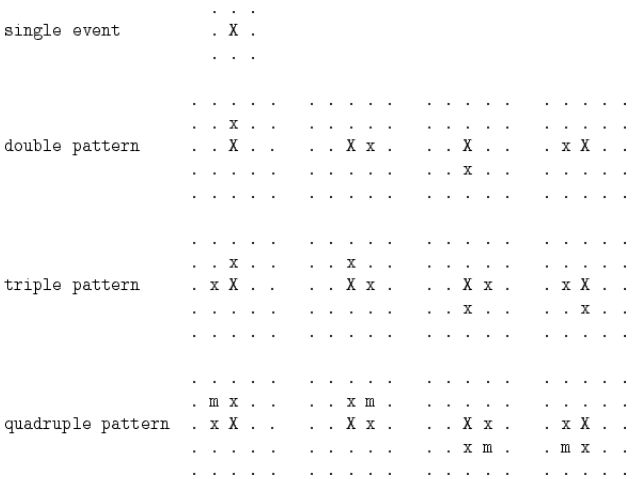

Figure 5.3: Pixel patterns of EPIC PN camera. 'X' marks the pixel with maximum charge, 'x' a pixel with non-maximum charge and 'm' a pixel with minimum charge. Dots mark pixel which do not detect an event. Credit: ESA (2012)

energy resolution. According to calibration reports single and double event patterns are calibrated well enough for spectral analysis and soft protons are commonly observed as single pattern events. The light curves of the FOV are therefore extracted for single events only, while thoseof the source and background region also include double events.

The flaring particle background is highly variable with time and exhibits count rates of one or more orders of magnitude higher than the low-background or source count rates. Good time intervals (GTI) of low-background periods can be defined using `tabgtigen` and setting a maximum threshold for the count rate, slightly higher than the one of the low background. The standard threshold is 0.4 cts/s for EPIC PN ESA (2012). Another method to define the rate limit was established by Piconcelli et al. (2004), which is especially suitable for bright sources. The underlying idea is to look at the Signal-to-noise ratio (SNR) of the source to background count rates and filter out those time interval's for which the background has a significant effect on the SNR. GTI files were created for the minimum of the thresholds derived by both methods. Because of the low count rates, however, both selection methods yielded equal results, since the count rate of low-background periods was lower than 0.4 cts/s.

Filtered event lists and spectra

Using the region and GTI information the image event list was filtered to accelerate the extraction of spectra and response files, for a smaller amount of events has to be processed. The selection criteria for the filtered event lists were

- pixels were not flagged as bad pixel,
- inclusion pixel patterns of single and double events,
- selection of events in GTI only.

Then source and background spectra were extracted from the filtered event list for the respective region and an energy range of 0.2-12 keV, with 5 keV energy bin size. Based on the spectrum file the photon redistribution matrix file (rmf)and ancillary region file (arf) were generated using `rmfgen` and `arfgen`, respectively. Those tasks take into account the energy range, region and bad pixel locations taken from the bad pixel list. Response files describe detector effects on the observed spectrum, such as effects of vignetting or the effective area, the probability of a photon to be detected as event and the transfer from the discrete pulse height space to the continuous energy space. To account for these effects the spectrum is folded with both response files by the fitting program. All spectra are presented in Sect. A.2.

Pile-up

The filtered event lists are furthermore filtered for the source region is also checked for pile-up. Pile-up occurs when multiple X-ray photons arrive in the same or two neighboring pixels during one readout frame and treated as a multiple pixel pattern event. This has an effect both on the PSF and spectral shape, since multiple photons are added up to one with a combined energy. The effect in the spectral shape is an artificial

hardening, because multiple soft X-ray photons are regarded as one hard photon. On the other hand, the PSF suffers from the high count rates in the center, which yields an artificial hole. The suppression of high count rates also alters the light curve of the source. A way to minimize the effect of pile-up is to only regard single-pixel events which are least effected by pile-up. As pile-up is a result of high count rates each EPIC instrument has a maximum limit for count rates for which this effect can be neglected. The limit for EPIC PN is of the order of 10^{11} erg s^{-1} cm−2 in the 0.15-10 keV energy range. A standard diagnostics test was performed on the source region, using the tool `epatplot`. This utilizes relative ratios of single and double events and compares them with the standard values. As long as the ratios follow standard curves pile-up is neglible. For compton thick sources are weak sources with count rates much below the pile-up limit for EPIC PN, the event lists are not effected by pile-up for the whole sample.

6. Statistical Methods and spectral modeling

This chapter describes statistical methods used in the analysis. Statistical tests treat the question whether a sample is consistent with a certain hypothesis, called null hypothesis. For this a test statistic t is defined and the value t_0 is calculated for the sample. The probability that under the assumption of the null hypothesis, a sample yields a test statistic $t_0 \geq t_c$ is expressed by the p-value. The critical value t_c corresponds to a certain significance level α, commonly 5%, for which the null hypothesis can be accepted. It depends on both the test and size of the sample. If the p-value is lower than α, the null hypothesis has to be rejected.

6.1. Spectral modeling

In spectral modeling these tests are used to compare the spectral data counts with a theoretical model. The spectral range is divided into discrete interval's (bins) for which the model predicts a number of data counts, based on model dependent parameters. In spectral analysis, bins are commonly wavelength or energy bins. The statistical test is used to quantify whether a number of spectral counts within a bin is consistent with the number of predicted counts, assuming a specific probability distribution function. The Goodness-of-fit is expressed by a specific fit statistic t. The aim is to change model parameters in order to minimize t, thus achieving the maximum likelihood, that the observed counts can be explained by the model. The way the parameters are changed is determined by a minimization algorithm (fit method). In this analysis a Levenberg-Marquardt minimization algorithm is used, which computes the gradient of the fit statistic in order to minimize the statistical value. The two commonly used fit statistics, which are also used in this analysis are the Cash statistic (Cash 1979) and χ^2-statistic. These are logarithmic-likelihood functions ln L, which assume different probability distributions function $P(X_i; M_i(\Theta))$ for the counts within one energy bin. Here X_i are the observed counts of the spectrum $\{ X_i;\, i \in [0, N]\}$ for each energy bin i and M_i describes counts predicted by the model with the parameter set Θ. The latter, χ^2-statistic, assumes a Gaussian distribution of counts per energy bin and the logarithmic-likelihood reduces to

$$t = \chi^2 = \sum \frac{(X_i - M_i)}{\sigma_i}, \tag{6.1.1}$$

in the optimized version, where the model independent part is neglected. The denominator σ_i is a data independent standard derivation of the Gaussian distribution. It is therefore not suitable for low-counts spectra, which follows Poisson distribution (Nousek & Shue 1989). This is assumed in Cash statistic that is expressed by the C-value

$$t = C = 2 \sum_i \left(X_i \ln M_i - M_i \right). \tag{6.1.2}$$

In case of a large number of data counts, Cash and χ^2-statistic are equally suited. In this analysis Cash statistic is used for spectra with less than 20 counts per energy bin. Another expression for the Goodness-of-Fit is the reduced statistical value, that is the χ^2 or C-value divided by the number of degrees of freedom (d.o.f.), i.e. the number of used energy bins minus the number of free parameters of the model. Pearson (1900) derived for χ^2-statistic that this should be around unity. If the reduced χ^2 is lower than 1, the uncertainties σ of the counts are overestimated. This also holds for the reduced C value Cash (1979).

6.2. The F-Test

The F-test compares the variances s_n, s_m of two samples of sizes n and m, with the same probability distribution function P. The test statistic is defined as the ratio of these variances F:

$$t = F = \frac{s_n}{s_m}, \tag{6.2.1}$$

where it is convention of choose the ratio such that $F \geq 1$. F follows an F-distribution, which is asymptotic to a Gaussian distribution for large samples. The p-value is determined from the F distribution. The F-test is used to compare a fit statistic results χ^2/d.o.f. of a simple model A with the one of a more complex one B, in which the simple model A is nested. In case the null hypothesis is rejected both models are statistically significantly different.

6.3. Two-Sample Kolmogorov-Smirnov Test

For two samples of data $A = \{ X_i;\, i \in [0, n] \}$ and $B = \{ Y_i;\, i \in [0, m] \}$, where $n, m \in \mathbb{N}$ are the number of elements in the respective sample, the two-sample Kolmogorov-Smirnov Test (KS-test) compares their distribution functions $F_A(X)$ and $F_B(Y)$ under the null hypothesis that both samples share the same underlying distribution:

$$H_0 : F_A(X) = F_B(Y).$$

The alternative thesis is that the sample are drawn from different distributions:

$$H_0 : F_A(X) \neq F_B(Y).$$

The KS-test uses the maximum difference t of both distributions

$$t = \max |F_A(X) - F_B(Y)|$$

as test statistics. The null hypothesis is then rejected at a given significance level α if $p \geq \alpha$, meaning that t exceeds a critical value t_c the difference between both distributions is too large and the two samples are independent. Critical values t_c depend on the size of the sample and are listed in tables publicly available.

6.4. Correlation coefficients

The correlation coefficient is a measurement to quantify the level of correlation between two random variables X and Y. For a two dimensional probability distribution function $f(X, Y)$ the correlation coefficient ρ is defined by the covariance V_{xy} and the expectation values μ_x, μ_y of X and Y:

$$V_{xy} = \int_{-\infty}^{+\infty} X\, Y\, f(X, Y)\, dX\, dY - \mu_x \mu_y \tag{6.4.1}$$

$$\rho = \frac{|V_{xy}|}{\sqrt{\sigma_x^2 \sigma_y^2}} \in [-1, +1]\,, \tag{6.4.2}$$

where σ_i^2 is the variance of the one-sided probability distribution function $f(X)$ and $f(Y)$. For independent variables $f(X, Y) = f(X)f(Y)$ thus $V_{xy} = 0$, which implies $\rho = 0$. However, the reverse is not necessarily true. If two variables are fully correlated $|\rho| = 1$.

7. Analysis of the hard X-ray spectrum of the XCTA-Sample

This chapter summarizes the analysis of the HX-subsample (see Chapt. 3) and the model fitting of the 3-10 keV range (referred to as hard X-ray range, hereafter). The analysis was carried out with `XSPEC v12.7` Arnaud (1996). Information about spectral models, which are not specifically explained here, can be obtained from the Xspec Manual[1].

7.1. Motivation

The project's aim was to analyze the properties of Fe Kα for Compton-thick AGN, which yields information about the origin of the line and ionization state of the emission region. Another objective was the analysis of the spectra for the existence of the primary, photo-electrically absorbed X-ray continuum and the relative strength to the reflected component. This can yield information about the covering fraction of the absorbing torus. 28 sources of the HX-Subsample were analyzed in the 3-12 keV range; NGC 0591, NGC 3690, NGC 6240 and IC 2560 have not been analyzed due to time constraints.

7.2. Spectral Analysis

The energy range was limited to the 3–12 keV range because the soft X-ray emission in the 0.3-3 keV range was associated with emission lines originating from ionized elements in the low-density, highly ionized Narrow Line Region, irradiated by the primary X-ray continuum of the central region. The underlying assumption is that the line emission in the soft part is independent from the hard components, which can therefore be treated separately and that the low-energy component is not contributing at all above 3 keV.
Each spectrum was fitted individually. If there were multiple observations for one source whose fit parameter were consistent with each other at 90% confidence level, thus the spectra coincided in spectral shape and normalization, they were fitted simultaneously with linked parameters. In case of NGC 1068, two observations exist from two subsequent days. Since the dynamic timescale of the re-processor are of the order of months or years (Guainazzi et al. 2012), these observations were merged in order to improve the Signal-to-Noise ratio. In case of Mrk 3, there are five observations of which four took place

[1] Xspec Spectral Models: https://heasarc.gsfc.nasa.gov/xanadu/xspec/manual/XspecModels.html

between 2001 and 2002. These are similar in shape and flux and were fitted as one dataset. The fifth observation took place in 2000, when the flux decreased and hence it was treated as a single dataset. The change in flux was already reported in Akylas et al. (2006) and references therein. They find a decrease of flux of $\approx 30\%$, suggesting that there might be a variation in the column density.

For the spectral analysis, the data were re-binned based on their number of spectral data counts in 2-10 keV range and its distribution in the 5-8 keV range, where the iron line complex is fitted. Re binning can smear spectral features like emission lines, thus if the spectra did not contain enough data counts to apply χ^2 statistics, which requires at least 20 cts/bin, Cash statistics is used and the data is re-binned to 5 cts/bin. Nousek & Shue (1989) suggests an number of counts about 4-5 times the number of bins. The spectra are intrinsically binned to 5 eV, which is far below the resolution of the detector (see Chapt. 4). A bin size of 50 eV requires at least 1200 cts/bin in the 5-8 keV in order to apply χ^2 statistics.

The best-fit for each spectrum was computed using the Levenberg-Marquardt minimization algorithm (`mpfit`) Sect. 6.1 and uncertainties of the parameters were calculated at a 90% confidence level. Based on the best-fit model, one can compute the total observed integrated photon flux in the 2-10 keV range. Furthermore, the 2-10 keV flux of the `pexrav` component is computed, which is the fraction of the total unabsorbed flux of the primary continuum that was reflected in our line of sight. In order to compute the unabsorbed 2-10 keV flux of the primary continuum, the absorption component of the baseline model is eliminated and the flux is determined for the unabsorbed powerlaw alone. Thus, total unabsorbed fluxes can only be determined for sources for which a primary continuum is included in the best-fit model.

For each emission line, the equivalent width is calculated . This is a quantitative measurement of the line strength against the underlying continuum and is generally defined as

$$EW = \int_{E_{\mathrm{low}}}^{E_{max}} \frac{F(E) - F_c(E)}{F_c(E)}\, dE, \tag{7.2.1}$$

where $F(E)$ is the total flux and $F_c(E)$ is the total flux of the continuum under the line. The flux is integrated from E_{min} to E_{max} which defines by the range of spectral feature. In `Xspec`, the equivalent width is defined as the flux at the center energy of the line, instead of integrating over an extended energy range. `Xspec` measures EW64 at the center energy. Thus a contribution of the line wings is not accounted. This can be neglected for the line width is less than the size of one energy bin. In this case, 68% of the line flux falls into one energy bin, and is included in the calculation of the equivalent width.

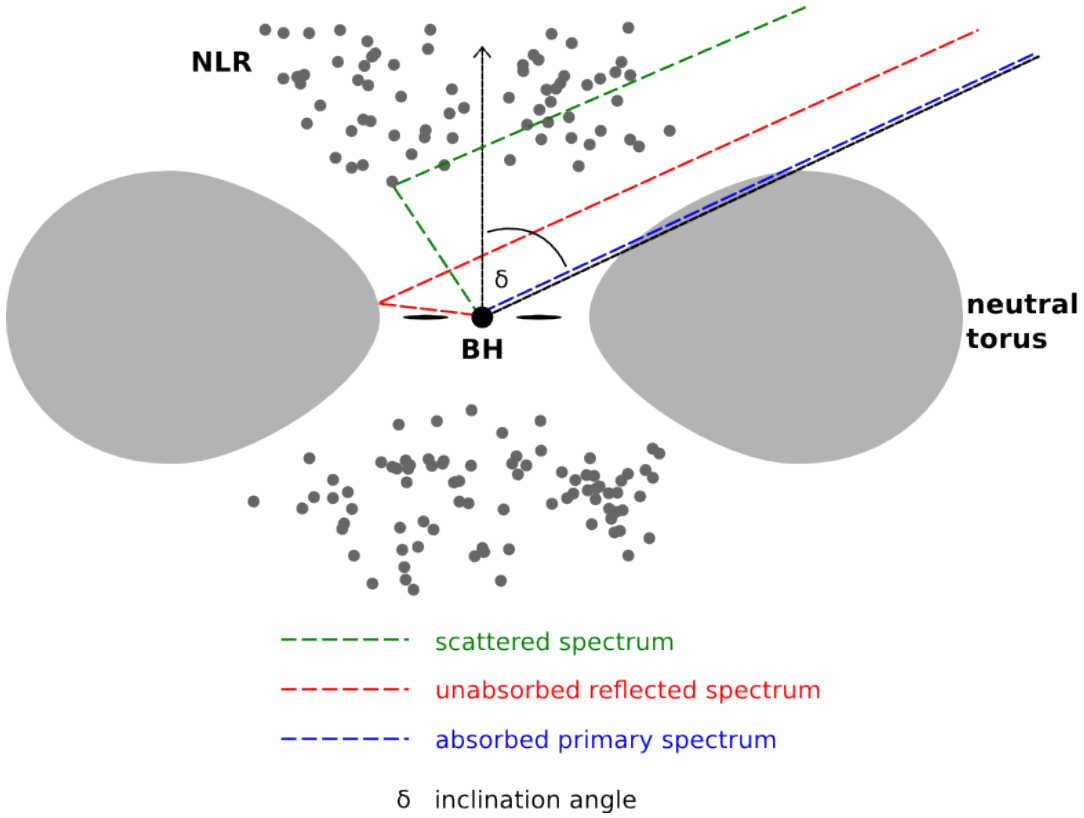

Figure 7.1.: A sketch of the scenario assumed in the baseline model. Continuum components are the absorbed continuum, seen through the torus, and the reflected unabsorbed spectrum which also yields the iron emission line complex due to fluorescence lines. A third scattered component from the NLR is considered as ionized reflection lines. Credit: R. Schulz

The baseline models

The model assumes the following scenario, illustrated in Fig. 7.1: an X-ray source, e.g. accretion disk or Corona, with a powerlaw-shaped energy distribution of the primary photons irradiates the inner walls of the obscuring torus, which is regarded neutral and in thermal equilibrium, because of its high density and low temperature. The inner walls can be locally approximated as a slab of cold electrons, that work as a compton-reflector for the primary continuum. Photons are reflected into the line of sight (l.o.s.) by the walls of the far-end side of the torus. This is modeled by the model `pexrav` (Magdziarz & Zdziarski 1995). Photons that penetrate the surface of the torus get down-scattered by Compton scattering and are eventually absorbed. The photo-electrically absorbed powerlaw was modelled by multiplying the primary powerlaw with the absorption model `zvfeabs`. It was added to the model if the fit statistic was significantly improved with respect to the additional number of parameters and if the

Table 7.1.: Overview: Spectral models

Xspec model name	physical description
powerlaw	Primary continuum.
pexrav	Neutral compton-reflection of the intrinsic powerlaw with exponential cut-off
zvfeabs	Redshifted photo-electric absorption of the primary continuum.
zgauss	Redshift corrected Gaussian line profile.

Notes:[a] in units of solar abundance [c] of the intrinsic powerlaw [c] in keV.

column density of the absorbing torus could be constrained at 90% confidence level. The F-test is used to test for statistical significance of the absorbed powerlaw. The absorbed powerlaw was included if the simple model could be rejected at 5% significance level.
The absorption of X-rays causes K- and L-shell ionization of neutral elements that deexitate by emitting fluorescence lines or the Auger effect. The most prominent line is Fe Kα due to the high abundance of iron abundance $A_{\rm Fe}$ in the central region and the high fluorescence yield Y (e.g., Matt et al. 1996a). The width of the lines is dominated by Doppler broadening with a Gaussian line profile, two redshift corrected Gaussians were added to the model to account for the neutral Fe Kα and its Compton Shoulder (Matt 2002b).
Once the continuum and the iron line were modelled, further emission lines were added to account for remaining residuals, such as Fe Kβ and Ni Kα. In addition, tests for ionized emission lines like Fe XXV Kα and Fe XXVI Kα were performed, until the best-fit model was found. Ionized emission lines are associated with emission from the NLR that absorbs, re-emits and also compton-scatters the primary continuum in our line of sight. An overview of the models is given in Tab. 8.2. The two possible models are:

1. A (reflection only): $C = \texttt{pexrav}(\Gamma, A_{\rm Fe}, N) + \sum_i G_i(E, N, \sigma)$,
2. B (mixed model): $C = \texttt{pexrav}(\Gamma, A_{\rm Fe}, N) + \texttt{zvfeabs}(N_{\rm H}, A_{\rm Fe}) \cdot \texttt{powerlaw}(\Gamma), N) + \sum_i G_i(E, N, \sigma)$,

where C is the distribution of counts, $\sum_i \rm G_i$ symbolizes the number of Gaussians to fit the emission lines, and the photon index Γ, the iron abundance $A_{\rm Fe}$, the normalization N, the line energy E and line width σ represent the free model parameters.

`pexrav` is a model for Compton reflection developed by Magdziarz & Zdziarski (1995). They assumed a plane-parallel, semi-infinite slab of cold electrons that is irradiated by a source of X-ray and soft γ-ray photons with an angular-distribution $\rm I \approx \cos^{-1}\Theta$ of the intensity, where Θ is the inclination angle of the incident photons with respect to the slab normal. Furthermore, they assumed a cut-off powerlaw spectral distribution of the incident photons. They computed angle-dependent Green's functions for the non-relativistic limit and relativistic regime, treating both single and multiple Compton scattering and bound-free absorption. Fig. 7.2 shows Monte-Carlo simulations of the

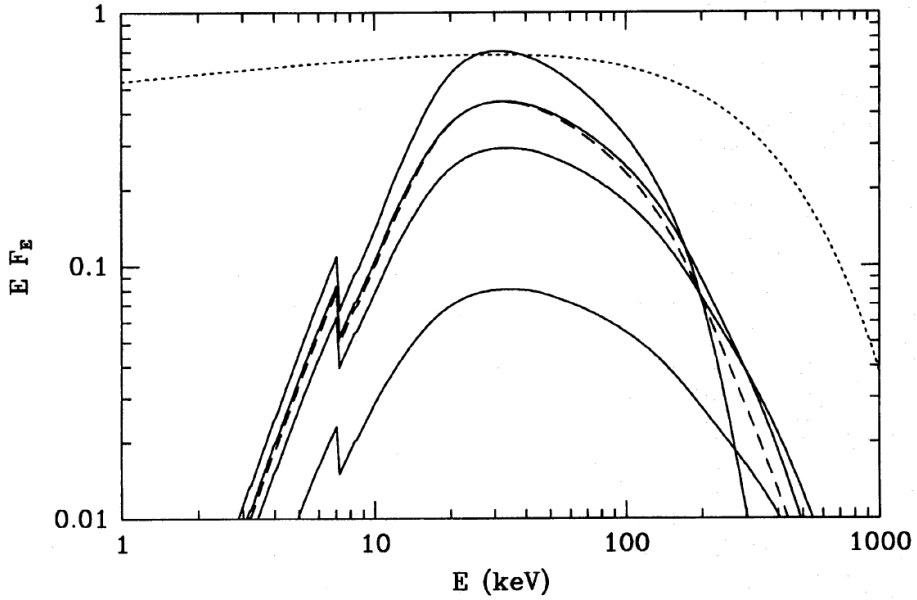

Figure 7.2.: Monte-Carlo simulations of the reflection spectrum as created by `pexrav`, for different viewing angles $\cos\Theta = 0.05, 0.25, 0.45, 0.95$, from top to bottom, respectively. The spectral index of the incident powerlaw is $\alpha = 0.9$, illustrated as a dotted line with an exponential cut-off energy at 300 keV. Also shown is the angle-averaged spectrum as a dashed line. (Magdziarz & Zdziarski 1995)

reflected spectrum (solid lines) for various viewing angles, resulting from a powerlaw with an exponential cut-off at 300 keV (dotted line). They find that the spectral shape of energies $E \leq 10$ keV does not change with increasing viewing angle, though it has an effect on the normalization of the spectrum. The spectrum for a viewing angle $\cos\Theta = 0.45$ is the one closest to the angle-averaged shape. For energies higher than 10 keV the spectrum hardens with increasing viewing angle (see Fig. 7.2). `pexrav` does not include line features, but only computes the reflected continuum.

`pexrav` is able to fit both the reflected continuum as well as the intrinsic powerlaw. The latter is included as an extra component in the baseline model, thus `pexrav` was used to model the reflected emission only (model parameter relative reflection fixed to -1). The cut-off energy of the intrinsic powerlaw was fixed at 200 keV. All metal abundances except for iron abundance were set to solar values. The iron K absorption edge was fixed to the value of neutral iron 7.11 keV[2]. Neutral lines were expected to originated from approximately the same region on the torus, thus they are effected by similar Doppler broadening. Gaussian widths of neutral emission lines were therefore linked to the one of Fe Kα, which is left free to vary. Ionized lines are generally weaker than the neutral lines. In order to test for their detection they were modelled as δ-peaks with a width

[2]X-ray Transition Database: http://www.nist.gov/pml/data/xraytrans/index.cfm

of 1 eV. In general, no constraints were put on the photon index and iron abundance except for the hard limits of the model ($1.1 \leq 2.5$ for Γ, $0.0 \leq A_{Fe} \leq 100$). However, in the case that no constraints could be found at 90% confidence level, they were fixed to literature values, if possible, or default values ($\Gamma = 1.9$ for Seyfert 2 galaxies, $A_{Fe} = 1.0$ relative to solar abundance). Because the inclination angle of `pexrav` has no significant effect on the reflected spectrum for energies E$\leq$ 10 keV, the inclination is fixed to 63°, which creates a spectrum closest to the theoretical angle averaged one (Magdziarz & Zdziarski 1995). The energy of the Compton shoulder is fixed to 6.135 keV, while its width is constrained to 35 eV (Matt 2002b).

7.3. Results

This section presents the results of the model fitting. Tab. 7.2 and Tab. 7.3 list the results for the continuum, while Tab. 7.4, Tab. 7.5 and Tab. 7.6 give further information about the detected emission lines. Fig. 7.3, Fig. 7.4 and Fig. 7.5 present six examples of the hard X-ray spectra including the fit model and residuals.
Fig. 7.6 shows the distribution of the absorbing, equivalent hydrogen column density N_H. In total there are 10 out of 29 (noted as 10/29, hereafter) sources, for which an absorbed powerlaw was detected. For the other ones, a reflection-dominated model resulted in the best fit. This suggests that the column density for these sources exceeds a value of $N_H \sim 10^{24}\,cm^{-2}$ and the fraction of the primary continuum could not is too low in order to be detected because the flux is too low, or this component is completely absorbed up to 10 keV. For 9/10 sources, a column density greater than $10^{23}\,cm^{-2}$ was measured and can be confirmed to have been in at least a mildly Compton-thick state at the time of observation. Only Mrk 231 exhibits a low column density of $N_H = (3 \pm 2)10^{22}\,cm^{-2}$, consistent with a compton-thin absorber. Furthermore, the spectrum indicates a weak neutral Fe Kα line with an equivalent width of 153^{+144}_{-124} eV. Together with the low column density this suggests that Mrk 231 has been observed in a compton-thin state. Piconcelli et al. (2013) present more recent *Suzaku*[3] observations from 2011, reporting a strong variation of the continuum flux and spectral shape since 2001, whilst the iron line flux remained constant. Fitting the 2011 *Suzaku* spectrum, they find evidence for a two-component partial-covering absorber with column densities of $N_H \sim 10^{22}\,cm^{-2}$ and $N_H \sim 10^{24}\,cm^{-2}$, respectively. This suggests that during the observation in 2001 Mrk 231 was observed through the compton-thin part of the absorber only.
The results for the equivalent width of 6.4 keV Fe Kα (EW64, hereafter) spread from a few 10 eV up to 3 keV, whilst the majority of sources present an EW64 of 200 eV - 1 keV (see Fig. 7.7), which is consistent with the published values of Compton-thick AGN. There are 7/29 sources with EW64 $\geq$ 2 keV. This is not unlikely for column densities N_H larger than $10^{24}\,cm^{-2}$ (Matt et al. 1996a). The spectra of these sources (IC 4995, NGC 1320, NGC 2273, NGC 3393, NGC 4968, NGC 5196 and NGC 7674) were best fitted with

[3]Suzaku mission: http://heasarc.gsfc.nasa.gov/docs/astroe/astroegof.html

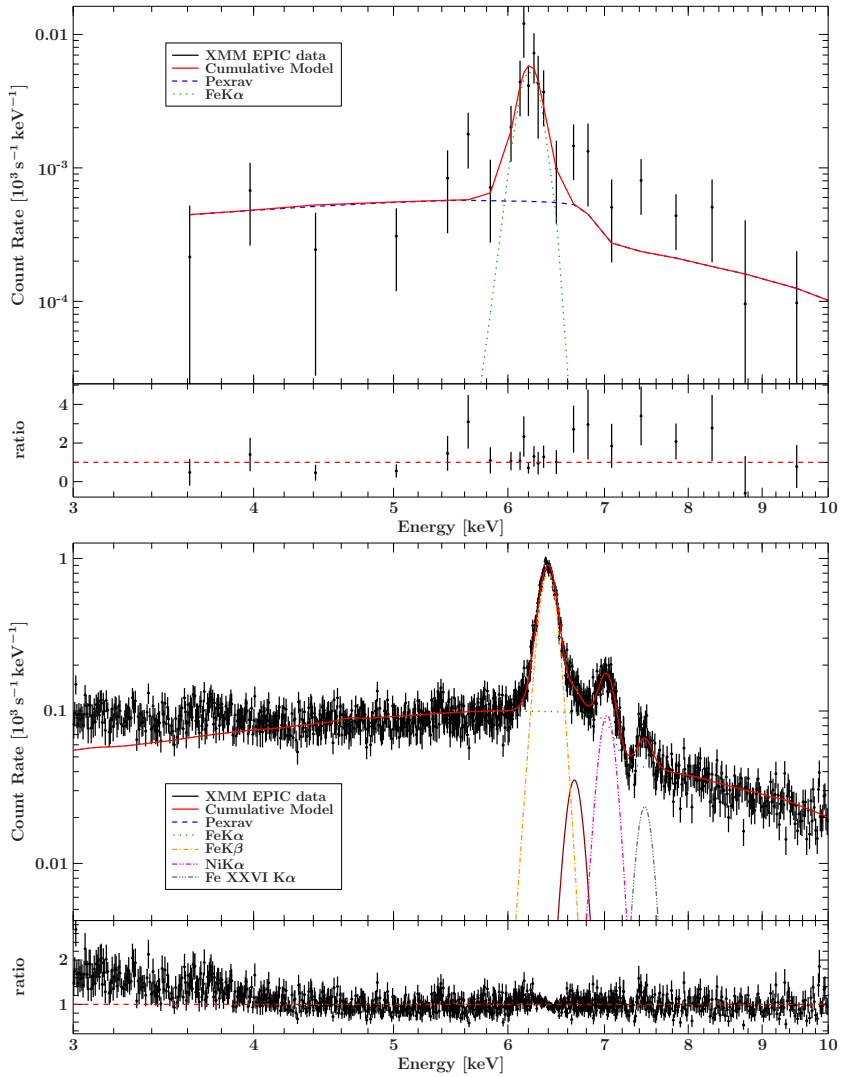

Figure 7.3.: Best-fit spectrum and model components for 2MASX J11570+5249 (upper panel) and Circinus Galaxy (lower panel).

a reflection dominated model without detecting a primary continuum component. This supports the existence of a very Compton-thick absorber. On the other hand, EW64 higher than 2 keV may be biased by the blending of multiple Fe Kα lines of neutral and low ionized iron, that are fitted as one line, due to the limited energy resolution and re-binning, which yields a larger EW64.

Fig. 7.8 shows the distribution of the iron abundance. A Gaussian fit to the histogram yields a mean of $A_{\mathrm{Fe}}/A_{\mathrm{solar}} = 1.0 \pm 0.5$. Some sources are consistent with a slight under-abundance of iron (e.g. Mrk 3 $A_{\mathrm{Fe}} = 0.70^{+0.03}_{-0.05}$). But the results should be taken with caution, for `pexrav` calculates the iron abundance based on the depth of the iron K edge at 7.11 keV of the Compton reflection component, which strongly depends on the photon

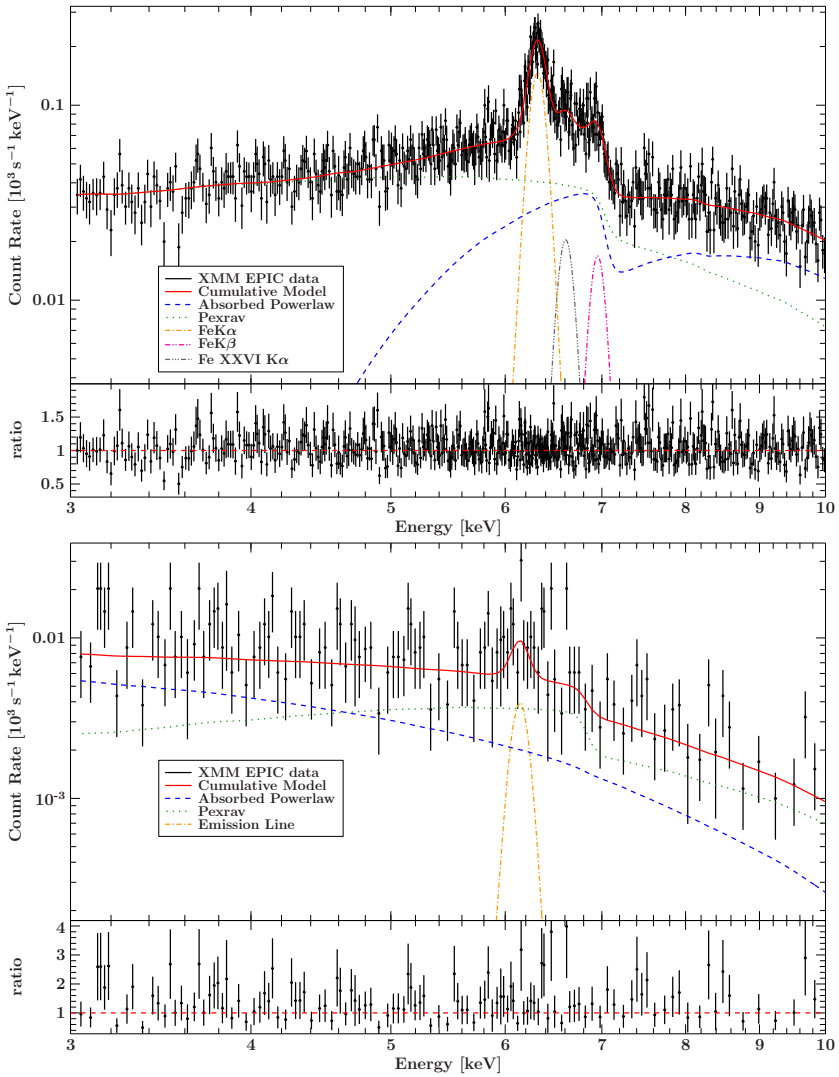

Figure 7.4.: Best-fit spectrum and model components for Mrk 3 (upper panel) and Mrk 231 (lower panel).

index and inclination angle. In addition, the edge might blend with the Fe Kβ line at $\sim 7.06\,\mathrm{keV}$ and is thus not determined correctly.

The photon index Γ of the primary continuum could be constrained in 9/29 sources. The distribution of the measurements are shown in Fig. 7.9. Most of the sources present a best-fit value of $\Gamma \sim 1.9$ within their uncertainties and agree with the typical value for Seyfert 2 galaxies. Left alone Mrk 3 has a slightly steeper powerlaw with an index of $\Gamma = 2.19^{+0.03}_{-0.02}$ and 2MASX J138+0927 with $\Gamma = 1.4^{+0.4}_{-0.2}$.

Important observable of the sources are their luminosity and flux. Since the flux of a source scales with $1/r^2$, where r is the distance to the source, and the flux is affected by heavy absorption, one expects the majority of the sources exhibit low fluxes. This can be

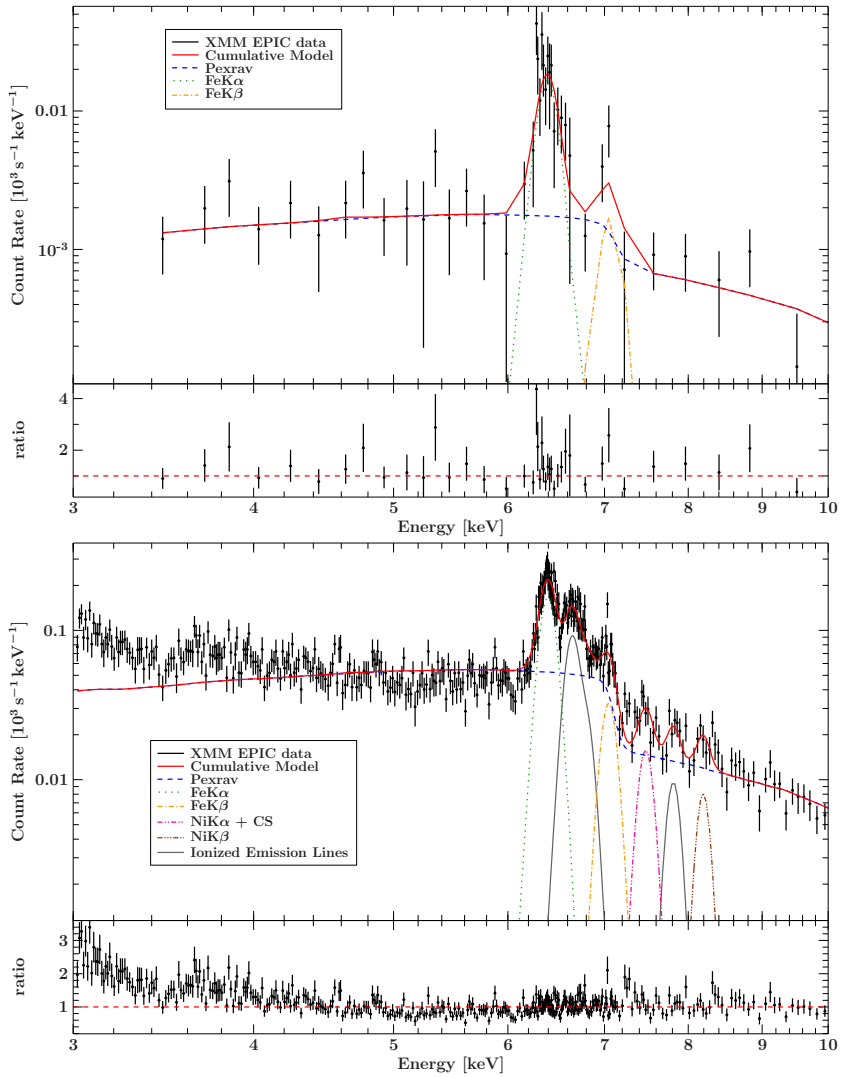

Figure 7.5.: Best-fit spectrum and model components for NGC 1386 (upper panel) and NGC 1068 (lower panel).

observed in the distribution of the observed flux in Fig. 7.10. About 46% of the sources exhibit a flux of less than $10^{-12}\,\mathrm{erg\,cm^{-2}\,s^{-1}}$. Only the Circinus Galaxy has a flux of the order of $10^{-11}\,\mathrm{erg\,cm^{-2}\,s^{-1}}$. It is also the closest Compton-thick AGN in the sample (z=0.001448, luminosity distance $d_\mathrm{L} = 8\,\mathrm{Mpc}$), thus it is expected to have a high flux, even though it is heavily absorbed with $N_\mathrm{H} \geq 10^{24}\ \mathrm{cm^{-2}}$. The lowest flux is observed in 2MASX J1150+5249, which is located at a distance of z=0.0355 ($d_\mathrm{L} = 153\,\mathrm{Mpc}$). Its spectrum is also reflection-dominated indicating $N_\mathrm{H} \geq 10^{24}\,\mathrm{cm^{-2}}$. For a similar luminosity, the expected flux of 2MASX J1150+5249 is only 0.2% of the flux of Circinus Galaxy, because of the greater distance. The observed flux ratio is 0.005, which suggests that under the assumption of comparable luminosities, both AGN have similar column

densities. The flux diagram translates directly into a luminosity diagram through the relation

$$F = \frac{L}{4\pi\, d_{\mathrm{L}}}, \tag{7.3.1}$$

where F is the flux, L the luminosity and d_{L} the luminosity distance, which depends on the redshift z through $d_{\mathrm{L}} = (1+z)d_{\mathrm{M}}$). Here the distance module $d_{\mathrm{M}}(H_0, \Lambda_0, \Omega_M$ includes the underlying cosmology. The default values used in `Xspec` are: $H_0 = 70$, $\Omega_M = 0.27$, $\Lambda_0 = 0.73$ (Bennett et al. 2003). The results for the luminosity are shown in table Tab. 7.3. Fig. 7.11 shows the distribution of the observed luminosity. Absorption corrected values could be calculated only for sources where the absorbed powerlaw could be detected and the column density was measured.

Test for the X-ray Baldwin effect

The original Baldwin effect was discovered by Baldwin (1977), who found a strong anti-correlation between the continuum luminosities and the equivalent width of broad emission lines (especially C IV λ1550) in the UV band of Quasars. It was later confirmed for narrow emission lines as well. The origin of this effect remains unexplained, though many authors associate it with the effect of a changing continuum shape and a softer ionized continuum for high luminosities (e.g. Netzer et al. 1992, Zhang et al. 2013). Iwasawa & Taniguchi (1993) studied X-ray data of 37 radio-loud and quiet type I AGN from the *Ginga* satellite and discovered an anti-correlation of the equivalent width of the X-ray Fe Kα line against the X-ray 2-10 keV continuum, EW64 $\propto L_{2-10\,\mathrm{keV}}^{-0.20\pm0.03}$, similar to the one of the original Baldwin effect. This anti-correlation is thus also known as 'X-ray Baldwin effect' or 'Iwasawa-Taniguchi effect'. It was reported for narrow Fe Kα lines as well, with a relation EW64 $\propto L_{2-10\,\mathrm{keV}}^{-0.17\pm0.08}$ and a Spearman rank probability of $\geq 99.9\%$ (Page et al. 2004). So far, the X-ray Baldwin effect has not been reported for Seyfert II galaxies yet.

In order to test for the X-ray Baldwin effect (XBE) in this sample, only sources for which an absorbed powerlaw was found could be used. Since the XBE was only reported for type I AGN, the equivalent width of the Fe Kα line was determined for the unabsorbed powerlaw continuum (EW64-I), assuming that the different equivalent width in type I and type II Seyfert galaxies is caused by a higher column density in type II AGN. The resulting EW64-I, as well as the corresponding unabsorbed continuum flux and luminosity are reported in Tab. 7.7, while EW64-I is plotted against $L_{2-10\,\mathrm{keV}}$ in Fig. 7.12. This shows negative a trend of EW64-I with increasing luminosity. The Spearman's correlation coefficient of the best-fit values of log EW64-I and log $L_{2-10\,\mathrm{keV}}$ is $\rho = -0.57$ at a significance level of 14%, which supports a weak correlation between these observables. A linear fit of $\log_{10}$ EW64 $-$ I $= a + \gamma \log_{10} L_{2-10\,\mathrm{keV}}$ yields $\alpha = -0.25 \pm 1.35$ and $\beta = 2.41^{+0.58}_{-2.41}$.

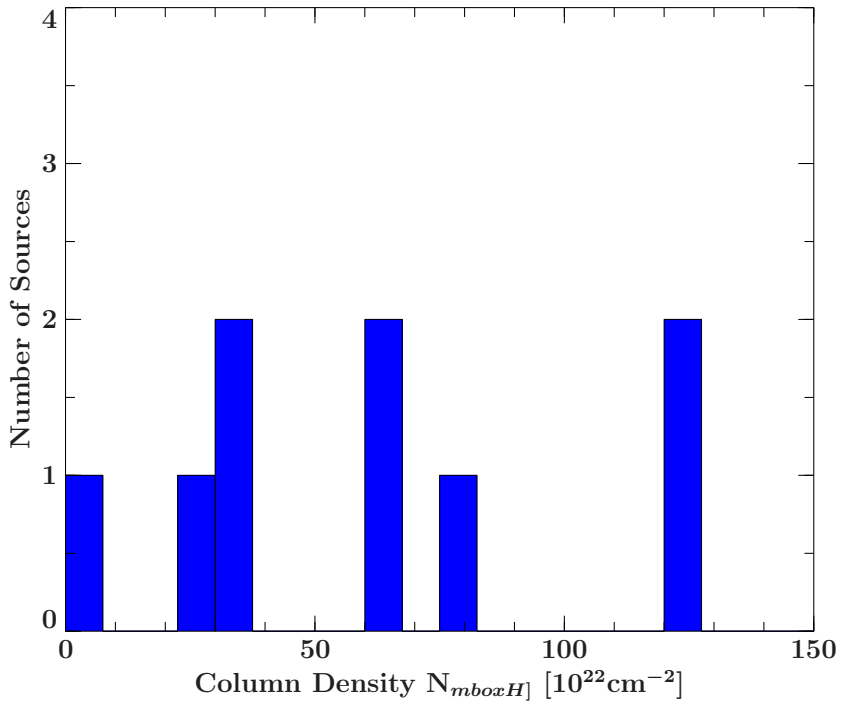

Figure 7.6.: Distribution of the best-fit values of the column density from the mixed model B, which includes an absorbed powerlaw.

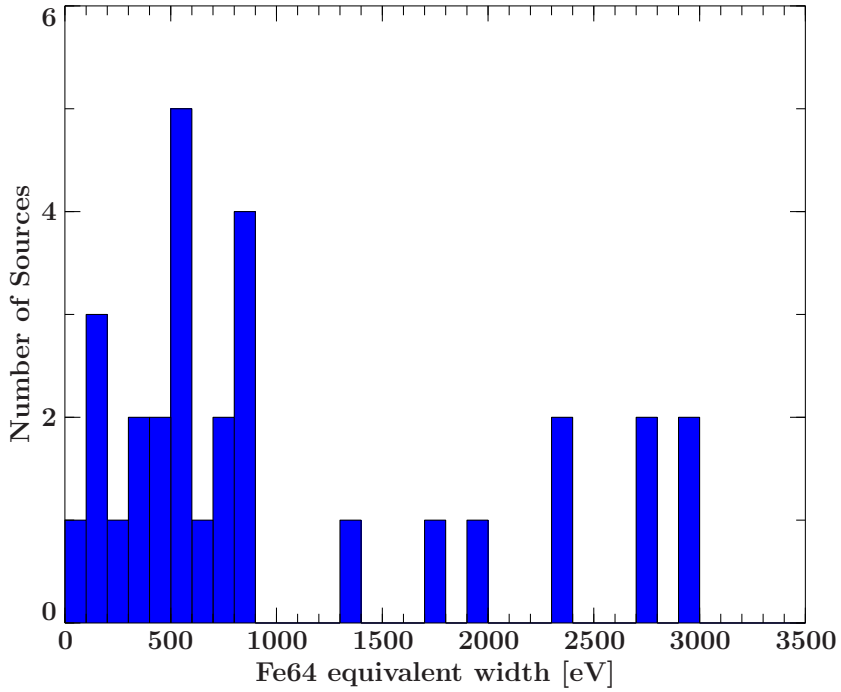

Figure 7.7.: Distribution of the best-fit values of the equivalent width of the 6.4 keV Fe Kα line.

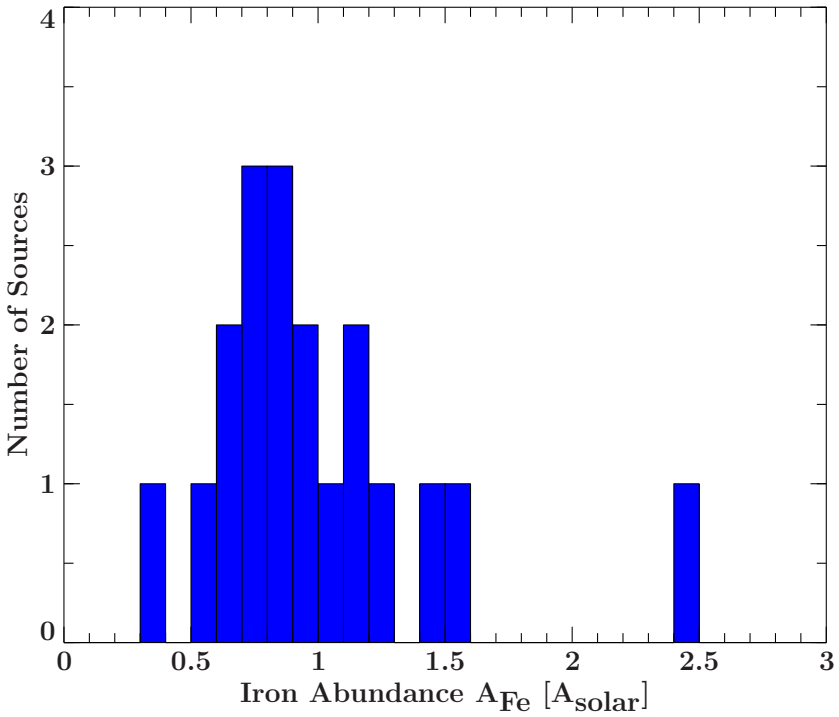

Figure 7.8.: Distribution of the best-fit values of the iron abundance. Fixed values are not included.

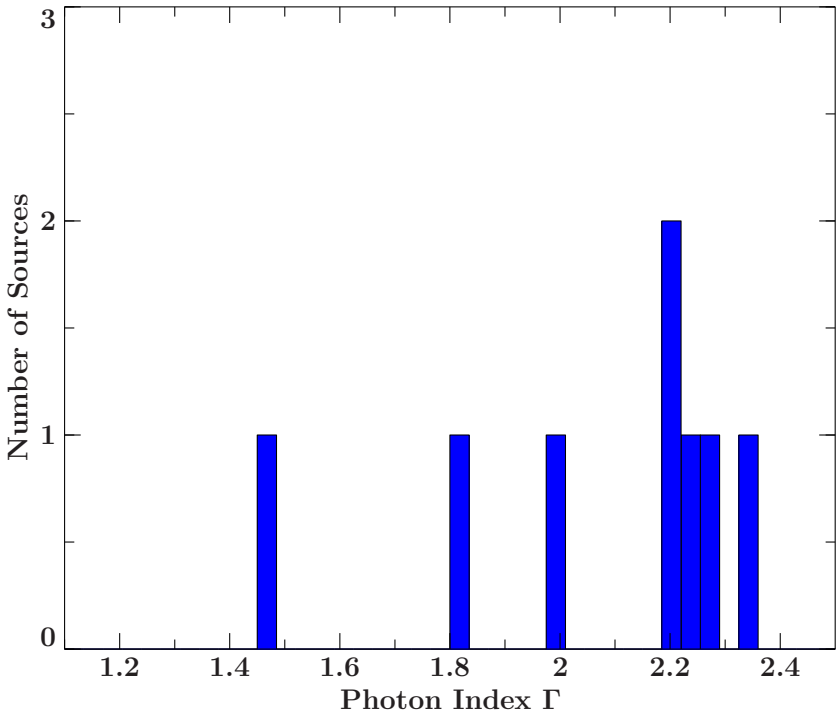

Figure 7.9.: Distribution of the best-fit values of the measured photon index Γ.

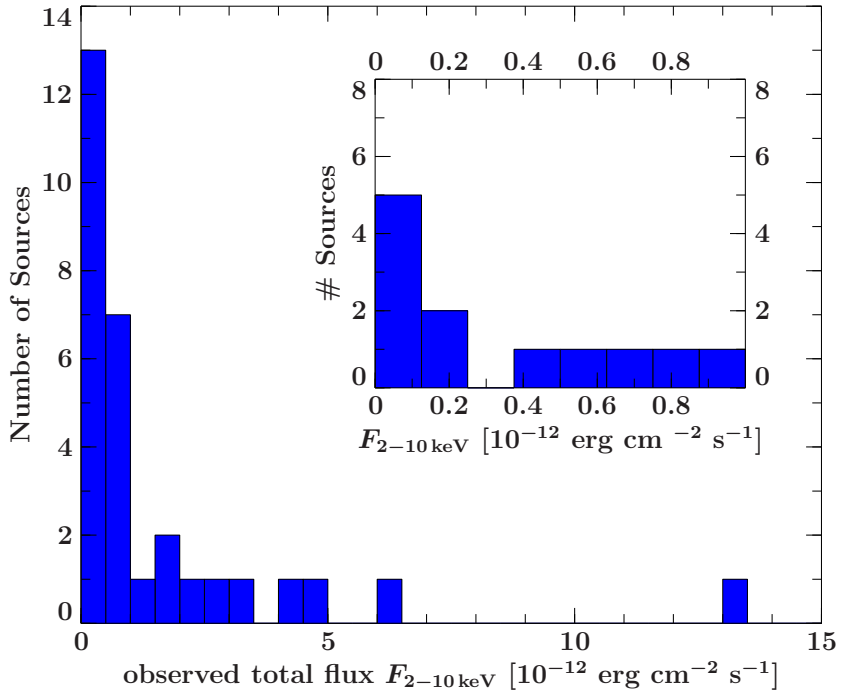

Figure 7.10.: Distribution of the best-fit values of the observed total flux in the 2-10 keV range.

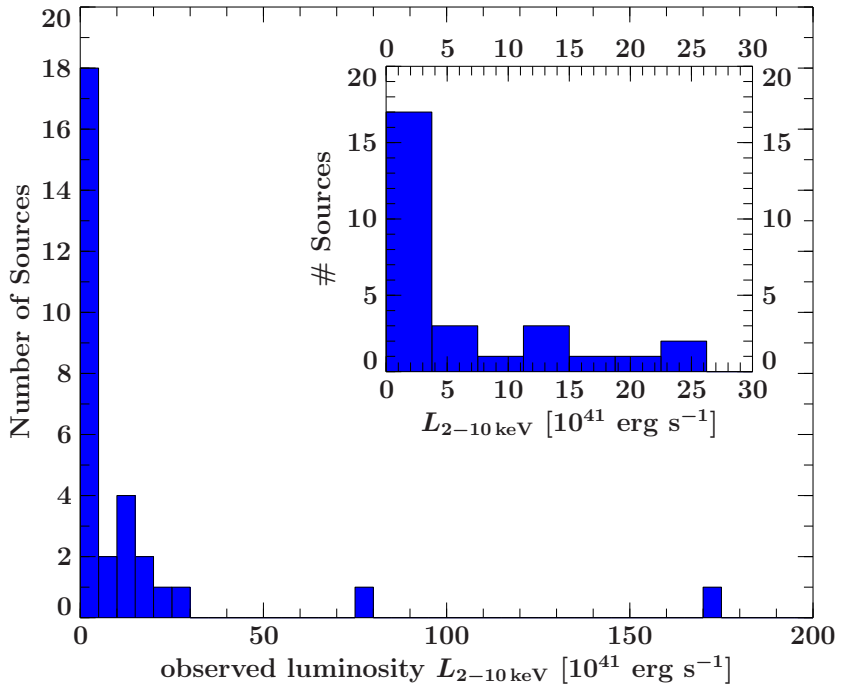

Figure 7.11.: Distribution of the best-fit values of the observed total luminosity in the 2-10 keV range.

Table 7.2.: Best-fit continuum parameters

Name	Γ	A_{Fe}	N_H	Chisq/dof	C/dof
Circinus	1.56^a	$1.22^{+0.09}_{-0.08}$	-	884/827	-
ESO 138-G1	1.80^a	$1.09^{+0.27}_{-0.22}$	-	143/130	-
Mrk 3 (2000-10-19)	$2.19^{+0.03}_{-0.02}$	$0.70^{+0.03}_{-0.05}$	$123.38^{+3.57}_{-9.48}$	798.2/832	-
Mrk 3 2^b (2001-2002)	$2.19^{+0.03}_{-0.02}$	$0.70^{+0.03}_{-0.05}$	$123.38^{+3.57}_{-9.48}$	798.2/832	-
NGC 1068	2.04^a	$2.43^{+0.32}_{-0.30}$	-	712.2/589	-
NGC 424	2^a	$0.93^{+0.39}_{-0.33}$	$76^{+40.10}_{-30.0}$	242/226	-
NGC 4945 (2001-01-21)	1.60^a	$0.73^{+0.16}_{-0.14}$	-	325.7/305	-
NGC 4945^b (2004-01-11)	1.60^a	$0.73^{+0.16}_{-0.14}$	-	325.7/305	
2MASX J1238+0927	$1.46^{+0.43}_{-0.20}$	$1.48^{0.78}_{-0.71}$	$34.60^{+14.90}_{-12.90}$	-	230.97/232
2MASXJ1150+5249	1.90^a	1^a	-	-	33.1/24
CGCG 218−007	1.90^a	$0.74^{+0.61}_{-0.53}$	63^{+14}_{-11}	-	88.4/84
ESO 137-G34	$2.22^{+0.23}_{-0.22}$	1^a	-	-	134.5/117
IC 2560*	-	-	-	-	-
IC 4995	1.90^a	≤ 0.62	-	-	58.1/47
IGR J20286+2544	1.90^a	$0.94^{+0.01}_{-0.01}$	$64.80^{+8.20}_{-6.60}$	-	305.2/332
IRAS F08216+3009	$2.33^{+0.16}_{-0.59}$	$1.18^{+2.06}_{-0.91}$	$25.70^{+6.20}_{-10.30}$	-	347.5/361
Mrk 231	1.90^a	$0.84^{+2.78}_{-0.65}$	$3.46^{+5.52}_{-2.10}$	-	226,5/247
Mrk 266	1.90^a	$0.85^{+1.30}_{-0.61}$	-	-	38.4/49
Mrk 573	1.90^a	1^a	-	-	43.2/21
NGC 1320	1.90^a	1^a	-	-	50.5/43
NGC 1386	1.90^a	$1.18^{+3.10}_{-0.88}$	-	-	35.1/33
NGC 2273	1.90^a	$0.38^{+0.70}_{-0.30}$	-	-	112.9/107
NGC 3076	1.90^a	1^a	-	-	78.5/65
NGC 3393	1.90^a	1^a	-	-	29.4/25
NGC 3690*	-	-	-	-	-
NGC 4666	1.90^a	$1.55^{+2.05}_{-0.86}$	-	-	95.2/117
NGC 4968	1.90^a	1^a	-	-	58.0/50
NGC 5194	1.90^a	1^a	-	-	30.1/23
NGC 6240*	-	-	-	-	-
NGC 7212	$1.82^{+0.24}_{-0.25}$	1^a	-	-	95.5/99
NGC 7674	$2.26^{+0.17}_{-0.50}$	$0.55^{+1.56}_{-0.21}$	-	-	83/76
SWIFT J1009.3-4250	$1.98^{+0.27}_{-0.26}$	$0.85^{+0.45}_{-0.36}$	$32.8^{+5.5}_{-5.50}$	-	897.4/935
UGC 5101	1.90^a	1^a	-	-	72.8/49

Notes: ^{a} fixed. ^{b} linked with parameter of the first dataset. ^{c} hydrogen column density of the absorbed continuum. * not analyzed due to time constraints.

Table 7.3.: Continuum fluxes and luminosities

Name	$F^{Total}_{2-10\,keV}$	$F^{Pexrav}_{2-10\,keV}$	$F^{PowLaw}_{2-10\,keV}$	$L^{Total}_{2-10\,keV}$	$L^{Pexrav}_{2-10\,keV}$	$L^{PowLaw}_{2-10\,keV}$
Circinus	13.46	9.26	-	0.62	0.43	-
ESO 138-G1	2.17	1.78	-	3.98	3.25	-
Mrk 3 (2000-10-19)	6.10	3.26	2.29	24.18	13.05	117.17
Mrk 3[c] (2001-2002)	4.78	2.59	1.60	19	10.40	124
NGC 1068	4.29	3.08	-	1.35	0.97	-
NGC 424	0.86	0.49	0.20	2.61	1.49	5.67
NGC 4945 (2001-01-21)	1.62	1.16	-	0.13	0.09	-
NGC 4945 (2004-01-11)	1.74	1.34	-	0.14	0.10	-
2MASX J1238+0927	1.19	0.43	0.71	171.75	63.01	395.17
2MASXJ1150+5249	0.10	0.07	-	2.87	2.12	-
CGCG 218−007	0.94	0.17	0.71	15	2.80	73.80
ESO 137-G34	0.48	0.38	-	0.88	0.70	-
IC 2560*	-	-	-	-	-	-
IC 4995	0.38	0.29	-	2.16	1.61	-
IGR J20286+2544	2.74	0.20	2.35	11.47	0.85	73.75
IRAS F08216+3009	0.96	0.23	0.64	13.60	3.30	36.20
Mrk 231	0.64	0.34	0.29	25.21	12.98	15.45
Mrk 266	0.30	0.29	-	5.14	4.84	-
Mrk 573	0.25	0.22	-	1.65	1.45	-
NGC 1320	0.43	0.25	-	0.74	0.43	-
NGC 1386	0.28	0.17	-	0.05	0.03	-
NGC 2273	0.89	0.64	-	0.05	0.04	-
NGC 3076	0.30	0.26	-	0.09	0.08	-
NGC 3393	0.22	0.14	-	0.77	0.47	-
NGC 3690*	-	-	-	-	-	-
NGC 4666	0.11	0.10	-	0.07	0.06	-
NGC 4968	0.23	0.15	-	0.49	0.32	-
NGC 5194	0.14	0.09	-	0.01	0.01	-
NGC 6240*	-	-	-	-	-	-
NGC 7212	0.71	0.64	-	11	9.85	-
NGC 7674	0.64	0.56	-	11.80	10.40	-
SWIFT J1009.3-4250	3.26	0.67	2.53	79.10	16.0	234.40
UGC 5101	0.17	0.15	-	5.72	5.160	-

Notes: Fluxes are in units of $10^{-12}\,erg\,s^{-1}\,cm^{-2}$, luminosities are in units of $10^{41}\,erg\,s^{-1}$. Total flux and luminosity are observed values, while the `pexrav` and `powerlaw` values are absorption corrected. * not analyzed due to time constraints.

Table 7.4.: Iron K α line

Name	$E_{\mathrm{Fe\,K}\alpha}$	$I_{\mathrm{Fe\,K}\alpha}$	$\sigma_{\mathrm{Fe\,K}\alpha}$	$EW_{\mathrm{Fe\,K}\alpha}$	$EW_{\mathrm{CS,Fe\,K}\alpha}$
Circinus	$6.40^{+0.01}_{-0.01}$	$31.00^{+0.20}_{-1.80}$	23^{+11}_{-15}	1338^{+86}_{-78}	24^{+24}_{-22}
ESO 138-G1	$6.40^{+0.08}_{-0.01}$	$2.46^{+0.03}_{-0.03}$	47^{+20}_{-24}	522^{+61}_{-63}	≤ 28
Mrk 3 1	$6.40^{+0.02}_{-0.01}$	$4.16^{+0.15}_{-0.42}$	≤ 23	349^{+13}_{-41}	≤ 13
Mrk 3 (2001-2002)	$6.42^{+0.01}_{-0.01}$	$4.29^{+0.21}_{-0.51}$	26^{+20}_{-25}	510^{+23}_{-62}	-
NGC 1068	$6.42^{+0.01}_{-0.01}$	$4.77^{+0.22}_{-0.23}$	25^{+17}_{-19}	464^{+23}_{-22}	≤ 13
NGC 424	$6.44^{+0.08}_{-0.02}$	$1.27^{+0.12}_{-0.18}$	60^{+16}_{-223}	857^{+83}_{-120}	≤ 49
NGC 4945 (2001-01-21)	$6.40^{+0.01}_{-0.04}$	$2.87^{+0.31}_{-0.32}$	≤ 32	848^{+90}_{-95}	≤ 40
NGC 4945 (2004-01-11)	$6.41^{+0.01}_{-0.01}$	$2.95^{+0.20}_{-0.20}$	22^{+22}_{-16}	878^{+62}_{-55}	≤ 23
2MASX J1238+0927	$6.40^{+0.06}_{-0.06}$	$0.30^{+0.18}_{-0.16}$	≤ 96.50	120^{+76}_{-65}	≤ 60
2MASX J1150+5249	$6.44^{+0.09}_{-0.05}$	$0.26^{+0.11}_{-0.14}$	≤ 145	1766^{+692}_{-952}	≤ 230
CGCG 218−007	$6.39^{+0.13}_{-0.07}$	$0.41^{+0.40}_{-0.17}$	20^{+0}_{-0}	200^{+195}_{-82}	≤ 204
ESO 137-G34	$6.40^{+0.03}_{-0.03}$	$0.82^{+0.70}_{-0.25}$	≤ 84	847^{+321}_{-254}	≤ 169
IC 4995	$6.39^{+0.05}_{-0.02}$	$0.80^{+0.22}_{-0.32}$	≤ 66	1928^{+749}_{-566}	≤ 156
IGR J20286+2544	$6.48^{+0.05}_{-0.07}$	$0.88^{+0.41}_{-0.35}$	≤ 141	145^{+62}_{-77}	≤ 82
IRAS F08216+3009	$6.40^{+0.01}_{-0.01}$	$0.94^{+0.57}_{-0.46}$	252^{+181}_{-144}	544^{+332}_{-264}	-
Mrk 231	$6.40^{+0.01}_{-0.01}$	$0.16^{+0.15}_{-0.13}$	20^{+0}_{-0}	153^{+144}_{-124}	-
Mrk 266	$6.46^{+0.07}_{-0.07}$	$0.17^{+0.12}_{-0.11}$	≤ 105	318^{+233}_{-197}	-
Mrk 573	$6.42^{+0.05}_{-0.06}$	$0.31^{+0.19}_{-0.16}$	≤ 85	724^{+451}_{-377}	-
NGC 1320	$6.43^{+0.02}_{-0.02}$	$1.31^{+0.27}_{-0.26}$	≤ 56	2965^{+466}_{-683}	≤ 45
NGC 1386	$6.41^{+0.03}_{-0.03}$	$0.74^{+0.21}_{-0.22}$	≤ 84	2316^{+586}_{-726}	≤ 114
NGC 2273	$6.37^{+0.03}_{-0.02}$	$2.47^{+6.89}_{-1.19}$	≤ 66	2391^{+3766}_{-1147}	≤ 79
NGC 3076	$6.43^{+0.08}_{-0.06}$	$0.35^{+0.16}_{-0.18}$	20^{+0}_{-0}	702^{+316}_{-357}	≤ 156
NGC 3393	$6.44^{+0.06}_{-0.04}$	$0.83^{+0.25}_{-0.36}$	≤ 170	2928^{+885}_{-1286}	≤ 188
NGC 4666	$6.40^{+0.04}_{-0.03}$	$0.12^{+0.05}_{-0.01}$	20^{+0}_{-0}	592^{+232}_{-280}	≤ 99
NGC 4968	$6.43^{+0.06}_{-0.04}$	$0.79^{+0.29}_{-0.25}$	91^{+79}_{-71}	2793^{+1016}_{-887}	≤ 590
NGC 5194	$6.46^{+0.03}_{-0.04}$	$0.48^{+0.15}_{-0.13}$	20^{+0}_{-0}	2741^{+839}_{-729}	≤ 204
NGC 7212	$6.42^{+0.05}_{-0.03}$	$0.73^{+0.24}_{-0.29}$	≤ 89	597^{+209}_{-233}	≤ 106
NGC 7674	$6.40^{+0.01}_{-0.04}$	$0.50^{+0.23}_{-0.19}$	≤ 87	492^{+223}_{-190}	≤ 109
SWIFT J1009.3-4250	$6.40^{+0.01}_{-0.01}$	$4.48^{+3.20}_{-3.20}$	20^{+0}_{-0}	68^{+57}_{-49}	≤ 63
UGC 5101	$6.48^{+0.08}_{-0.05}$	$0.16^{+0.08}_{-0.07}$	≤ 170	625^{+338}_{-266}	≤ 77

Notes: Errors correspond to the 90% confidence level of the best-fit parameters. Energies are units of keV, EW in units of eV and intensities I in units of 10^{-5} photons keV^{-1} cm^{-2} s^{-1}.

Table 7.5.: Neutral emission lines

Name	$E_{\mathrm{Fe\,K}\beta}$	$I_{\mathrm{Fe\,K}\beta}$	$EW_{\mathrm{Fe\,K}\beta}$	$E_{\mathrm{Ni\,K}\alpha}$	$I_{\mathrm{Ni\,K}\alpha}$	$EW_{\mathrm{Ni\,K}\alpha}$
Circinus	$7.04^{+0.01}_{-0.01}$	$4.56^{+0.31}_{-0.31}$	$307.00^{+21.00}_{-21.00}$	$7.48^{+0.01}_{-0.02}$	$1.59^{+0.23}_{-0.23}$	$166.00^{+24.00}_{-24.00}$
ESO 138-G1	$7.05^{+0.09}_{-0.08}$	$0.00^{+0.37}_{-0.00}$	$0.00^{+128.00}_{-0.00}$	$7.47^{+0.78}_{-0.06}$	$0.00^{+0.33}_{-0.00}$	$0.00^{+54.00}_{-0.00}$
Mrk 3 (2000-10-19)	$7.04^{+0.04}_{-0.03}$	$0.57^{+0.12}_{-0.20}$	$57.00^{+17.00}_{-21.00}$	-	-	-
Mrk 3 (2001-2002)	$7.06^{+0.02}_{-0.06}$	$0.83^{+0.21}_{-0.31}$	$111.00^{+28.00}_{-41.00}$	-	-	-
NGC 1068	$7.07^{+0.02}_{-0.02}$	$0.02^{+0.14}_{-1.17}$	$183.00^{+22.00}_{-25.00}$	-	-	-
NGC 424	$7.13^{+0.08}_{-0.07}$	$0.20^{+0.08}_{-0.10}$	-	$7.47^{+0.18}_{-0.00}$	-	$0.00^{+174.00}_{-0.00}$
NGC 4945 (2001-01-21)	$6.93^{+0.20}_{-0.14}$	$0.23^{+0.20}_{-0.17}$	$73.00^{+63.00}_{-54.00}$	$7.57^{+0.14}_{-0.12}$	$0.19^{+0.15}_{-0.15}$	$142.00^{+117.00}_{-115.00}$
NGC 4945 (2004-01-11)	$7.00^{+0.03}_{-0.03}$	$0.40^{+0.12}_{-0.12}$	$130.00^{+37.00}_{-36.00}$	$7.38^{+0.13}_{-0.14}$	$0.09^{+0.10}_{-0.05}$	$47.00^{+43.00}_{-25.00}$
2MASX J1238+0927	$6.97^{+0.34}_{-0.12}$	$0.19^{+0.19}_{-0.17}$	$91.00^{+79.00}_{-87.00}$	-	-	-
2MASX J1150+5249	-	-	-	-	-	-
CGCG 218−007	-	-	-	-	-	-
ESO 137-G34	-	-	-	-	-	-
IC 4995	-	-	-	-	-	-
IGR J20286+2544	$7.17^{+0.07}_{-0.09}$	$0.46^{+0.29}_{-0.29}$	$99.00^{+61.00}_{-66.00}$	-	-	-
IRAS F08216+3009	-	-	-	-	-	-
Mrk 231	-	-	-	-	-	-
Mrk 266	-	-	-	-	-	-
Mrk 573	-	-	-	-	-	-
NGC 1320	-	-	-	$7.35^{+0.04}_{-0.10}$	$0.18^{+0.14}_{-0.11}$	$617.00^{+488.00}_{-340.00}$
NGC 1386	$7.08^{+0.08}_{-0.05}$	$0.13^{+0.12}_{-0.11}$	$493.00^{+452.00}_{-434.00}$	-	-	-
NGC 2273	-	-	-	-	-	-
NGC 3076	-	-	-	-	-	-
NGC 3393	-	-	-	-	-	-
NGC 4666	-	-	-	-	-	-
NGC 4968	-	-	-	-	-	-
NGC 5194	-	-	-	-	-	-
NGC 7212	-	-	-	-	-	-
NGC 7674	-	-	-	-	-	-
SWIFT J1009.3-4250	-	-	-	-	-	-
UGC 5101	-	-	-	-	-	-

Notes: Line widths σ were linked with the width of the 6.4 keV iron line. Errors correspond to the 90% confidence level of the best-fit parameters. Energies are in units of keV, EW in units of eV and intensities in units of 10^{-5} photons $\mathrm{keV}^{-1}\,\mathrm{cm}^2$ s.

Table 7.6.: Ionized emission lines

Name	Energy E	Intensity	EW
Circinus	$6,68^{+0,02}_{-0,03}$	$1,7^{+0,35}_{-0,29}$	25^{+5}_{-4}
ESO 138-G1	$6,57^{+0,06}_{-0,06}$	$0,55^{+0,23}_{-0,23}$	69^{+30}_{-29}
IC 4995	$6,78^{+0,09}_{-0,09}$	$0,14^{+0,14}_{-0,11}$	341^{+257}_{-331}
IGR J20286+2544	$6,86^{+0,11}_{-0,17}$	$0,38^{+0,32}_{-0,32}$	57^{+56}_{-47}
Mrk 3 (2000-10-19)	$6,70^{+0,04}_{-0,02}$	$0,67^{+0,17}_{-0,22}$	40^{+10}_{-13}
Mrk 3 (2001-2002)	$6,74^{+0,05}_{-0,06}$	$0,67^{+0,17}_{-0,22}$	40^{+10}_{-13}
NGC 424	$6,69^{+0,12}_{-0,11}$	$0,11^{+0,11}_{-0,07}$	29^{+30}_{-19}
	$6,92^{+0,10}_{-0,33}$	$0,12^{+0,08}_{-0,08}$	66^{+45}_{-44}
NGC 1068	$6,67^{+0,02}_{-0,03}$	$2,41^{+0,18}_{-0,57}$	161^{+12}_{-38}
	$6,84^{+0,31}_{-0,06}$	$0,85^{+0,53}_{-0,22}$	75^{+46}_{-20}
	$7,30^{+0,44}_{-0,08}$	$0,32^{+0,10}_{-0,13}$	54^{+18}_{-22}
	$7,84^{+0,02}_{-0,03}$	$0,52^{+0,10}_{-0,1}$	140^{+28}_{-23}
	$8,22^{+0,05}_{-0,05}$	$0,39^{+0,11}_{-0,11}$	128^{+36}_{-36}
NGC 1320	$6,75^{+0,03}_{-0,05}$	$0,18^{+0,16}_{-0,11}$	444^{+372}_{-275}
NGC 4945 (2001-01-21)	$6,69^{+0,03}_{-0,04}$	$0,88^{+0,22}_{-0,25}$	122^{+31}_{-35}
NGC 4945 (2004-01-11)	$6,67^{+0,03}_{-0,17}$	$0,65^{+0,14}_{-0,12}$	92^{+20}_{-18}

Notes: Line widths σ were fixed to $\sigma = 1\,\mathrm{eV}$. Errors correspond to the 90% confidence level of the best-fit parameters. Energies are units of keV, EW in units of eV and intensities in units of 10^{-5} photons $\mathrm{keV}^{-1}\,\mathrm{cm}^2\,\mathrm{s}$

7.4. Discussion of the hard X-ray spectrum

This chapter treats the discussion of the results conducted in the hard X-ray analysis. It includes the discussion of the iron line properties, and distribution of the observed luminosities as a function of the redshift.

7.4.1. The Fe Kα line complex

Fig. 7.13 shows the line width of the neutral Fe Kα line and their equivalent width, as a function of their center energies. The majority of the lines show a center energy of $E \leq 6.5\,\mathrm{keV}$, which is consistent with iron Kα emission of neutral or low ionized iron. Thus, a significant part of the fluorescence lines appear to be caused by reflection from a neutral or low ionized medium, with ionization stages less than Fe X.
In many cases only upper limits were found for the line width of Fe Kα. For well constrained data, the upper limit of the line width is $\leq 80\,\mathrm{eV}$, which corresponds to

Table 7.7.: Results for the X-ray Baldwin effect test

Name	$\log F_{2-10\,\mathrm{keV}}$	$L_{2-10\,\mathrm{keV}}$	EW64-I
Mrk 3 (2000-10-19)	$-21.8^{+0.1}_{-0.1}$	155^{+10}_{-11}	89^{+92}_{-78}
Mrk 3 (2001-2002)	$-22.0^{+0.1}_{-0.1}$	109^{+09}_{-09}	129^{+135}_{-113}
SWIFT 1009	$-23.2^{+0.2}_{-0.2}$	236^{+59}_{-45}	40^{+69}_{-11}
2MASX J1238	$-24.0^{+0.4}_{-0.5}$	427^{+318}_{-191}	69^{+113}_{-32}
IRAS F08216	$-24.1^{+0.4}_{-0.5}$	44^{+17}_{-21}	114^{+169}_{-63}
Mrk 231	$-24.9^{+0.4}_{-0.6}$	26^{+13}_{-12}	149^{+290}_{-23}
CGCG 218-007	$-24.1^{+1.6}_{-0.4}$	70^{+100}_{-22}	77^{+162}_{-58}
IGR J20286	$-23.5^{+0.3}_{-0.8}$	54^{+13}_{-11}	49^{+73}_{-30}

Note: Errors correspond to the 90% confidence level of the best-fit parameters. EW64-I in units of eV and flux F in units of erg/cm^2/s and Luminosity in units of 10^{41} erg/s.

$\leq 3750\,\mathrm{km/s}$. The mean of the well constrained widths is $23 \pm 13\,\mathrm{eV}$, or $1106 \pm 625\,\mathrm{km/s}$. These small width place the origin of the iron line outside the Broad Line Region, where widths of several 1000 to $10^4\,\mathrm{km/s}$ are common.
The ionized lines which were detected in 9/28 sources (see Tab. 7.6) correspond to Kα emission of He- and H-like iron at 6.7 keV and 6.95 keV, respectively. Ionized iron lines in the assumed scenario are associated with scattering of the primary continuum at the Narrow Line Region. Another possibility is additional reflection off ionized material in the inner regions of the AGN, that was studied e.g. by Życki et al. (1994) or García et al. (2011). García & Kallman (2010) found that for ionization parameters $\xi \leq 200$, the reflected spectrum cannot be distinguished from that of neutral reflection, except for some features in the soft X-rays. For higher ionization parameters, the differences in the soft X-rays become more distinctive as certain emission lines, like O VIII Lα are very strong. For significantly higher parameters, $\xi \geq 1000$, the line features are almost smeared out for the continuum emission is more effective. However, the hard X-ray spectrum is only affected by the presence of highly ionized iron emission lines and the smearing of the iron K absorption edge due to emission of iron in different ionization states. Thus, concentrating on the hard X-ray spectrum alone does not allow to distinguish whether the origin of the ionized emission lines is scattering or reflection.

7.4.2. Dependency of the Fe Kα equivalent width on the column density

The left panel of Fig. 7.14 shows the results for the equivalent width of Fe Kα (EW64) against the column density N_H. EW64 depends on the strength of both the reflected and absorbed continuum. In the diagram a positive trend of EW64 can be seen for an

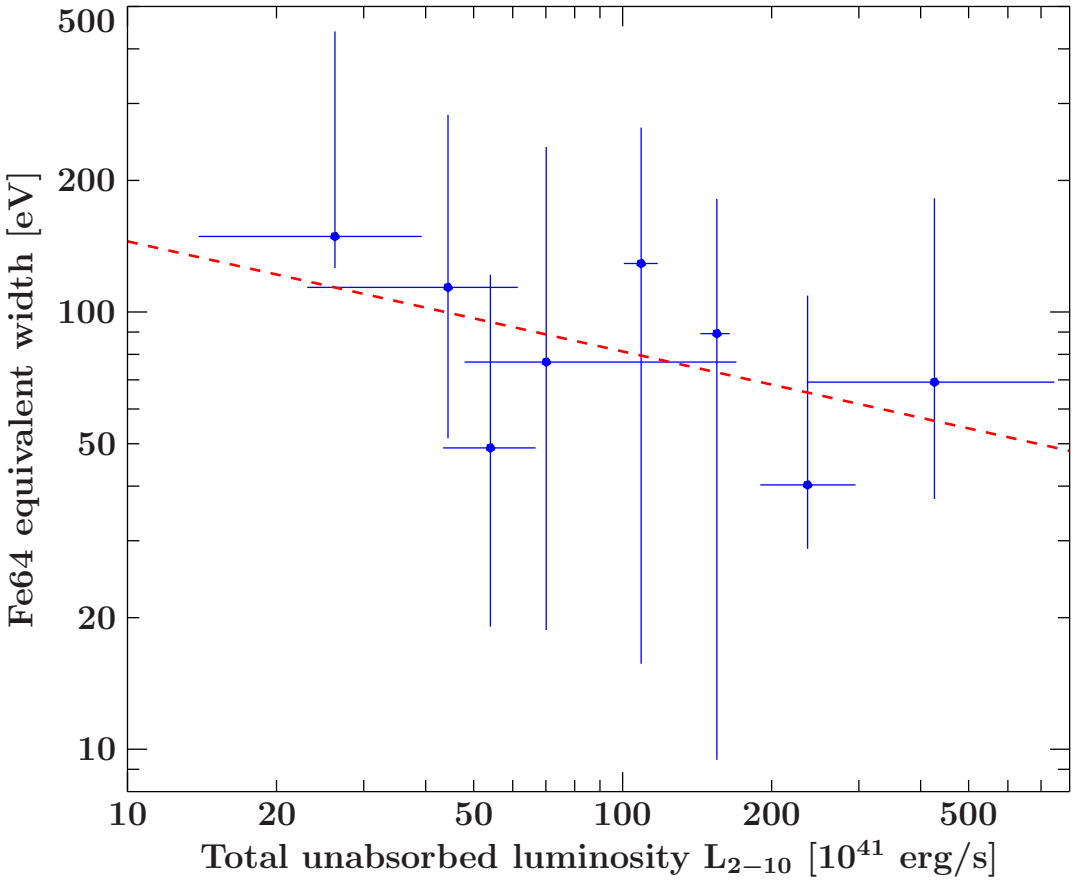

Figure 7.12.: The equivalent width of Fe Kα against the X-ray continuum luminosity for the case of no absorption.The red dashed line corresponds to $\log_{10}$ EW64 $= -0.25 \log_{10} L_{2-10\,\mathrm{keV}} + 2.41$

increasing column density (Spearman rank coefficient $\rho = 0.32$. Exceptions from this trend are NGC 424 and IRAS F0821+3009. Both present a strong iron line with EW64 of 853^{+120}_{-83} eV and 544^{+332}_{-264} eV, respectively.
Since the baseline model component `pexrav` only computes the unabsorbed reflection spectrum off a slab, hence, from the inner walls of the far-side of the torus, it does not take into account the absorbed reflected continuum, which is passing through the near-side of the torus (see Sect. 2.2.4). In the hard X-rays the shape of the absorbed reflection is very similar to the one of the absorbed powerlaw. Thus, if this component is present in the spectrum, this component is modeled as part of the absorbed powerlaw. In this case the results for N_H can be regarded as lower limits to the absorbing column densities of the obscuring matter.
Another important parameter that affects the albedo of a reflecting medium and in effect the strength of the reflected continuum, is the ionization parameter (e.g. Życki et al. 1994) and its iron abundance. A significant incident flux causes complete ionization

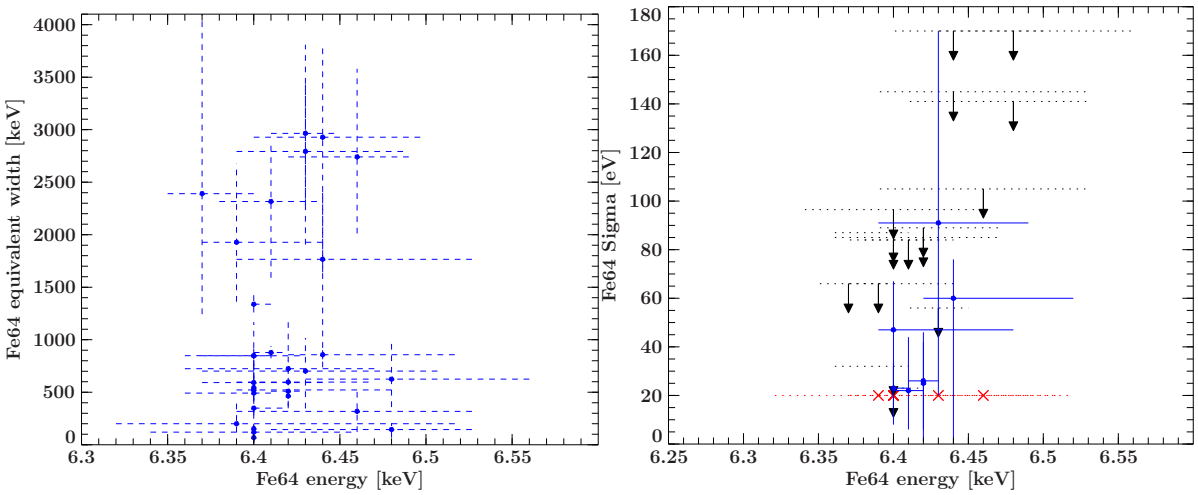

Figure 7.13.: Results for the Fe Kα equivalent width (left panel) and line width σ_{64} (right panel) against the center energy of the Fe Kα line. Red crosses mark lines with fixed line width of 20 eV.

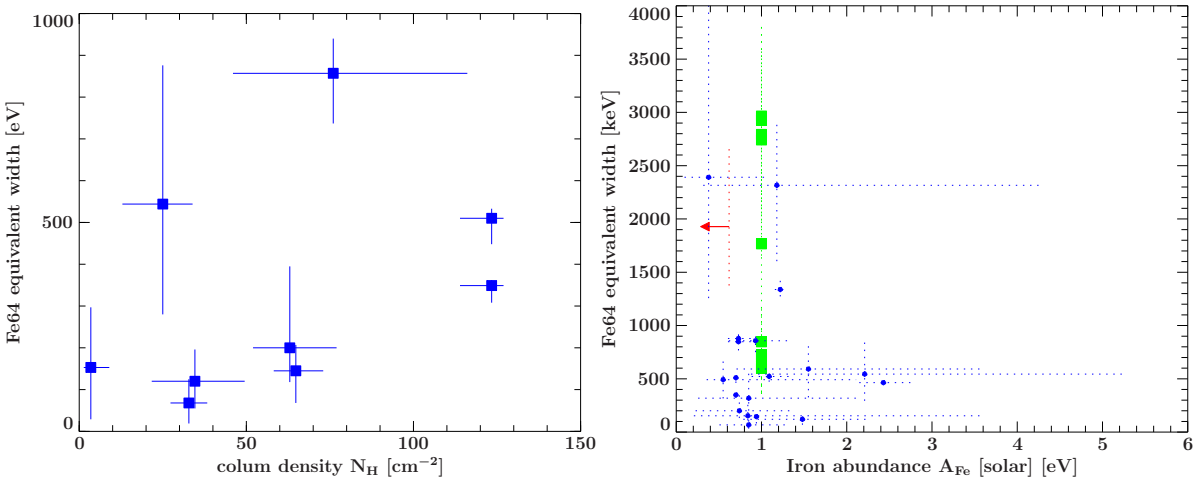

Figure 7.14.: Results for the Fe Kα equivalent width against the column density N_{H} (left panel), for sources where an absorbed powerlaw could be measured and the iron abundance A_{Fe} (right panel). Green squares mark sources for which the iron abundance was fixed to solar abundance.

of heavy elements which reduces the absorption opacities within the reflecting medium and the continuum reflection becomes more effective. With different ionization states the abundances of the (iron) ions change. The Fe Kα lines caused by reflection off a highly ionized gas is mainly due to recombination cascade of He- and H- like iron. The stronger reflected continuum and changing iron abundance yield a weaker EW64. The EW64 of the Fe Kα lines measured in the sample are plotted against the measured iron

abundances in Fig. 7.14. The dependency of EW64 on the ionization parameter (e.g. García et al. 2011) is almost the same for all abundances. For a given iron abundance, the EW64 decreases monotonically with increasing ionization parameter. However, the uncertainties in the results of the fit are to large to make any assumptions on the ionization of the reflector.
Taking this into account, the spread of the EW64-vs-N_{H} diagram depends on the inclination angles, different contributions of the continuum, ionization stages and iron abundaces of the sources. Even though, a positive trend of EW64 against N_{H} is visible. A comparison of the results for NGC 424 and IGR J2028+2544 or CGCG 218−007, which have similar column densities, reveal that the iron abundances are comparable. In terms of luminosities IGR J2028+2544 and CGCG 218−007 show a higher observed luminosity, about one order of magnitude more, while the luminosity of the reflection component is of the same order of 10^{41} erg/s. Given a neutral reflection this suggests that the absorbed powerlaw component in these sources is stronger with respect to the reflection continuum, than in NGC 424. The spectrum of the three sources is shown in Fig. 7.15. In NGC 424 the iron K edge blends with the detected emission lines of He- and H-like iron. It is thus possible that the iron abundance in NGC 424 is affected by the normalization of these lines and it is in fact higher than in IGR J2028+2544 or CGCG 218−007. The shape of their spectra show strong signs for a heavily absorbed powerlaw and a reflection dominated spectrum. This suggests that the strong powerlaw component measured, is a mix of the powerlaw and absorbed reflection component. Under these conditions the iron line is very weak, which can be explained if the source is seen at a high inclination angle, where the strong reflection of the inner wall is not visible and the iron line is caused by the absorbed reflection component. Because of the high scattering of the spectra of IGR J2028+2544 or CGCG 218−007 it cannot be decided whether there is evidence of ionized reflection which could also account for the small EW64, based on the smearing of the iron K edge. At least in IGR J2028+2544 a He-like iron line was detected.
As for IRAS F0821+3009, compared to sources of similar column densities (e.g., 2MASX J1238+0927 and Swift J1009−4250, respectively), present a similar ratio of the reflected and intrinsic continuum ($\sim 6\%$) but has a higher iron abundance, which can account for a higher EW64, since it grows linearly with the iron abundance (García et al. 2011).

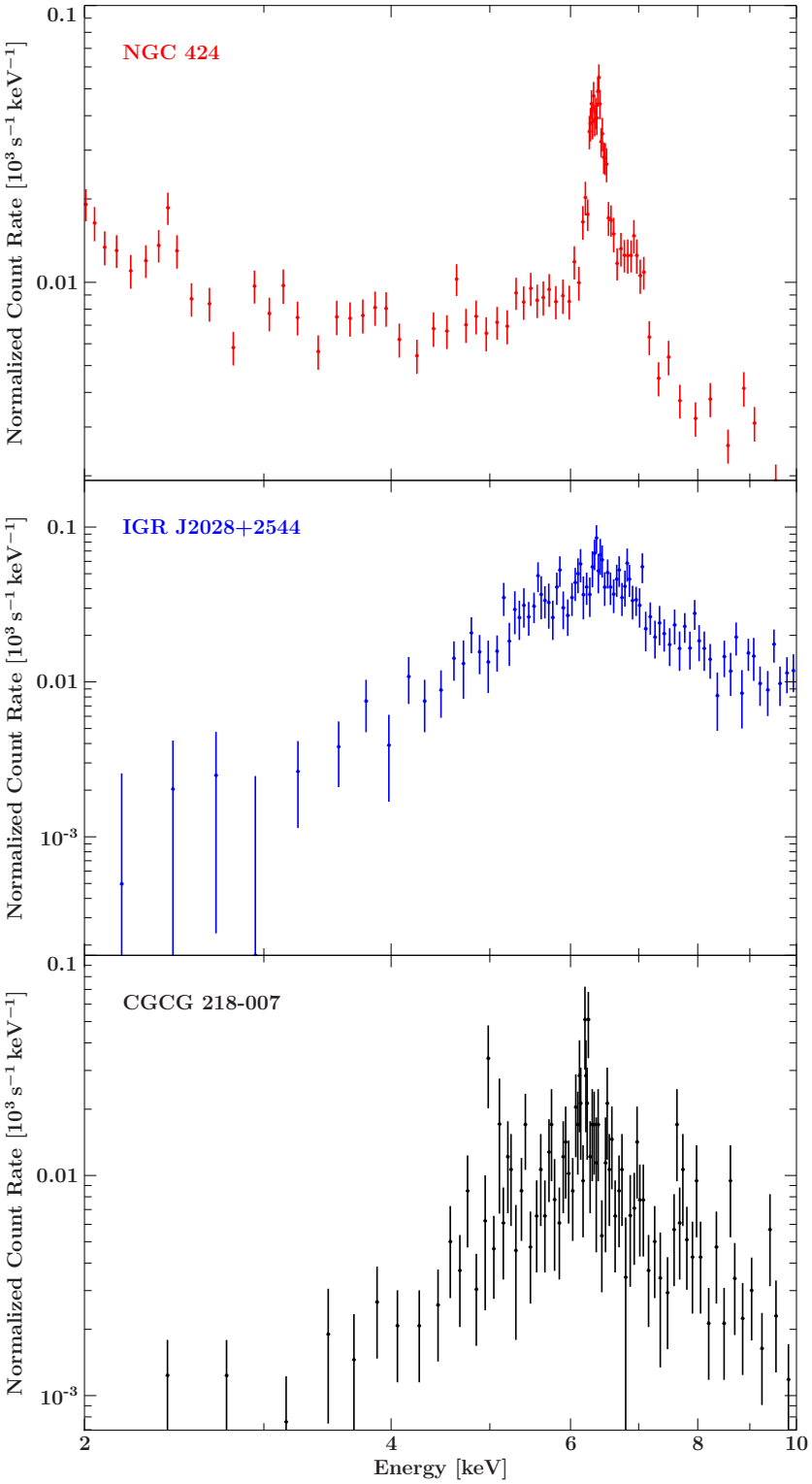

Figure 7.15.: 2-12 keV spectrum of NGC 424, IGR 2028+2544 and CGCG 218−007.

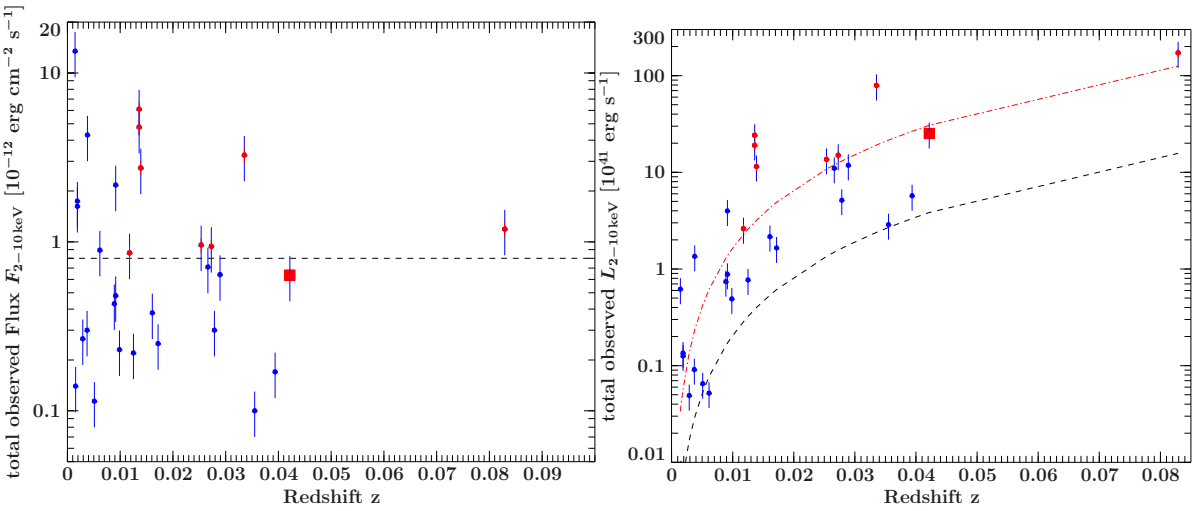

Figure 7.16.: Diagrams of the 2-10 keV total observed flux (left panel) and luminosity (right panel). Sources with best-fits that include an absorbed powerlaw are shown as red circles, while those with a reflection continuum only are depicted in blue circles. The red square marks Mrk231, which was found to be compton-thin. Black dashed line in the flux diagram: marks the flux limit for $z \geq 0.01$ above which a powerlaw was detected. Black dashed line in the luminosity diagram: luminosity limit corresponding to the flux limitation of $0.1 \cdot 10^{-12}\,\mathrm{erg/cm^2/s}$ in the data reduction. Red dotted-dashed line: Luminosity limit corresponding to the powerlaw flux limit above $z = 0.01$. Error bars represent an assumed systematic flux error of 30%.

7.4.3. The distribution of observed luminosities

The total observed flux and corresponding luminosities are plotted against the redshift in Fig. 7.16, (flux diagram and luminosity diagram, hereafter). For `Xspec` does not compute errors on the integrated flux a systematic error of 30% is assumed. The flux diagram shows that sources in the low redshift range are detected at different flux values. The lower limit of spectral counts opposed during the data reduction translates into a flux limitation of $F_{\mathrm{cut}} = 0.1 \cdot 10^{-12}\,\mathrm{erg\,cm^{-2}\,s^{-1}}$. For higher redshifts this flux limit causes a selection effect that becomes more obvious in the luminosity diagram (illustrated as black dashed line). The flux limit corresponds to a minimum luminosity that a source needs in order to be observed with a sufficient Signal-to-Noise ratio. For this, at high redshifts only very luminous sources are detected. On the other hand, very luminous sources are statistically rare at low redshifts. In order to observe them, one has to search large volumes, hence they are predominantly found at high redshifts. In both diagrams sources for which an absorbed powerlaw could be measured in the best-fit are presented as red circles. Also shown is Mrk 231, which was found to be compton-thin. These red-marked sources show a distinct distribution in the diagram. With the KS-test the null hypothesis is rejected at 5% significance level (the p-value for the flux is 0.01). Leaving Mrk 231 aside, one can estimate the flux limit for Compton-thick sources for redshifts $z \geq 0.01$ to be $\sim 0.8 \cdot 10^{-12}\,\mathrm{erg\,cm^{-2}\,s^{-1}}$ from the flux diagram. This

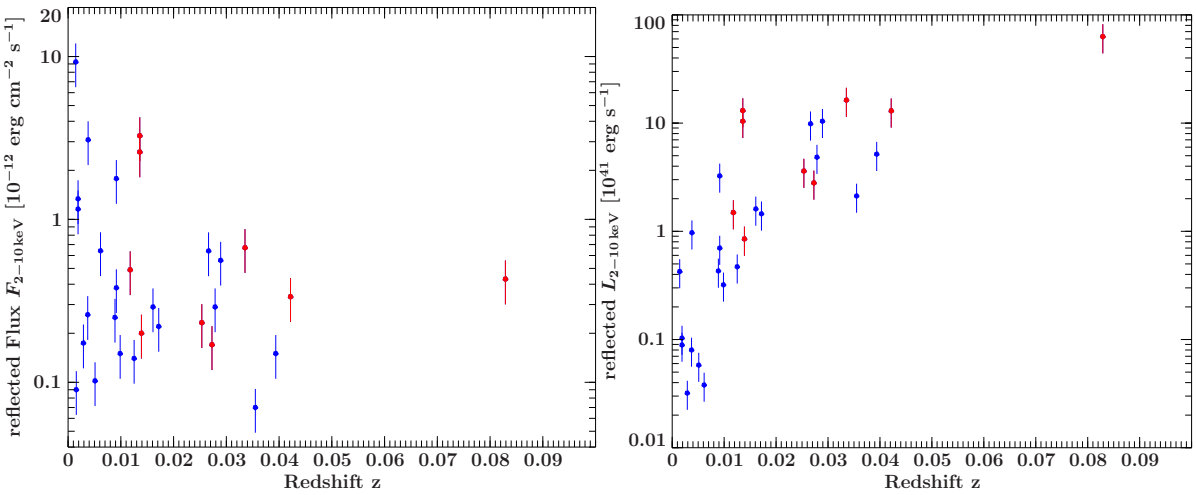

Figure 7.17.: Diagrams of the 2-10 keV flux (left panel) and luminosity (right panel) of the reflected component only. Sources with best-fits that include an absorbed powerlaw are shown as red circles, while those with a reflection continuum only are depicted in blue circles. The red square marks Mrk231, which was found to be compton-thin. Error bars represent an assumed systematic flux error of 30% .

corresponds to the red dot-dashed line in the luminosity diagram. For a given redshift this line represents the luminosity for which an absorbed powerlaw could be fit. Within one redshift bin for $z \geq 0.01$ these sources show a higher total observed luminosity and a smaller column density than heavily absorbed sources. Fig. 7.17 shows the same flux and luminosity diagrams of the reflected continuum only. Compared to the one of the total observed flux and luminosity, no independent distribution is visible (the p-value for the flux diagram is $p = 0.60$). This suggests suggests, that the different distributions in the total flux diagram are caused by the additional powerlaw component, while the reflected component shows no independent distribution.

An interesting feature is that below $z = 0.01$, there is no source for which an absorbed powerlaw was detected. Assuming that a powerlaw component can be detected if the luminosity exceeds a certain limit (red dashed line), one would expect those sources to have an absorbed powerlaw component that is measurable through model fitting. There are sources which have a sufficiently high luminosity but no powerlaw continuum, those are ESO 138-G1, ESO 137-G4, NGC 1068 and NGC 4945. A possible explanation may come again from the fact that the absorbed reflected component is not specifically included in the model, thus the absorbed powerlaw in the fit is biased by the contribution of the absorbed reflection. This means that red-colored sources show an additional component with an unknown contribution of the reflection component, that is not necessary present in the blue colored sources.

In conclusion the strength of the absorbed primary continuum can be regarded as an upper limit, while the red line for luminosity needed to detect it represents a lower limit. Thus the distinction in the redshift space may not be real, since the actual limit

may not include these blue sources. In order to determine the fraction of red sources with redshift lower than 0.01, more sources need to be considered. From the 2–10 keV luminosity function derived by Ueda et al. (2003), it follows that the expected number of AGN below z=0.01, in the luminosity range $\log Lx = 41.5 - 43$, is of the order of 10^4. They estimate the fraction of Compton-thick AGN in this luminosity range to be only a few percent. Thus, the expected number of Compton-thick AGN is of the order of 100 sources. But the sample only comprises 38 sources in total, which shows its incompleteness. In order to determine the column density of an absorbed source it is necessary to observe very luminous sources, which are rare for low redshifts. Hence, the fact that none of the rare and luminous sources with an absorbed powerlaw was detected below z=0.01, is also biased of the incompleteness of the sample.

7.4.4. The X-ray Baldwin Effect

The results for the X-ray Baldwin effect of the HX-subsample support a weak anti-correlation at 14% significance level, which can also be seen also in Fig. 7.12. A simple fit to the data is inconclusive and both consistent with an anti- or no correlation, because of the huge uncertainties of the fit parameters α and β, as well as the uncertainties of EW64-I. However, the best-fit value $\beta = -0.25$ is similar to what was found for the X-ray Baldwin effect of type-I AGN. For better constraints on the possible correlation the uncertainties of EW64-I have to be reduced. On the one hand, for this better quality data is needed, though on the other hand a detailed study of the equivalent width is necessary. In the extimation of the errors of EW64-I it was assumed that its uncertainties depend only on the uncertainties of the strength of the continuum. However, systematically the latter is correlated with the photon index.

8. Analysis of the broad band spectrum

Following the analysis of the hard X-ray spectrum in Chapt. 7, this chapter concentrates on the total *XMM*-Newton 0.3-10 keV spectrum. This includes the soft X-ray range of 0.3-2 keV, which is known to show a complicated composition. The commonly accepted theory for compton-thick AGN is that this component is caused by the scattering of the primary continuum in ionized clouds attributed to the Narrow Line Region (NLR), and exhibits a forest of emission lines due to recombination, radiative decay after photo-excitation and fluorescence after photo-ionization (e.g. Guainazzi & Bianchi 2007). It is commonly fit with a powerlaw absorbed only by a galactic absorber, to model the continuum emission and an number of emission lines with Gaussian profile to account for the emission lines; or an photoionization model derived from the RGS spectrum.
The existence of ionized iron lines in the hard X-ray range may be attributed to the following two scenarios: scattering of the primary continuum in optically-thin, ionized plasma in the line of sight, or ionized reflection off ionized matter, for example the surface of the inner walls of the torus.

In order to fit emission lines in the soft X-rays, spectra with a high SNR are necessary. This analysis provides a case-study of high-SNR observations of four sources, Circinus galaxy, Mrk 3, NGC 424 and NGC 1068, in order to find properties of the 2-10 keV spectrum and to test two origins for the soft X-ray emission: the scattering scenario and the ionized reflection scenario.

This analysis is performed with `ISIS v1.6.2-4` (Houck & Denicola 2000), which uses `Xspec` models.

8.1. The phenomenological view

To get an idea of the composition of the total spectrum, the four sources were systematically fit with a phenomenological model. The assumed scenario is the same as in the analysis of the hard X-ray range. An additional absorbed reflection component is not included, because its shape is similar to the one of the absorbed primary powerlaw and is thus included in the absorbed powerlaw component (see Fig. 2.9).

The phenomenological model

The spectra were fit in the following way: the continuum includes the reflection component `pexrav` and if significant, an absorbed powerlaw, both in the same parameter configuration as explained in Sect. 7.2. Furthermore, an unabsorbed powerlaw was assumed for the continuum of the soft X-rays. In addition Compton-scattering of photons out of the l.o.s. within the torus is considered by the multiplicative model `cabs`. Two parameter configurations were chosen:

a) The powerlaw index of the soft X-ray powerlaw is linked to the one of `pexrav` ($\Gamma_{\mathrm{PL1}} = \Gamma_{\mathrm{Pex}}$), thus it results from the same primary continuum,

b) the indices of the soft and hard X-ray ranges are independent ($\Gamma_{\mathrm{PL1}} \neq \Gamma_{\mathrm{Pex}}$).

Subsequently an emission line is included for Fe Kα (6.4 keV), Fe Kβ (7.05 keV), Ni Kα (7.47 keV), Fe XXV Kα (6.7 keV), Fe XXVI Kα (6.96 keV). Also, subsequently a Gaussian emission line with fixed energy and a fixed width of 1 eV was added in the soft X-ray range. In all cases it was tested if the line minimized χ^2. A list of considered emission lines and corresponding energies is available at Tab. A.1. A global absorber was added in order to account for the galactic H I photo-electric absorption, using the model `phabs`. The lower limit of the absorbing column density was set to the galactic value for each individual source, taken from Kalberla et al. 2005. The final two models consists of:

Model 1 - Reflection dominated:

$C = \mathtt{phabs}(N_{\mathrm{H,gal}})(\mathtt{powerlaw1}(\Gamma, N) + \sum_i G_i(E, N, \sigma) + \mathtt{pexrav}(\Gamma, A_{\mathrm{Fe}}, N)$

Model 2 - Reflection and absorbed continuum:

$C = \text{Model 1} + \mathtt{phabs}(N_{\mathrm{H,gal}})\,[\mathtt{cabs}(N_{\mathrm{H}}) \cdot \mathtt{zvfeabs}(N_{\mathrm{H}}, A_{\mathrm{Fe}}) \cdot \mathtt{powerlaw2}(\Gamma, N)])$

Parameter configuration A: for $\Gamma_{\mathrm{PL1}} = \Gamma_{\mathrm{Pex}}$ B: for $\Gamma_{\mathrm{PL1}} \neq \Gamma_{\mathrm{Pex}}$,

where $\sum_i G_i$ symbolizes the number of Gaussians to fit the emission lines for the soft X-rays and hard X-rays, and the photon index Γ. The iron abundance A_{Fe}, the normalization N, the line energy E and line width σ represent the free model parameters. The results of this fit are presented in Sect. 8.4.

8.2. The scattering scenario

In this part, a self-consistent model for the soft X-ray emission is tested. The soft X-rays are associated to scattering of primary photons of plasma in the line of sight. As described in Sect. 2.2, there are two kinds of plasma in astrophysics: collisional and photo ionized. The later is commonly modeled based on the RGS spectrum Sect. 4.1.3 using photo-ionization codes like XSTAR (Kallman 1999) or Cloudy (Ferland et al. 1998). Self-consistent models for photo-ionized plasma are not yet embedded in Xspec. Studies of

Table 8.1.: Scattering scenario overview: spectral models

Xspec model name	physical description
powerlaw	Primary continuum.
pexrav	Neutral compton-reflection of the intrinsic powerlaw with exponential cut-off.
tbnew/tbnew_simple	Redshifted photo-electric absorption of the primary continuum.
zgauss	Redshift corrected Gaussian line profile.
apec	Emission of collision-driven optically-thin plasma.

the emission of optically-thin collisional plasma were done, for example, by e.g. Raymond & Smith (1977), Mewe et al. (1985), Mewe et al. (1986), or Liedahl et al. (1995), which over time calculated, updated and rewrote models to calculate the spectrum. A frequently used model embedded in `Xspec` is `MEKAL`. Further improvements and additional emission lines in the atomic data are provided in the Astrophysical Plasma Emission Code `APEC`[1] (Smith et al. 2001, Foster et al. 2012) (see Sect. 8.2). Since this analysis concentrates on the EPIC PN Sect. 4.1.2 spectrum, with limited energy resolution, the application of a photo-ionization code is not possible and only the collision-driven scenario is tested.

APEC uses a separate atomic database, Astrophysical Plasma Emission Database (APED), to calculate the line emissivity for more than one million emission lines and continuum emissivity from a hot collisional and optically-thin plasma. The emissivity in `APEC` is defined as the total number of transitions per unit volume and electron as well as hydrogen density. Since the number of emitted photons is proportional to the number of contributing ions, the emissivity requires elemental abundances and ionization balance rates. The level population is calculated for a given plasma temperature from collisional (de)excitation rate coefficients C_{if}, radiative transition rates and recombination transition rate coefficients, derived from the Milne relations Eq. 2.2.16. Model parameters are the plasma temperature T, metal abundance A, redshift z and normalization N.

The scattering model

Assuming the same spectrum component for the hard X-ray Spectrum as describes in Sect. 8.1, the soft X-ray spectrum is modeled as scattered emission from one or multiple optically-thin collision-driven plasma (see Fig. 8.1) in line of sight using `APEC`. For photo-absorption the model `tbnew` is now used, which is an updated version of `tbabs`[2] for absorption of X-rays in the interstellar medium. A simpler version is `tbnew_simple`,

[1] http://atomdb.org/
[2] http://pulsar.sternwarte.uni-erlangen.de/wilms/research/tbabs/

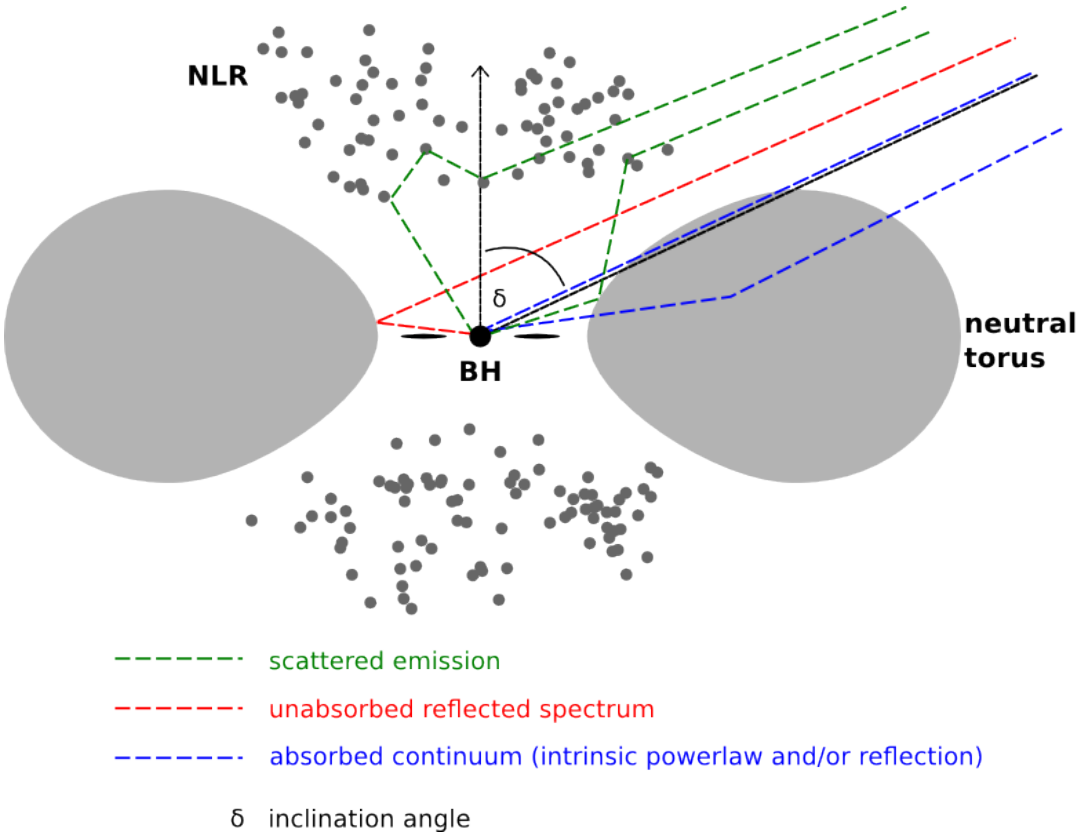

Figure 8.1.: Sketch of the scattering scenario. Blue dotted line: unabsorbed reflection. Yellow dot-dashed line: absorbed primary X-rays. Red solid line: Primary and reflected emission that scatters at ionized clouds of the NLR.Credit: R. Schulz

which has only the hydrogen column density and normalization as model parameter. The final model consists of

Model 1 - reflection dominated:

$$C = \texttt{tbnew\_simple}(N_{\mathrm{H,gal}})(\texttt{APEC}_{\mathrm{n}}(T, A, z, N) + \texttt{pexrav}(\Gamma, A_{\mathrm{Fe}}, N) + \textstyle\sum_i G_i(E, N, \sigma),$$

Model 2 - with absorbed intrinsic continuum:

$$C = \text{Model 1} + \texttt{tbnew\_simple}(N_{\mathrm{H,gal}})(\Gamma, A_{\mathrm{Fe}}, N) + [\texttt{cabs}(N_{\mathrm{H}}) \cdot \texttt{tbnew}(N_{\mathrm{H}}, A_{\mathrm{Fe}}) \cdot \texttt{powerlaw2}(\Gamma, N)]),$$

where $\texttt{APEC}_{\mathrm{n}}(T, A, z, N)$ represents one or multiple components of plasma. Results of the spectral fitting are presented in Sect. 8.4.
The parameter assumption for `pexrav` and the absorbed powerlaw are described in Sect. 7.2. The optically-thin plasma metal abundances were left free to vary and the redshift was fixed to the value of the source, taken from NED. The lower limit of the galactic absorber (`tbnew_simple`) is again fixed to the galactic column density, obtained from Kalberla et al. 2005. For the local absorber of the incident powerlaw (`tbnew`) all

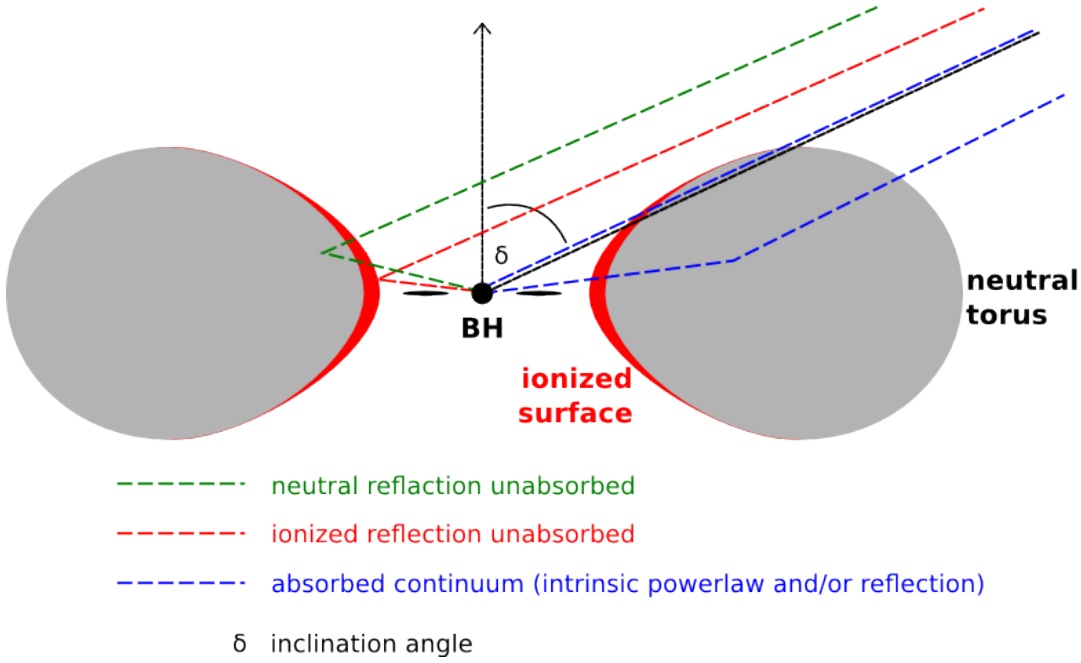

Figure 8.2.: Sketch of the reflection scenario, in which the inner walls of the torus are expected to have an ionized surface. Credit: R. Schulz.

abundances except the iron abundance are assumed to be solar. The iron abundance is linked to the same parameter measured by the compton reflection model `pexrav`. Hence, the free parameters of `tbnew` are reduced to the hydrogen column density and iron abundance.

8.3. The reflection scenario

The complex structure of emission lines in the soft X-ray range may also be attributed to the reflection spectrum itself (see Fig. 8.2). Depending on the ionization state of the reflector, the spectrum exhibits different features. in case of a strong radiation the material becomes ionized. This can occur, for example, by reflection of coronal X-ray at the accretion disk (Matt et al. 1996b) or at the surface of the inner walls of the torus. Studies for ionized reflection have been performed by e.g., Ross et al. 1999 and García et al. 2011. For an ionization parameter $\log \xi \sim 2$ significant changes of the reflected spectrum can be expected for intrinsic X-ray luminosities of the order of $\log L_{\mathrm{X}} \sim 43$, assuming a column density of $\log N_{\mathrm{H}} = 23$ and a reflector at pc-scale. Seyfert galaxies exhibit intrinsic luminosities of the order of 10^{41}–$10^{44}\mathrm{erg\,s^{-1}}$. Ionized reflection may therefore play a role in high luminosity and/or mildly Compton-thick sources. For high ionization parameters emission and absorption lines are weak and the reflected continuum dominates the spectrum. Changing iron abundances for different

Table 8.2.: Reflection scenario overview: spectral models

Xspec model name	physical description
powerlaw	Primary continuum.
pexrav	Neutral compton-reflection of the intrinsic powerlaw with exponential cut-off
xillver	Ionized compton-reflection of the intrinsic powerlaw with exponential cut-off
tbnew/tbnew_simple	Redshifted photo-electric absorption of the primary continuum.
zgauss	Redshift corrected Gaussian line profile.

ions yield different contributions to the prominent iron line (see Sect. 2.2.4).

The reflection model

The model assumes an isotropic X-ray source embedded by an rotationally symmetric torus. The incident radiation is caused by reflection from ionized gas associated with the inner surface of the torus. However, multiple components are considered, as well as neutral reflection off cold or low-ionized material from the inside of the torus. Scattered radiation from the ionized clouds of the NLR is not regarded in this model. Like the previous models, the spectrum includes an absorbed powerlaw continuum if necessary and in case of neutral reflection, Gaussian functions for neutral reflection lines (Fe Kα, Fe Kβ, Ni Kα) are added. The ionized reflection is modeled using the model `xillver` (García & Kallman 2010). The basic model components are:

Model 1 - reflection:

$$C = \texttt{tbnew\_simple}(N_{\mathrm{H,gal}}) \cdot \{\texttt{xillver}_n(\Gamma, N, A_{\mathrm{Fe}}, \xi)\,[+\texttt{pexrav}(\Gamma, A_{\mathrm{Fe}}, N) + \textstyle\sum_i G_i(E, N, \sigma)]\}$$

Model 2 - reflection and absorption:

$$C = \text{Model 1} + \texttt{tbnew\_simple}(N_{\mathrm{H,gal}}) \cdot \texttt{tbnew}(N_{\mathrm{H}}, A_{\mathrm{Fe}}) \cdot \texttt{powerlaw2}(\Gamma, N)$$

where $\texttt{xillver}_n(\Gamma, N, A_{\mathrm{Fe}}, \xi)$ represents one or multiple components of `xillver`.

`xillver` was developed to model the reflection spectrum of an illuminated accretion disk. It assumes a plane-parallel slab with azimuthal symmetry and constant density along the vertical direction of the atmosphere, which is irradiated by an isotropic X-ray source. The spectrum is computed by the calculation of the radiative transfer equation which is followed by the determination of the ionization balance, using `XSTAR` code. Included heating processes are Photo-ionization, Auger effect, Compton heating, charge transfer and de-excitation, which are balanced by radiative and dielectric recombination, bremsstrahlung, collisional ionization and collisional excitation of bound states. To

compute the strength of the emission lines `xillver` takes advantage of state-of-the-art atomic data (Kallman et al. 2004 or García et al. 2005). Free parameters are the photon index of the incident powerlaw, the iron abundance of the slab, the ionization parameter and normalization. The resulting model for different ionization parameters can is depicted in Fig. 8.2.
As in previous models the lower limit of the galactic absorbing column density, which is fixed to the measured value for the particular source (Kalberla et al. 2005). In case of multiple reflections or powerlaw components the photon indices were linked together, thus assuming the same incident powerlaw for all components. The iron abundance was left free to vary separately for all components, to account for different abundances due to different ionization states. In case a `pexrav` component was included, parameter assumptions follow the description of Sect. 8.1.

8.4. Results of the broad-band analysis

Circinus: The phenomenological model with free photon indices of both the hard (Γ_{H}) and soft powerlaw (Γ_{S}) yields a good fit of $\chi^2_{\mathrm{red}} = 1.25$ for 581 d.o.f. ($\chi^2_{\mathrm{red}} = 1.25\,(581)$ hereafter), though it yields an unusual flat spectrum of $\Gamma_{\mathrm{soft}} = 1.03$ and $\Gamma_{\mathrm{H}} = -0.3$. Tying the photon indices together gives an equally good fit of $\chi^2_{\mathrm{red}} = 1.28\,(582)$ with $\Gamma = 1.38^{+0.19}_{-0.16}$, which is consistent within uncertainties with published results of Yang et al. (2009) and the hard X-ray analysis Sect. 7.3. In order to compute systematic parameter correlations contour plots are created for Γ against the normalization of `pexrav` , the normalization of Ni Kα against A_{Fe} and the normalization of Fe Kβ against A_{Fe}, which are shown in Fig. A.1. The contour plot of Γ against the normalization of pexrav, shows a systematic correlation between these parameters, while the iron abundance can be well determined with minor uncertainties caused by the emission lines. The results of the best-fit with tied parameters are listed in Tab. 8.4. The spectrum and model components are shown in Fig. 8.3. The emission lines included in the best-fit are summarized in Tab. 8.8.
Applying the model for the scattering scenario from a thermal plasma, using one `APEC` component with free metal abundance and a free photon index, yields $\chi^2_{\mathrm{red}} = 1.63\,(694)$. But the photon index is very low, ($\Gamma = 1$). Fixing it to the published value of 1.56 results in a worse fit of $\chi^2_{\mathrm{red}} = 3.1\,(617)$. Though the `APEC` component can basically describe the shape of the data, there are strong residuals at 0.86, 1.0, 1.32 and 2.42 keV, indicating further line emission of Fe XVIII, Fe XXI, Mg XI and S XV. A second `APEC` component does not improve the fit. Thus, adding Gaussians emission lines at the energies of the residuals,results in $\chi^2_{\mathrm{red}} = 1.69\,(594)$. The results for the metal abundance of the plasma are consistent with the iron abundance measured by `pexrav` and solar abundance. Best-fit continuum parameters are listed in Tab. 8.5. A plot of the data and best-fit model is shown in Fig. 8.4.
To fit the reflection model a `xillver` component is applied first. The fit is unacceptable

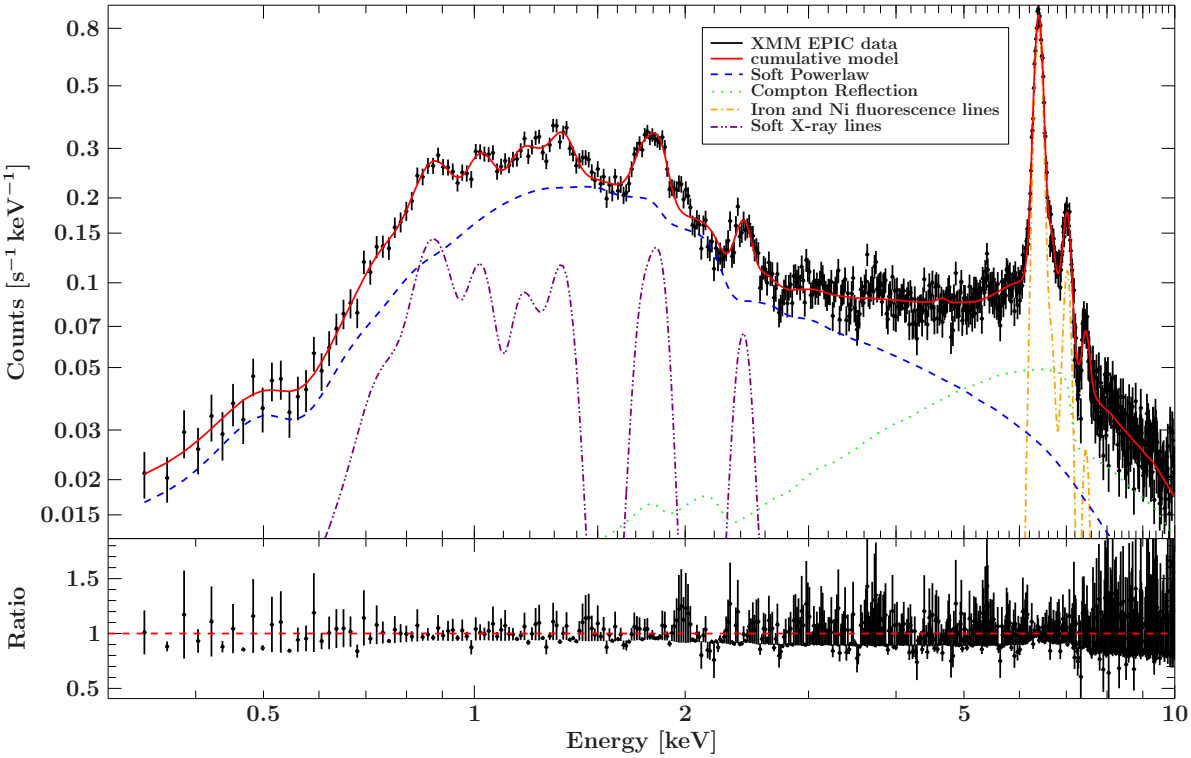

Figure 8.3.: Spectrum of Circinus with the best-fit of the phenomenological model.

with $\chi^2_{\rm red} = 42.3\,(617)$ and significant residuals in the soft X-rays. If a second `xillver` component is added, with linked photon indices, the fit improves to $\chi^2_{\rm red} = 2.85\,(614)$. For the remaining residuals three emission lines at 2.4, 1.0 and 7.47 keV are included, which yield the best-fit of $\chi^2_{\rm red} = 2.27\,(668)$. The line energies are consistent with line emission of S XV, L-emission of Fe XIX to Fe XXII and Ni Kα. The parameters of the first `xillver` component are well constrained. The ionization parameter, $\xi_1 = 100 \pm 1$, indicates a low-ionized reflection component with iron overabundance. The second reflection component on the other hand, is highly ionized, $\log \xi_2 \sim 3$, and shows a lower limit for the iron abundance of $A_{\rm Fe,xi\,2} \geq 9.68$. Best-fit parameters are given in Tab. 8.6, while a plot of the spectrum and best-fit model is also displayed in Fig. 8.4.

Mrk 3: For Mrk 3 the phenomenological model yields consistent values for both independently fit photon indices and the linked parameter configuration. To reduce the number of free parameters the photon index of the soft X-ray powerlaw is tied to the one of `pexrav`. The model yields and excellent fit of $\chi^2_{\rm red} = 1.11\,(546)$. Compared to the hard X-ray analysis the iron abundance is consistent, but the photon index, $\Gamma = 2.05 \pm 0.2$, is slightly flatter and consistent with results of Bianchi et al. (2005). However, the column density is lower. Contour plots are created for Γ against the column density $N_{\rm H}$, the normalization of Ni Kα against $A_{\rm Fe}$ and the normalization of Fe Kβ against $A_{\rm Fe}$, which

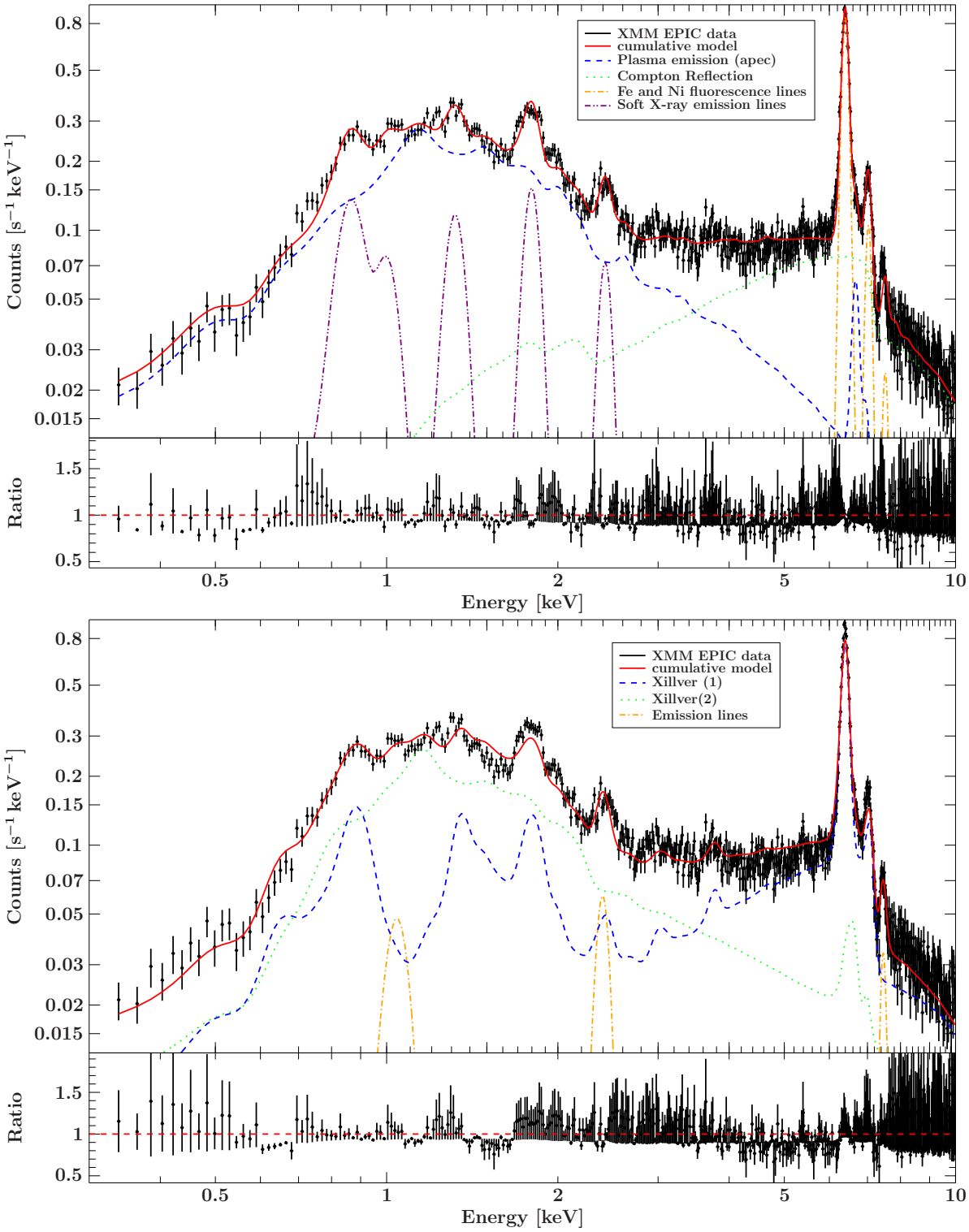

Figure 8.4.: Best-fit of the 0.3–10 keV spectrum of Circinus, for the scattering model (upper panel) and the reflection model (lower panel).

are shown in Fig. A.2. The first shows that the photon index is systematically correlated with the absorbing column density. Taking this into account the results are consistent with those of Bianchi et al. (2005). Best-fit parameters are also given in Tab. 8.4. The included emission lines are given in Tab. 8.8. The spectrum and model components are shown in Fig. 8.5.
When substituting the powerlaw and soft X-ray emission lines with an `APEC` model for solar abundance, there are strong residuals below 1 keV. The fit is $\chi^2_{\mathrm{red}} = 6.62\,(541)$. The residuals removed by the addition of a second `APEC` component and allowing both metal abundances to vary free. At last emission lines were added at 1.72 ± 0.01 keV, $1.27 \pm 0,02$ keV and 2.33 ± 0.03 (interpreted as Mg XI, Mg I and Si I, respectively). The final fit quality is good with $\chi^2_{\mathrm{red}} = 1.15\,(531)$. The corresponding best-fit parameters are listed in Tab. 8.5, while the spectrum is shown in Fig. 8.5.
The results for the photon index and column density are consistent with the ones derived from the hard X-ray analysis. However, the iron abundance is very low, $A_{\mathrm{Fe}} = 0.27 \pm 0.13$. Furthermore, the metal abundances of the two plasma components show only upper limits, which are consistent with solar abundance.
In order to fit the reflection model, the photon index of `xillver` and the absorbed powerlaw are linked. The fit is first performed in the 2-10 keV range, since this is where reflection is dominant. This yields a good fit ($\chi^2_{\mathrm{red}} = 1.13\,(432)$ in the 2–10 keV range). But when evaluated on the 0.3–10 keV range, there is a clear soft excess below 1 keV, compared to the expected emission of `xillver` ($\chi^2_{\mathrm{red}} = 5.76\,(545)$). Adding another reflection component to test for the presence of another reflector minimizes the fit statistic to $\chi^2_{\mathrm{red}} = 1.64\,(542)$. The resulting photon index of the primary powerlaw is very flat: $\Gamma = 1.24 \pm 0.01$. The higher iron abundances can be explained by the contribution of an additional continuum component, compared to the hard X-ray analysis model. In conclusion, the transmitted intrinsic powerlaw seems weaker. As for the reflector, one component is rather low-ionized, while the other one is highly ionized. Both show an iron overabundance. Furthermore, the best-fit includes two emission lines, to account for remaining residuals, possibly OIV–VII and FeXX emission. The best-fit parameters are listed in Tab. 8.6, while a plot of the spectrum and best-fit model is given in Fig. 8.6.
In order to test whether the soft X-rays are better described by a scattered emission component, the highly ionized reflection component is substituted for an `APEC` component. This yields an equally good fit, with $\chi^2_{\mathrm{red}} = 1.31\,(538)$, where the iron abundance of the `xillver` component is slightly lower, $A_{\mathrm{Fe}} = 1.53 \pm 0.12$. The iron abundance of the plasma is constrained to $A \leq 3.22$. The best-fit parameters are listed in Tab. 8.7, with the corresponding best-fit model shown in Fig. 8.6. Both the `xillver` and `APEC` components are tested for intrinsic absorption. however, this had no effect on the fit and the resulting column density was zero.

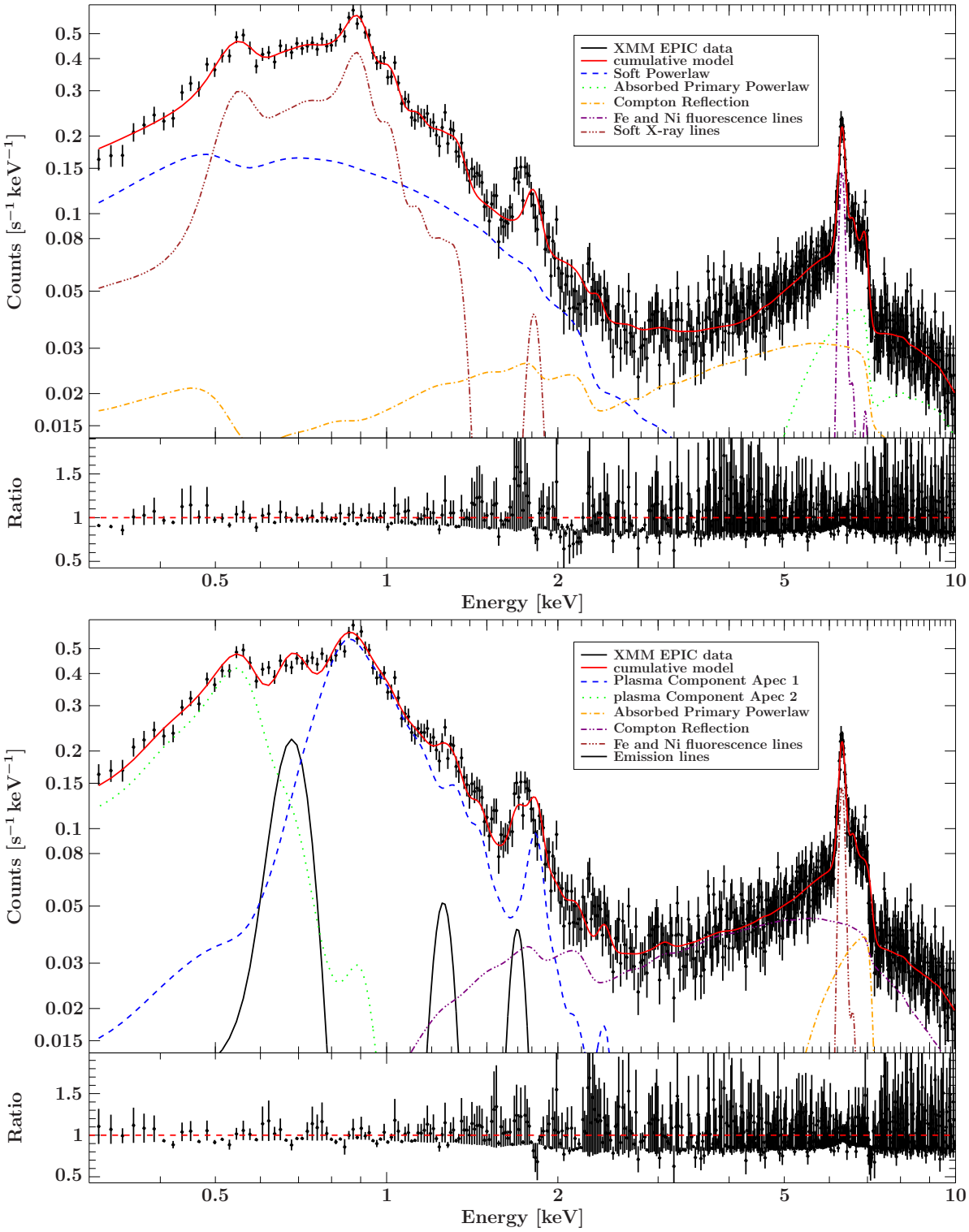

Figure 8.5.: Best-fit of the 0.3–10 keV spectrum of Mrk 3, for the phenomenological model (upper panel) and the scattering model (lower panel).

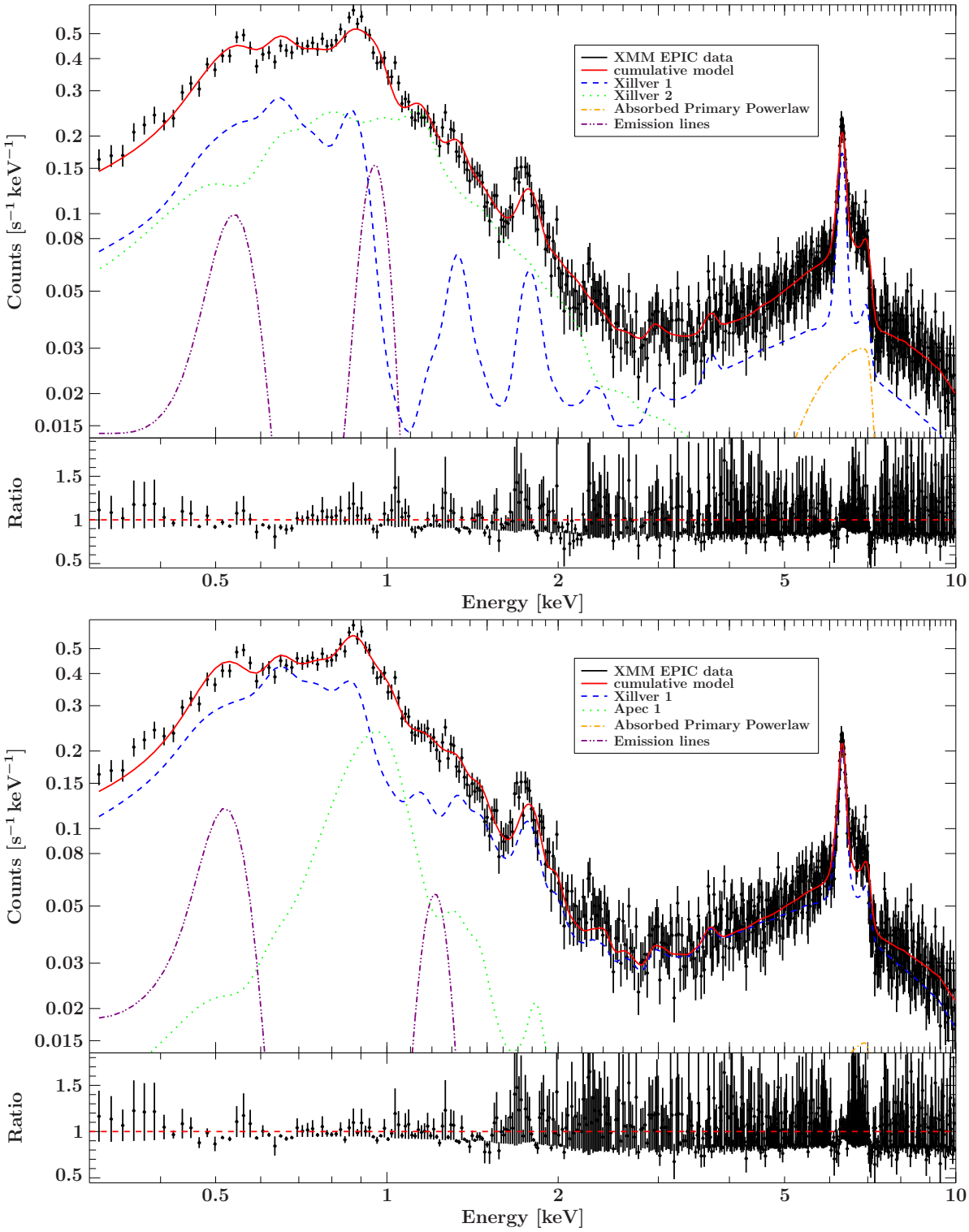

Figure 8.6.: Best-fit of the 0.3–10 keV spectrum of Mrk 3, for the reflection model (upper panel) and the mixed model, with both scattered and reflection components (lower panel).

NGC 1068: The phenomenological model with tied photon indices cannot reproduce the spectrum of NGC 1068, $\chi^2_{\rm red} = 81.3\,(828)$. The model with an independent photon index for the soft X-ray powerlaw, though, gives a good fit of the data, with $\chi^2_{\rm red} = 1.89\,(827)$, while the photon index of `pexrav` is fixed to the published value 2.04. The significantly steeper powerlaw in the soft X-rays indicate that this part cannot be explained solely by Compton-reflection, but additional emission, possibly originating from plasma clouds in the AGN, has to be taken into account. According to Sutherland & Dopita (1993), a hot plasma, both collisional and photoionization driven, can be approximated by a black body. Including such a component in the model and tying the photon indices of the soft and hard powerlaw together, improves the fit further to $\chi^2_{\rm red} = 1.42\,(825)$. The temperature of the black body is $kT = 0.27 \pm 0.02$ keV, suggesting the presence of a low-temperature plasma, in addition to the reflected emission. Contour plots of Γ against the normalization of `pexrav` , the normalization of Ni Kα against $A_{\rm Fe}$ and the normalization of Fe Kβ against $A_{\rm Fe}$ are created and shown in Fig. A.3. The best-fit parameters of the phenomenological model without black body component are listed in Tab. 8.4 and shown in Fig. 8.7. Emission lines detected in the phenomenological fit are summarized in Tab. 8.8.
For the scattering model the hard X-ray range is left unchanged, while the soft X-ray emission lines and powerlaw continuum are now modeled with an `APEC` component for solar abundance. The model is not able to sufficiently describe the data, $\chi^2_{\rm red} = 17.6\,(847)$. Even though the overall shape is reproduced, detailed features of the spectrum below 2 keV are not modeled. This does not improve by allowing the metal abundance of `APEC` to vary as well. The addition of another plasma component minimizes the $\chi^2_{\rm red} = 8.9\,(646)$, which gives a fairly good description of the soft X-ray spectrum. Nevertheless there are strong residual, which are removed by adding emission lines at 1.326 ± 0.003 keV (Mg XI), 1.81 ± 0.01 keV (Si I) and 2.43 ± 0.02 keV (S XV). The final fit is shown in Fig. 8.7, while best-fit parameters are given in Tab. 8.5.
As the hard X-ray analysis showed, the 6–8 keV range of NGC 1068 has many emission lines of neutral and ionized elements. In order to properly fit the reflection model, the energy range is first reduced to 2–10 keV. The forest of emission lines is not sufficiently modeled by one reflection component ($\chi^2_{\rm red} = 34\,(859)$) and even adding a second component ($\chi^2_{\rm red} = 2.07\,(628)$) leaves significant residuals at 6.7 and 7.4 keV. The latter, Ni Kα, is generally not fitted with `xillver`, for no atomic data is included in the tables of `xillver`. Evaluating the model in the 0.3–10 keV range furthermore shows a strong excess of the observed spectrum below 1 keV. In order to take into account neutral reflection, `pexrav` and fluorescence lines (Fe Kα, Fe Kβ and Ni Kα) are included in the model. The fit is acceptable in the 2–10 keV range, with $\chi^2_{\rm red} = 1.44\,(619)$. The ionization parameter of one `xillver` component is of the order of $\log \xi \sim 2$, indicating low-ionized reflection. This suggests a similar emission region like the neutral reflector. The iron abundances of these components are thus linked together, which reduces the statistic insignificantly, $\chi^2_{\rm red} = 1.43\,(620)$. However, evaluating the model on the whole spectrum, the data are poorly described by the reflection model only. Neither a single

blackbody component can account for the residuals, nor a single `APEC` component. A better fit is gained by adding two `APEC` components, which leave smooth residuals below 0.5 keV. These may not be physical, but results from the uncertainties of the detector calibration and the effect of the effective area below 0.5 keV. Fitting these with a simple black body gives the best-fit of $\chi^2_{\rm red} = 2.23\,(839)$. The final model is shown in Fig. 8.8, while best-fit parameters are given in Tab. 8.6 and Tab. 8.7.

NGC 424: The phenomenological model fit presents a similar picture like for NGC 1068. Even though the statistic is acceptable, with linked photon indices, because the photon index of the soft X-ray powerlaw dominates the fit, the resulting photon index is as steep as the hard limit of the `pexrav` model ($\Gamma = 2.5$), while the iron abundance is unreasonably high, $A_{\rm Fe} \leq 51$. On the other hand, fitting both parameters independent results in $\chi^2_{\rm red} = 1.17\,(231)$. The best-fit is shown in Fig. 8.9, corresponding parameters are listed in Tab. 8.4 and contour plots are shown in Fig. A.4. Adding a black body component, while tying the soft and hard photon index, now yields $\chi^2_{\rm red} = 1.06\,(228)$, for a similar plasma temperature as for NGC 1068.
The simple scattering model with one plasma component (`APEC`) for the soft X-rays is insufficient, $\chi^2_{\rm red} = 91\,(240)$, with residuals below 1 keV. An additional plasma component with both metal abundances free to vary improves the fit to $\chi^2_{\rm red} = 2.61\,(244)$. For the best fit of $\chi^2_{\rm red} = 1.26\,(234)$, emission lines for Ne IX, Mg I, Si XIII and S XV were added, to account for the remaining residuals. The best-fit parameters given in Tab. 8.5 and Fig. 8.10 depicts the best-fit model.
For the reflection model, two `xillver` components as well as one neutral reflection component are required to fit the total 0.3–10 keV spectrum, including emission lines at 0.9, 1.3, 1.9 and 2.4 keV. This leads to a final fit of $\chi^2_{\rm red} = 1.48\,(229)$. Additionally it was tested, whether the line emission can be described by one or two `APEC` components. The best-fit is derived for two additional components with $\chi^2_{\rm red} = 1.87\,(236)$, but severe under-abundance for both of the plasma components. The best fit parameters are listed in Tab. 8.6 and Tab. 8.7. The best-fits are shown in Fig. 8.10.

8.5. Discussion of the broad band analysis

This section discusses the results obtained in the spectral analysis in Chapt. 8. Sect. 8.5.1 focusses on the results of the phenomenological model, while the subsequent section (Sect. 8.5.2) compares the results for the scattering and reflection model. In Sect. 8.5.3 the results are put in context with previous studies of these sources.

8.5.1. On the phenomenological model

The phenomenological fit confirms the Compton-thick hard X-ray component and a complex line structure of the soft X-ray in different ionization states. For all sources

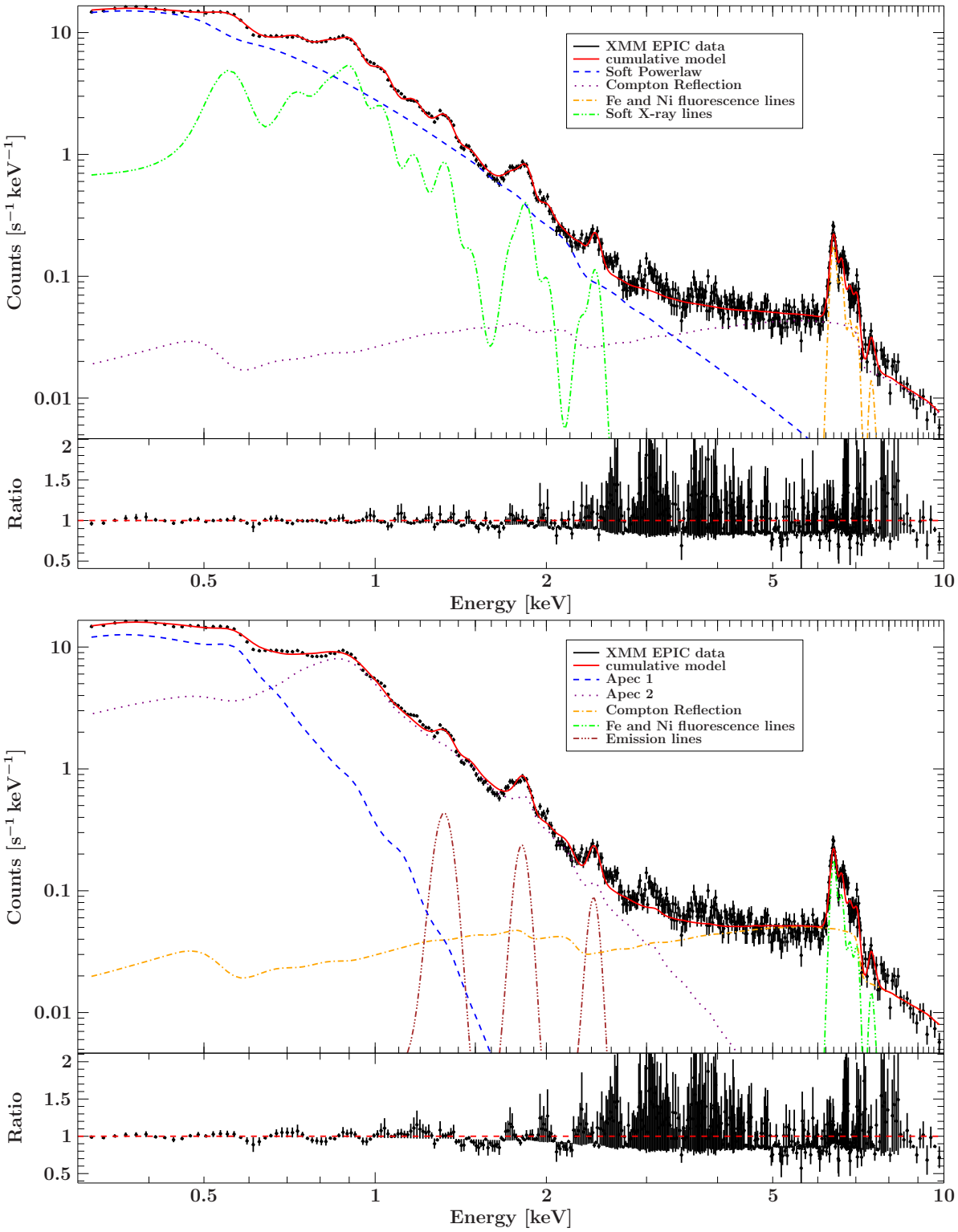

Figure 8.7.: Best-fit of the 0.3–10 keV spectrum of NGC 1068, for the phenomenological model (upper panel) and the scattering model (lower panel).

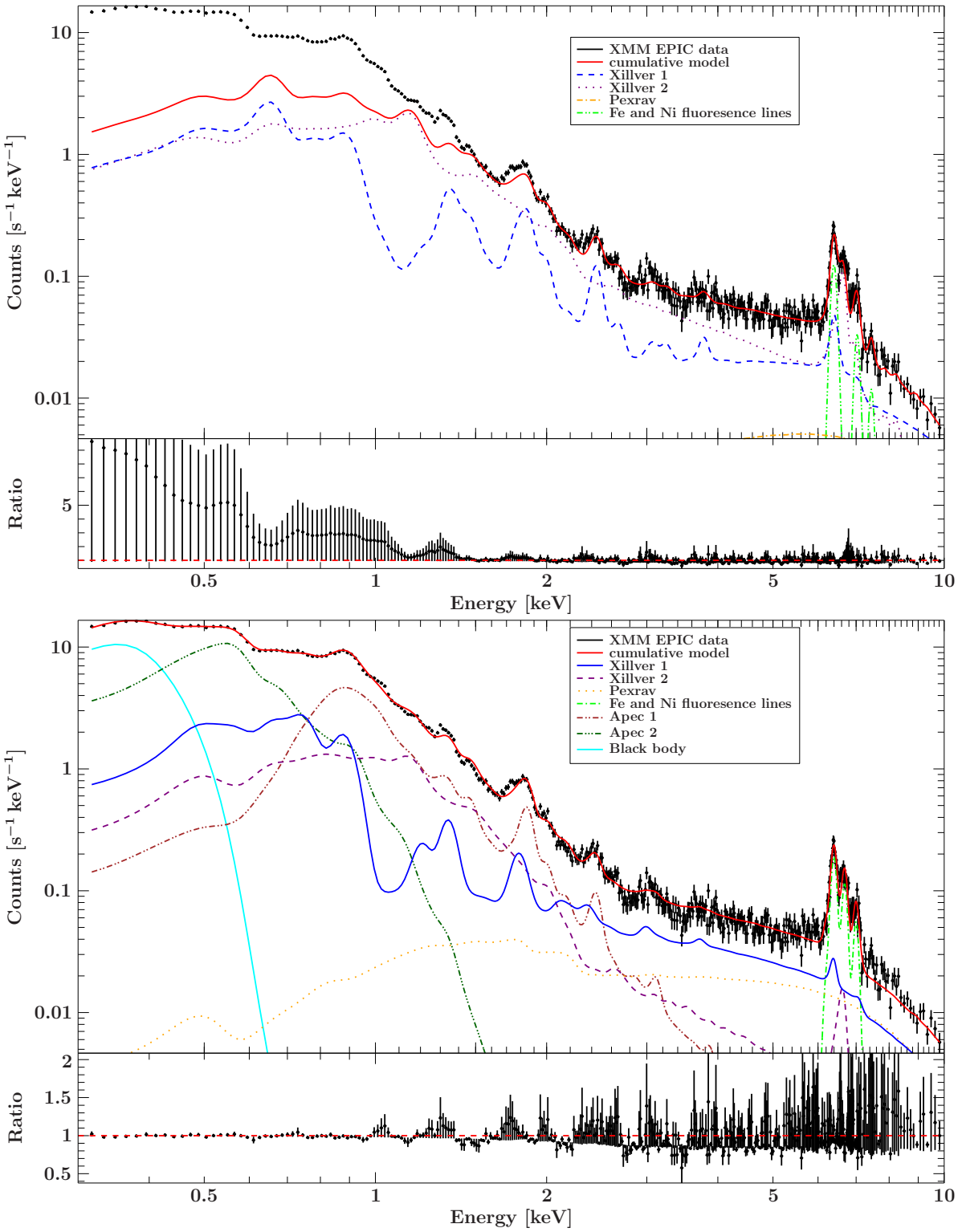

Figure 8.8.: Best-fit of the 0.3–10 keV spectrum of NGC 1068, for the reflection model (upper panel) and the mixed model, with both scattered and reflection components (lower panel).

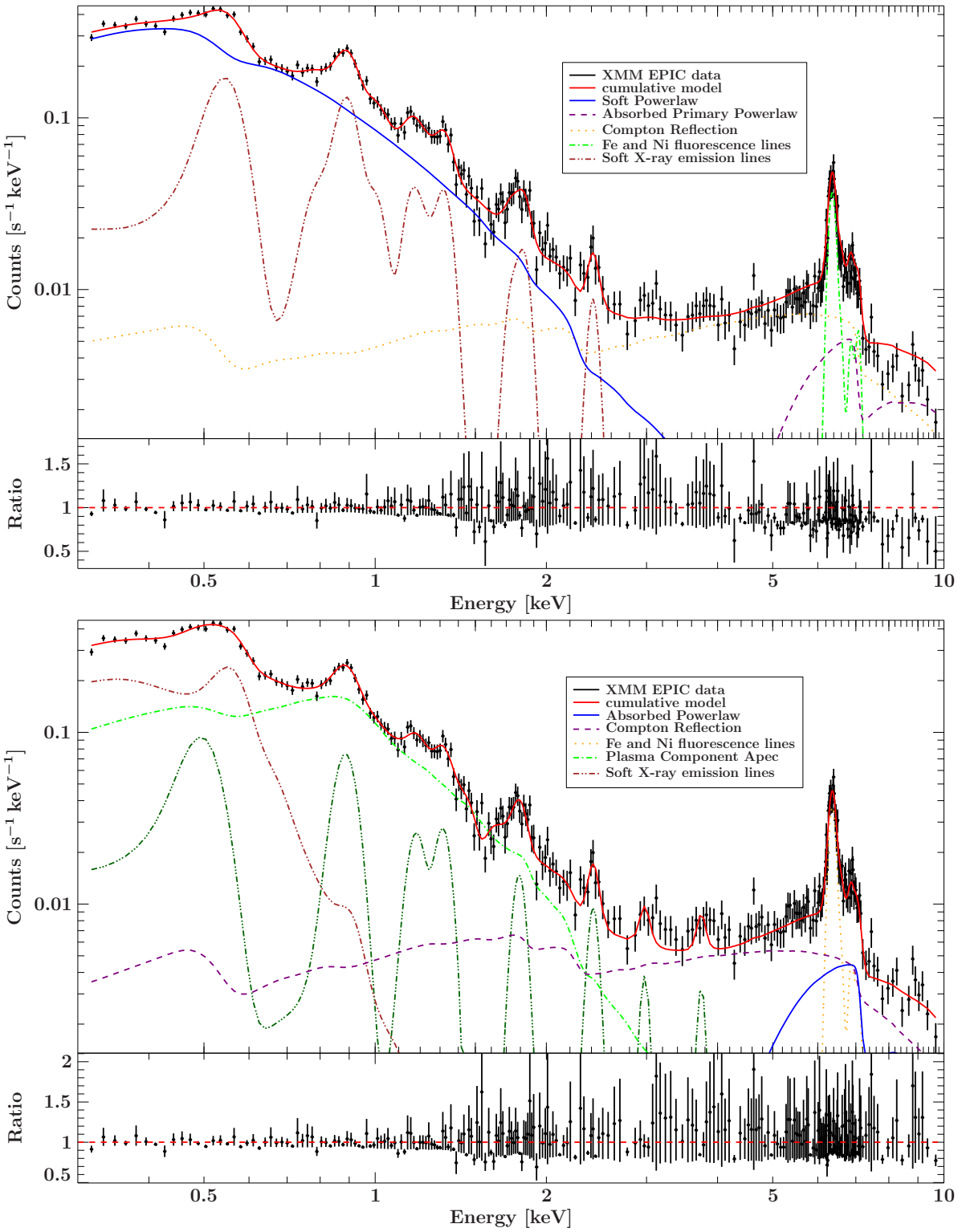

Figure 8.9.: Best-fit of the 0.3–10 keV spectrum of NGC 424, for the phenomenological model (upper panel) and the scattering model (lower panel).

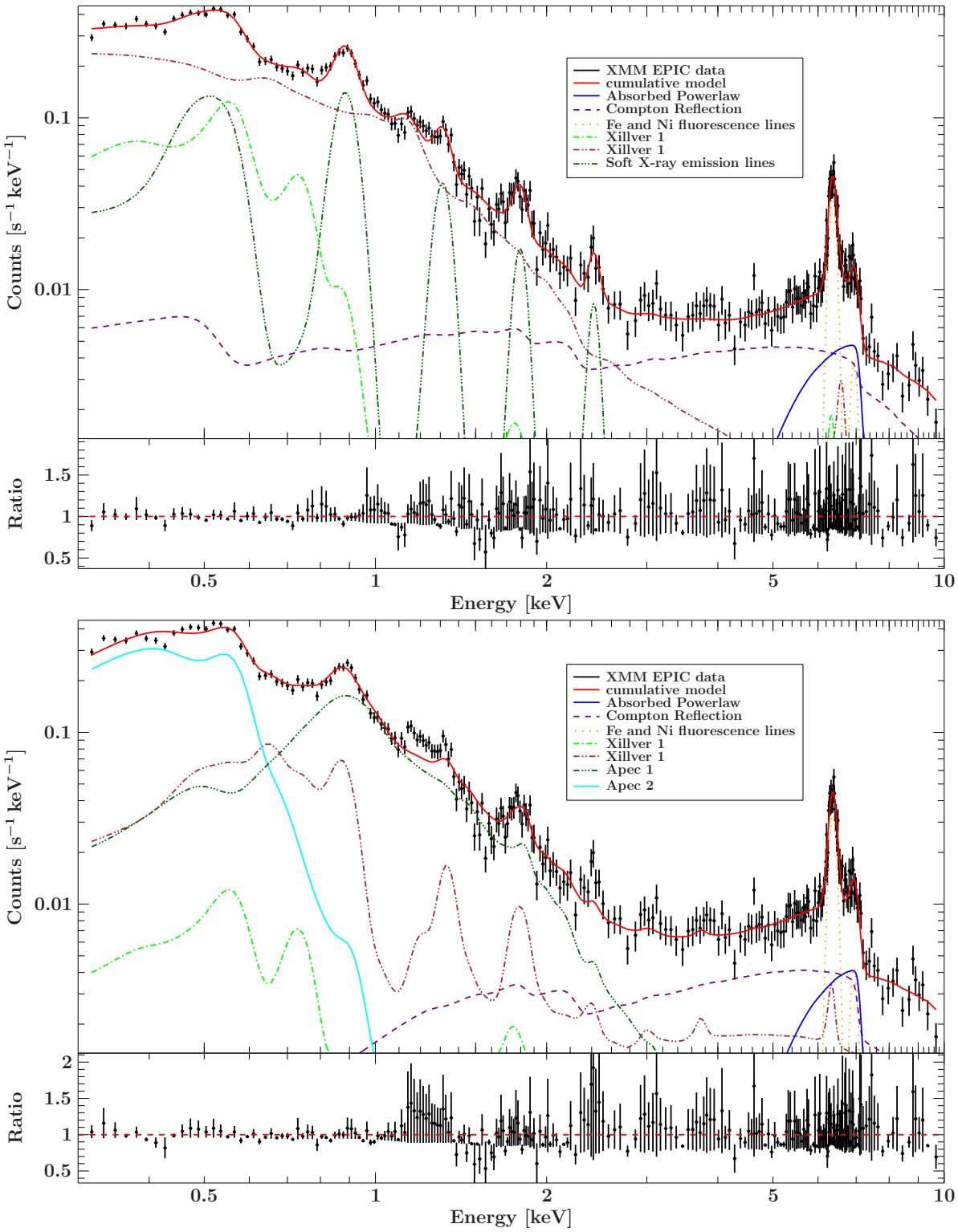

Figure 8.10.: Best-fit of the 0.3–10 keV spectrum of NGC 424, for the reflection model (upper panel) and the mixed model, with both scattered and reflection components (lower panel).

Table 8.3.: Reduced χ^2 (d.o.f.) for each model and source

Source	(A)	(B)	(C)	(D)
Circinus	1.34 (582)	1.43 (597)	2.17 (608)	–
Mrk 3	1.16 (515)	1.12 (531)	1.31 (538)	1.31 (538)
NGC 1068	1.89 (829)	3.09 (861)	272 (849)	2.24 (839)
NGC 424	1.17 (231)	1.26 (234)	1.49 (228)	1.84 (240)

Notes: (A) Phenomenological model (B) Scattering model (C) Reflection model (D) A mixed model, where the best fit includes both `xillver` and `APEC` components.

Table 8.4.: The phenomenological model: Best-Fit parameters

Source	$N_{\mathrm{H,gal}}$ (1)	Γ_{S} (2)	Γ_{H} (3)	A_{Fe} (4)	$N_{\mathrm{H,PL2}}$ (5)	F_{PL1} (6)	F_{PEX} (7)	F_{PL2} (8)
Circinus	$0.43^{+0.05}_{-0.05}$	–	$1.38^{+0.19}_{-0.16}$	$0.79^{+0.20}_{-0.17}$	–	$5.68^{+0.82}_{-0.89}$	$3.81^{+1.00}_{-0.95}$	–
Mrk 3	$0.09^{+0.02}_{-0.02}$	–	$2.06^{+0.23}_{-0.23}$	$0.77^{+0.12}_{-0.11}$	88^{+10}_{-11}	$0.40^{+1.52}_{-0.11}$	$2.29^{+0.18}_{-0.18}$	$2.90^{+0.22}_{-0.23}$
NGC 1068	$0.04^{+0.01}_{-0.01}$	$3.54^{+0.01}_{-0.01}$	2.04^{a}	$1.25^{+0.17}_{-0.15}$	–	$0.98^{+0.03}_{-0.03}$	$3.05^{+0.07}_{-0.07}$	–
NGC 424	$0.07^{+0.02}_{-0.02}$	$3.36^{+0.01}_{-0.17}$	2.00^{a}	$0.76^{+0.28}_{-0.25}$	99^{+61}_{-35}	$0.04^{+0.01}_{-0.01}$	$0.54^{+0.06}_{-0.06}$	$0.14^{+0.06}_{-0.07}$

Notes: (1) Galactic column density in units of $10^{22}\,\mathrm{cm}^{-2}$. (2) Photon index of the soft X-ray powerlaw. (3) Photon index of the primary (hard X-ray) powerlaw. (4) Iron abundance of `pexrav` in solar units. (5) Column density of the compton-thick absorber in units of $10^{22}\,\mathrm{cm}^{-2}$. (6) 0.3-10 keV Flux of the soft X-ray powerlaw, in $10^{-12}\,\mathrm{erg\,cm^{-1}s^{-1}}$. (7) 0.3-10 keV flux of the reflected continuum, in $10^{-12}\,\mathrm{erg\,cm^{-1}s^{-1}}$.(8) 0.3-10 keV flux of the absorbed, incident powerlaw, in $10^{-12}\,\mathrm{erg\,cm^{-1}s^{-1}}$. ^{a} fixed parameter.

neutral as well as ionized emission lines are found, which are consistent with those commonly found in obscured AGN (Guainazzi & Bianchi 2007). The column densities of the global absorber are consistent with the galactic HI values for each source, except for Circinus, which exhibits a higher absorption. The photon indices are consistent with those of the hard X-ray analysis (Chapt. 7). As for the iron abundances, the values of Circinus and NGC 1068 are inconsistent and much lower than those found in Chapt. 7. For these sources the soft X-ray powerlaw extents far into the hard X-ray range ($\geq$ 5 keV). This contribution influences the strength of the Compton-reflection model `pexrav` and the required depth of the iron K-edge.
The photon indices of the soft and hard components could be tied for Circinus and Mrk 3, which suggests that the spectrum solely arises from the reprocession of the primary continuum. NGC 1068 and NGC 424, on the other hand, show a soft excess above the

Table 8.5.: The scattering model: Best-Fit parameters

Source	$N_{\mathrm{H,gal}}$ (1)	Γ (2)	A_{Fe} (3)	$kT_{\mathrm{a\,1}}$ (4)
Circinus	$0.41^{+0.01}_{-0.01}$	1.56^{a}	$0.93^{+0.10}_{-0.09}$	$5.43^{+0.50}_{-0.80}$
Mrk 3	$0.58^{+0.04}_{-0.04}$	$2.01^{+0.14}_{-0.14}$	$0.27^{+0.13}_{-0.12}$	$0.73^{+0.02}_{-0.02}$
NGC 1068	$0.06^{+0.01}_{-0.01}$	$2.50^{+0.01}_{-0.02}$	$0.70^{+0.09}_{-0.10}$	$0.14^{+0.01}_{-0.01}$
NGC 424	$0.13^{+0.02}_{-0.02}$	2.00^{a}	≥ 1.27	$0.83^{+0.05}_{-0.04}$
Source	$A_{\mathrm{a\,1}}$ (5)	$kT_{\mathrm{a\,2}}$ (6)	$A_{\mathrm{a\,2}}$ (7)	$N_{\mathrm{H,PL2}}$ (8)
Circinus	$0.94^{+0.17}_{-0.25}$	–	–	–
Mrk 3	≤ 1.08	$0.061^{+0.001}_{-0.009}$	≤ 5.0	123^{+13}_{-16}
NGC 1068	$0.010^{+0.001}_{-0.001}$	$0.804^{+0.004}_{-0.004}$	$0.095^{+0.003}_{-0.002}$	–
NGC 424	$0.050^{+0.017}_{-0.015}$	$0.113^{+0.007}_{-0.005}$	$0.019^{+0.005}_{-0.004}$	149^{+62}_{-41}

Notes: (1) Galactic column density in units of $10^{22}\,\mathrm{cm}^{-2}$. (2) Photon index (4) Iron abundance of pexrav in solar units. (5) Plasma temperature of `APEC` component 1, in keV. (6) Metal abundance of `APEC` component 1, in units of solar abundance (7) Plasma temperature of `APEC` component 2, in keV. (8) Metal abundance of `APEC` component 1, in units of solar abundance. (9) Column density of the compton-thick absorber in units of $10^{22}\,\mathrm{cm}^{-2}$. ^{a} fixed parameter.

primary powerlaw, indicating an additional emission component, e.g. contribution of a starburst region, as observed in NGC 1068 (Wilson et al. 1992).

8.5.2. Scattering vs. Reflection

As shown in Tab. 8.3, statistically both the scattering and reflection model, as well as their combination are compatible with the data. Apart from NGC 1068 where the pure reflection model is substantially worse, the best-fit values do not allow to distinguish between reflection and emission of a collisional thermal plasma. Though it should be noted that the reflection model gives slightly higher χ^2-values, than the scattering model. In order to evaluate which model is more favorable, a closer look at the model parameters is required.

For each source either a model of a two-temperature plasma, a multi-ionized reflector or a combination of both, as well as additional emission lines, are required to fit the data. In the case of a pure scattering or reflection model, the data is not described to full extend. Despite the additional emission lines, there are residuals, mostly in the transition from one component to another one. This shows that the model, despite all its components, has difficulties to fit all features. Furthermore, the requirement

Table 8.6.: The reflection model: Best-Fit parameters

Source	$N_{\mathrm{H,gal}}$ (1)	Γ (2)	$\xi_{\mathrm{xi\,1}}$ (3)	$A_{\mathrm{Fe,xi\,1}}$ (4)	$\xi_{\mathrm{xi\,2}}$ (5)	$A_{\mathrm{Fe,xi\,2}}$ (6)	$A_{\mathrm{Fe,pexrav}}$ (7)	$N_{\mathrm{H,PL2}}$ (8)
Circinus	$0.75^{+0.01}_{-0.01}$	$1.59^{+0.01}_{-0.01}$	100^{+1}_{-1}	$4.49^{+0.10}_{-0.09}$	1423^{+6}_{-4}	≤ 10	–	–
Mrk 3	$0.19^{+0.01}_{-0.02}$	$1.25^{+0.01}_{-0.01}$	200^{+1}_{-1}	$2.13^{+0.36}_{-0.22}$	1726^{+210}_{-119}	$5.37^{+0.41}_{-0.35}$	–	75^{+11}_{-9}
NGC 1068	$0.07^{+0.01}_{-0.01}$	$0.19^{+0.01}_{-0.02}$	100^{+1}_{-2}	≤ 10.13	3707^{+816}_{-180}	≥ 0.03	≤ 10	–
NGC 424	$0.03^{+0.01}_{-0.00}$	2^{a}	$1.5^{+0.1}_{-0.2}$	$6.00^{+3.36}_{-2.53}$	839^{+192}_{-149}	$4.34^{+0.63}_{-0.60}$	≤ 99	96^{+27}_{-23}

Notes: (1) Galactic column density in units of $10^{22}\,\mathrm{cm}^{-2}$. (2) Photon index (3) Ionization parameter of `xillver` component 1, in units of (4) Iron abundance of `xillver` component 1, in solar units. (5) Ionization parameter of `xillver` component 2, in units of $\mathrm{erg\,cm\,s}^{-1}$ (6) Iron abundance of `xillver` component 2, in solar units. (7) Iron abundance of `pexrav` in solar units. (8) Column density of the compton-thick absorber in units of $10^{22}\,\mathrm{cm}^{-2}$. [a] fixed parameter.

of additional emission lines implies that the ion abundances differ from the expected values based on the models. This suggests that of both these models, the reflection and the scattering model, are too simple to describe the origin of the soft X-ray spectrum self-consistently.

As for the scattering model, Circinus Galaxy aside, all sources require a low- ($\mathrm{k}T \sim 0.06\,\mathrm{keV}$) and a high-temperature ($\mathrm{k}T \sim 0.8\,\mathrm{keV}$) plasma component. The metal abundances of these components are only a few percent, except for Mrk 3, where there are only upper limits. As for the hard X-ray component, the iron abundances are not consistent with the phenomenological model, while the photon indices and column densities are comparable. The sub-solar abundances are unusual for AGN. According to evolution models, (e.g. by Ballero et al. 2008), AGN reach solar and super-solar abundances in early states of their evolution due to star formation and starburst. Furthermore, studies of optical and UV emission and absorption lines suggest at least solar metallicities in AGN, (e.g. Hamann & Ferland 1999). Unless these AGN have undergone at least micro merger, with an inflow of gas with sub-solar abundances, it is unlikely to find such low metal abundances. In order to explain the low abundances, high resolution plots of the best-fit scattering models are produced and shown in Fig. 8.11. In this display each emission line is resolved. In the soft X-rays, there is a strong underlying continuum, which is caused by bremsstrahlung of electrons in the plasma. Obviously the resolution of the EPIC PN detector is not sufficient to resolve these emission lines. Hence, they appear as a blend of lines which is mistreated by `APEC` as an unusually strong bremsstrahlung continuum. Thus, despite statistical agreement the scattering of a thermal plasma is not able to give a reasonable description of the soft X-rays. This suggests either, that the two-temperature model is yet too simple, or the collisional plasma plays a minor contribution to the spectrum.

Table 8.7.: Mixed reflection and scattering model:

Source	$N_{\mathrm{H,gal}}$ (1)	Γ (2)	$\xi_{\mathrm{xi\,1}}$ (3)	$A_{\mathrm{Fe,xi\,1}}$ (4)	$\xi_{\mathrm{xi\,2}}$ (5)	$A_{\mathrm{Fe,xi\,2}}$ (6)
Mrk 3	$0.23^{+0.01}_{-0.01}$	$1.21^{+0.01}_{-0.01}$	200^{+1}_{-1}	$1.5^{+0.1}_{-0.1}$	–	–
NGC 1068	$0.37^{+0.02}_{-0.01}$	$3.00^{+0.03}_{-0.05}$	13^{+1}_{-2}	≤ 0.01	6351^{+1857}_{-1645}	$7.4^{+1.2}_{-1.0}$
NGC 424	$0.04^{+0.01}_{-0.01}$	2^{a}	$2^{+796}_{-0.9}$	$1^{+3.0}_{-0.8}$	24^{+9}_{-5}	$0.9^{+2.7}_{-0.5}$
Source	$A_{\mathrm{Fe,pexrav}}$ (7)	$N_{\mathrm{H,PL2}}$ (8)	$kT_{\mathrm{a\,1}}$ (9)	$A_{\mathrm{a\,1}}$ (10)	$kT_{\mathrm{a\,2}}$ (11)	$A_{\mathrm{ap\,2}}$ (12)
Mrk 3	98^{+34}_{-24}	103^{+26}_{-28}	≤ 2.23	≤ 2.1	–	–
NGC 1068	≤ 0.01	-	$0.80^{+0.01}_{-0.01}$	$1.31^{+0.95}_{-0.52}$	$0.11^{+0.01}_{-0.01}$	$0.031^{+0.004}_{-0.003}$
NGC 424	$1.26^{+3.0}_{0.8}$	110^{+42}_{-27}	$0.86^{+0.02}_{-0.03}$	$0.08^{+0.01}_{-0.01}$	$0.01^{+0.01}_{-0.01}$	$0.05^{+0.02}_{-0.01}$

Notes: (1) Galactic column density in units of $10^{22}\,\mathrm{cm}^{-2}$. (2) Photon index (3) Ionization parameter of `xillver` component 1, in units of (4) Iron abundance of `xillver` component 1, in solar units. (5) Ionization parameter of `xillver` component 2, in units of (6) Iron abundance of `xillver` component 2, in solar units. (7) Iron abundance of pexrav in solar units. (8) Column density of the compton-thick absorber in units of $10^{22}\,\mathrm{cm}^{-2}$. (9) Plasma temperature of `APEC` component 1, in keV. (10) Metal abundance of `APEC` component 1, in units of solar abundance (11) Plasma temperature of `APEC` component 2, in keV. (12) Iron abundance of `xillver` component 2, in solar units. ^{a} fixed parameter.

On the other hand, the fits with the pure reflection model show a similar pattern, i.e. it is required to fit one highly ionized and one low-ionized reflection component. In case of NGC 1068 and NGC 424, an additional neutral component is needed to account for the strong iron lines at 6.4 keV. The measured iron abundances, as opposed to the metal abundances that were measured by `APEC` , are super-solar. An exception is the low-ionized component of NGC 1068, for which only an upper limit $A_{\mathrm{Fe}} \leq 10$ exists at 90% confidence level. The reason for the high abundance can also be seen in the high resolution plot of the best-fit models, in Fig. 8.12. The highly ionized component has a very strong reflection continuum and low iron abundances (Sect. 2.2.4). That means, that the highly ionized `xillver` component fits the blend of emission lines as a strong reflection continuum. The low-ionized component is then needed to fit the remaining emission line features of the data, since reflection is not as efficient due to the opacities of the gas itself, and the lines are relatively stronger. Fig. 8.13 shows the effect of different iron abundances on the spectrum for Mrk 3. It displays the resulting spectrum of the best-fit `xillver` component, if only the iron abundance is changed to $A_{\mathrm{Fe}} = 0.5, 1, 10$ in solar values. For the low-ionized spectrum an iron abundance significantly higher than solar predominantly effects the shape of the continuum. It is steeper and exhibits a prominent iron K absorption edge is. Both a high iron abundance

Table 8.8.: Intensities of the emission lines of the phenomenological model

Energy	Interpretation	Circinus	Mrk 3	NGC 1068	NGC 424
0.50	N VII Lyα	–	–	–	$0.74^{0.64}_{-0.70}$
0.56	O VII (f) Heα	–	$12.6^{+0.91}_{-4.3}$	$129.47^{+3.58}_{-4.02}$	$6.40_{-0.94}1.13$
0.57	O VII (r) Heα	–	≤ 0.77	–	–
0.65	O VIII Lyα	–	$4.21^{+0.51}_{-1.02}$	$13.28^{+1.73}_{-1.74}$	–
0.73	Fe XVIII	$3.95^{+4.55}_{-3.58}$	$3.43^{+0.42}_{-1.56}$	$4.159^{+1.44}_{-1.44}$	–
0.77	Fe XVIII	≤ 6.30	≤ 3.84	–	–
0.83	Fe XVII	–	≤ 0.34	$9.68^{+1.32}_{-1.31}$	$0.45^{+1.61}_{-1.65}$
0.87	Fe XVIII 3d-2p	$6.07^{+2.68}_{-4.68}$	–	–	–
0.90	Ne IX (f) Heα	–	$5.28^{+1.56}_{-4.76}$	$47.85^{+3.9}_{-4.86}$	$1.80^{+0.17}_{-0.10}$
0.92	Ne IX (r) Heα	–	≤ 0.47	$11.75^{+3.7}_{-5.59}$	–
0.91	Fe XIX	$5.04^{2.50}_{-1.81}$	–	–	–
1.01	Fe XXI	–	≤ 0.23	–	$0.38^{+0.10}_{-0.09}$
1.02	Ne X Lyα	$5.30^{1.07}_{-0.88}$	$2.82^{+0.23}_{-1.2}$	$20.66^{+1.47}_{-1.47}$	–
1.05	Fe XXI	–	–	$7.18^{+1.29}_{-1.29}$	–
1.14		$1.16^{0.17}_{-0.21}$	–	–	–
1.17		$2.88^{+0.61}_{-0.60}$	–	$9.66^{+0.53}_{-0.57}$	–
1.25	Mg I Kα	$0.83^{+0.70}_{-0.52}$	$0.73^{+0.15}_{-0.15}$	$1.41^{+0.45}_{-0.45}$	$0.38^{+0.08}_{-0.08}$
1.30	Mg I Kβ	–	–	–	$0.15^{+0.08}_{-0.08}$
1.33	Mg XI Heα	$2.96^{+0.53}_{2.71}$	$0.74^{+0.14}_{-0.73}$	$8.33^{+0.42}_{-0.42}$	$0.40^{+0.08}_{-0.08}$
1.44	Fe XXI, FeXXII	$0.80^{+0.36}_{-0.43}$	–	–	–
1.47	Mg XII Lyα	–	–	$1.43^{+0.30}_{-0.30}$	–
1.72	Mg XI	$1.06^{0.30}_{-0.31}$	–	–	–
1.74	Si I Kα	–	–	$1.36^{+0.24}_{-0.24}$	$0.10^{+0.05}_{-0.05}$
1.84	Si XIII (f)	–	$0.51^{+0.11}_{-0.11}$	–	–
1.85	Si XIII (i)	$3.10^{+0.28}_{-0.28}$	–	$5.14^{+0.28}_{-0.28}$	$0.18^{+0.04}_{-0.04}$
2.01	Si XIV Lyα	–	≤ 0.05	$1.16^{+0.20}_{-0.20}$	–
2.01	P I Kα	–	≤ 0.04	–	–
2.31	S I Kα	$0.91^{+0.47}_{-0.47}$	–	$0.74^{+0.20}_{-0.20}$	–
2.43	S XV (f)	–	$0.24^{+0.13}_{-0.13}$	–	–
2.45	S XV (i)	$1.76^{+0.41}_{-0.44}$	≤ 0.11	$2.22^{+0.20}_{-0.20}$	$0.20^{+0.05}_{-0.05}$
2.62	S XVI Lyα	≤ 0.42	–	–	–

Notes: Energy correspond to center line energies in keV, which were fixed during the fit. Line intensities are in units of 10^{-5}photons cm^{-2} keV^{-1} s^{-1}.

and high ionization yield a stronger effect on the strength of the iron emission line features, while the continuum basically remains stable. Thus the high iron abundance may indicate an overestimation of the ionization in order to fit the line blend of the spectrum as a strong continuum. However, overabundance are possible, as described before. The model then predicts at least two or three (in case of NGC 1068 and NGC 424) differently ionized regions, responsible for the Compton-reflection. the neutral and low ionized components most likely coincide with reflection of the inner, visible wall of the

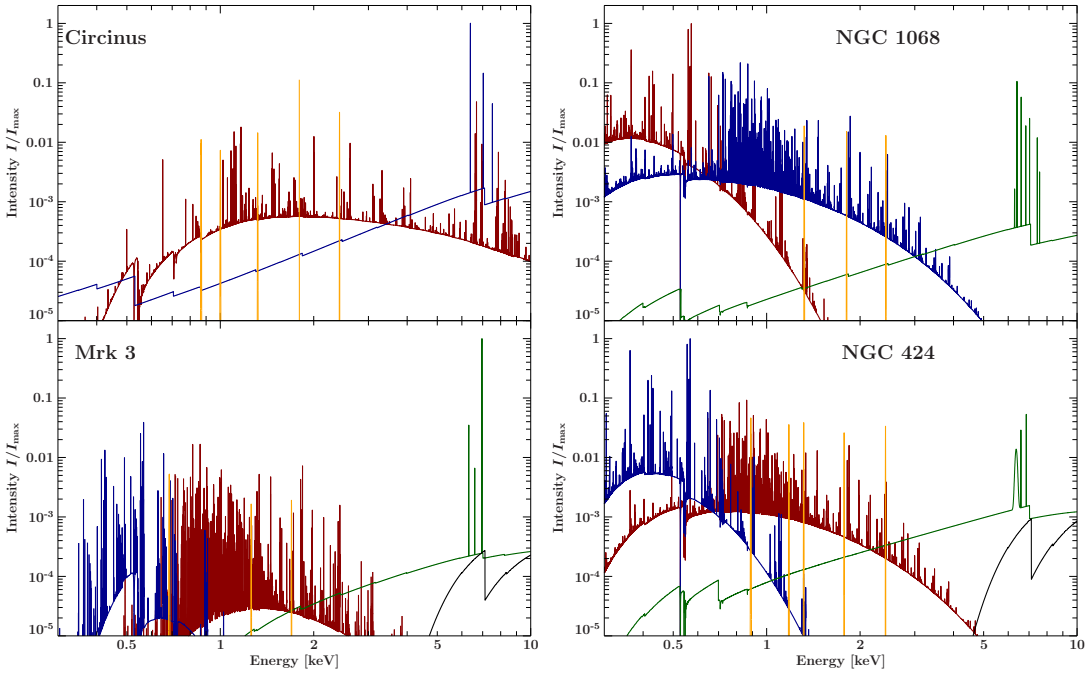

Figure 8.11.: Best-fit scattering models in high resolution ($\Delta E = 1e-3\,\mathrm{keV}$). Dark red: `APEC` 1. Dark blue: `APEC` 2. Dark green: `pexrav` and fluorescence lines of iron and nickel. Black: Absorbed powerlaw. Orange: Additional emission lines.

torus. The origin of the highly ionized component cannot be derived based on this analysis. To estimate its location with respect to the primary X-ray source, a detailed study of the intrinsic luminosity and corresponding densities is required. Also, the remaining emission lines, that were fit individually, suggest the contribution of another ionized component.

The necessity of multiple model components, in both the case of a thermal plasma and the case of (ionized) Compton reflection, support the assumption that the single-phase models (`APEC` , and `xillver`) are too simple to explain the structure of the emission region. Both models assume ionization balance, where heating processes are balanced by cooling processes. According to, e.g. Chakravorty et al. (2008) and Różańska et al. (2008), such a gas lies on the stability curve in the temperature and pressure phase space. The pressure can be parameterized by the ratio of ionization parameter and temperature, which is proportional to the radiation pressure over the gas pressure. In equilibrium, there are configurations, in which multiple states of temperature coexist at the same pressure (multi-phase state). Chakravorty et al. (2009) find that in case of super-solar metallicities, especially of iron and oxygen, the probability of a multi-phase is higher than in the solar or sub-solar case. Hence, even though the analysis does not yield an unambiguous result for the metal abundance, assuming a multi-phase based on the multiple components, suggests at least solar or overabundance of metals.

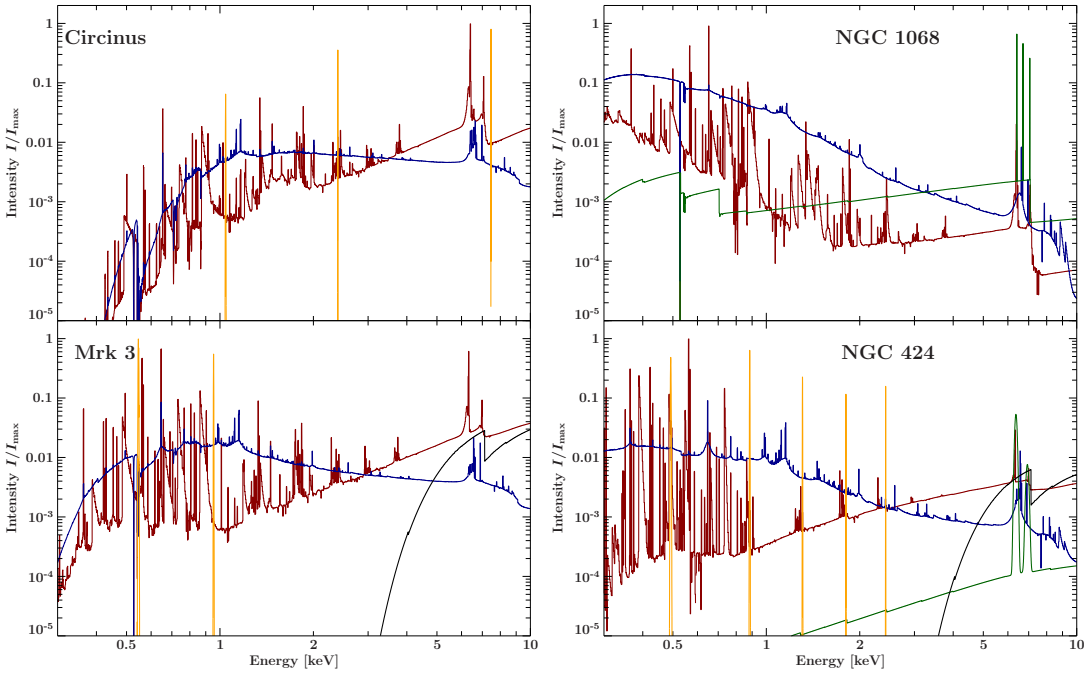

Figure 8.12.: Best-fit scattering models in high resolution ($\Delta E = 1e-3\,\mathrm{keV}$). Dark red: `xillver` 1. Dark blue: `xillver` 2. Dark green: `pexrav` and fluorescence lines of iron and nickel. Red: Absorbed powerlaw. Green: Additional emission lines.

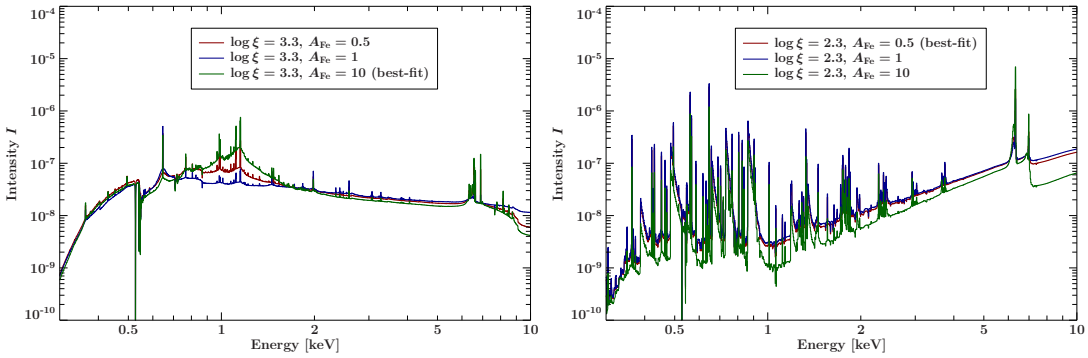

Figure 8.13.: Dependency of the spectrum on the iron abundance for the high-ionized (left panel) and low-ionized (right panel) `xillver` component in the best-fit pure reflection model of Mrk 3. For the `xillver` components, only the iron abundance A_{Fe} is varied, while all other parameters are left at their best-fit values.

The addition of emission lines, required for a best-fit may also indicate that the assumption of ionization balance is not fully correct, and the effect of ionized outflows has to be considered. The equilibrium depends on the shape of the ionizing continuum and chemical abundance (e.g. Chakravorty et al. 2009). Certain lines, especially at 1.0, 1.8, 2.4 keV, which are seen in all spectra, but differ from the intensities predicted by the

models, suggest a different ion abundance than assumed in the equilibrium case, and indicate out-of-equilibrium states.
In conclusion it can be said, that the models used in this analysis, are not able to fully describe the 0.3–10 keV spectrum of the four sources self-consistently. Nevertheless, because of the unreasonable parameter results of the scattering model, the reflection model is more favorable. But it showed that the approach to regard the soft X-rays a a forest of emission lines that does not contribute to the hard X-ray range is too simple. This has consequences for the derived parameters as explained above and it suggests that the regions, responsible for the emission, most likely consist of multiple ionization states or out-of-equilibrium states.

8.5.3. Comparison with published results

Circinus was first observed in X-rays within the *ROSAT*[3] *All Sky survey* (Brinkmann et al. 1994) and found to exhibit a pure Compton reflection dominated spectrum, which was later confirmed with *BeppoSAX* and *ASCA* observations (e.g. Matt et al. 1999, Guainazzi et al. 1999). Furthermore, Circinus is a well-studied *Chandra* and *XMM-Newton* source (e.g. Molendi et al. 2003). The soft X-ray emission was studied by Bianchi et al. (2001) (BMI01, hereafter) and Sako et al. (2000b) (S20, hereafter). Using archival *ASCA* observations S20 found that Circinus can be described by a single low-temperature collisional plasma (`MEKAL` model with $kT = 0.69 \pm 0.05$ keV and fixed solar abundance), or a combination of a low and highly ionized photo-ionized plasma ($\log \xi_{\mathrm{min}} = 0.9^{+0.5}_{-\infty}$ and $\log \xi_{\mathrm{max}} = 3.53^{+0.32}_{-20}$). BMI01 reanalyzed *ASCA* and *BeppoSAX* data in order to test for ionized reflection. Furthermore, they applied a fit equal to the phenomenological model in Sect. 8.1. The energies of the soft X-ray lines detected with *ASCA* could be confirmed by the phenomenological model. In fact, due to the improved resolution of the EPIC PN detector, eight additional lines were detected, which are consistent in line energies with the strongest soft X-ray emission lines, that are observed in RGS spectra of obscured AGN (Guainazzi & Bianchi 2007). Furthermore, BMI01 fit a thermal plasma, using `MEKAL` and find a higher temperature than S20 for sub-solar abundance. The results of the scattering model (Sect. 8.2) is not consistent with either of the collisional plasma models of BMI01 or S20. It should be noted, though, that the scattering model includes a more detailed description of the atomics processes, responsible for the emission. In addition *XMM-Newton* EPIC PN has a better energy resolution that *ASCA* or *BeppoSAX*, thus more features and line blends can be resolved, which influences the fit. However, as described in Sect. 8.5.2, the additional lines, that are required, suggest that the abundances might not be correct and different components than a collisional plasma have to be regarded.
Based on a model produced with CLOUDY, BMI01 studied the soft X-ray contribution of reflection in the spectrum. They require a single mildly ionized reflector, which explains

[3] http://heasarc.gsfc.nasa.gov/docs/rosat/rosat.html

the line spectrum and most of the continuum. They note, however, the existence of an unexplained soft excess, which they relate to a possible region of starburst. Using the reflection model (Sect. 8.3), the spectrum is well described by combination of a mildly and highly ionized reflector with iron over abundance. Solely S XVV and L-emission of Fe XXI–XXII have to be fit as individual lines. This confirms the presence of ionized reflection and suggests a single-ionized reflector is too simple to account for the whole spectrum, but at least two reflectors are responsible.

Mrk 3 was first considered as Compton-thick source by Turner et al. (1997) based on *ASCA* observations. The existence of a cold Compton-thick absorber was confirmed in a series of studies on individual datasets of *Ginga*, *ASCA*, *ROSAT* or *BeppoSAX* (e.g. Sako et al. 2000a, Cappi et al. 1999). Griffiths et al. (1998) performed a composite study on non-simultaneous data from *Ginga*, *ASCA* and *ROSAT*. They discovered evidence on spectral variability in the continuum normalization and, furthermore, in the flux of the iron K α line on a timescale of ~ 3.5 yrs. They conclude that at least a significant contribution of the iron line cannot originate on the neutral torus, but from a region with a dimension less than 0.3 pc. The soft X-ray band was modeled as a blend of a scattered powerlaw continuum, with single emission lines, as well as, with an absorbed continuum and emission lines scattered from a hot photo-ionized region. The first is associated with shock-heated gas from a nuclear starburst region, while the alternative description corresponds to a photo-ionized gas ($\log \xi \sim 2.8$). A subsequent analysis of an *XMM-Newton* observation by Pounds & Page (2005) remark a small blue shift of the Fe Kalpha lien of 30 ± 10 keV. They conclude, based on variability studies of this line, that part of it arises from an outflow on the near-side of the torus (supported by Sako et al. 2000a). This scenario would support a non-equilibrium state as suggested in Sect. 8.5.2. However, a significant blue shift of the line spectrum is not observed in this analysis.
The spectrum below 3 keV was studied based on RGS data by Pounds & Page (2005) as well as Bianchi et al. (2005). The lines detected by the phenomenological fit (Tab. 8.8) are consistent with their findings. Especially, the detection of a strong forbidden O VII line indicates emission from a photo-ionized plasma, in which the rate of collisions is lower than the rate of this forbidden transition. Bianchi et al. (2005) note, that at least two ionized regions are needed to account for the variety of ionization states in the RGS data. This agrees with the conclusion of a multi-phase emission region (Sect. 8.5.2).

NGC 1068 has a long history of observations in the optical, UV and X-rays- First detection of the iron line were obtained with *Ginga* (Koyama et al. 1989). The reflection spectrum was then confirmed by more recent observations with *ASCA* (e.g. Ueno et al. 1994, Iwasawa et al. 1997, Netzer & Turner 1997). In following observations with *BeppoSAX* it was discovered that NGC 1068 shows evidence for the presence of at least two reflectors of different ionization states, based on the presences of both neutral and

H- and He-like iron lines (eg. Matt et al. 1997, Guainazzi et al. 1999). The detection of OVII was further interpreted as evidence for third reflector, (Bianchi et al. 2001).
The source exhibits an extended soft X-ray emission which lies significantly above the reflected component (e.g. Marshall et al. 1993, Ueno et al. 1994 and Brinkman et al. 2002, BK02 hereafter). BK02 discovered that there are two regions in the soft spectrum of NGC 1068, a bright central region coinciding with the region of the hard component, and a fainter more extended region, associated with the ionization cone the source. The soft X-ray spectra of both regions show discrete emission lines from H- and He-like elements, which they found to be consistent with recombination following photo-ionization in warm photo-ionized plasma. This confirms results from Kinkhabwala et al. (2002) (K02, hereafter), who analyzed RGS data of the 0.3–2.5 keV spectrum. A collisional component was earlier suggested by Sako et al. (2000a), based on evidence for jet-outflows with intense shock heating in NGC 1068 (e.g. Wilson & Ulvestad 1982, Goosmann & Matt 2011, Wang et al. 2012). However, K02 excluded contribution of any collisional plasma, which is heated by shocks or jet-like outflows, based on the intensity ratio of the intercombination, forbidden and resonance lines. Furthermore, they observe metal abundance consistent with solar, except for N, Mg and Si. Both these facts speak against the scattering model for NGC 1068, which was questioned based on the low abundances anyway. On the other hand, K02 and BK02 find a broad and flat distribution of ionization parameters ($\log \xi = 0 - 3$), which is consistent with the results of the reflection model. In the scenario of a mixed reflection and scattered emission, the iron abundances found for the ionized reflection components are consistent with solar abundances. Thus, at least part of the ionized emission, solar interpreted as scattering from photo-ionized emission is also consistent with results for ionized reflection. So far, it was not unambiguously distinguished, whether the different ionization parameters results from a radial or density stratification of ionization states. In the mixed model two components of collisional plasma is required, but the results show very low abundances, and an additional blackbody was included to account for remaining residuals below 0.5 keV. Based on the results of K02 and BK02, this may suggest that the contribution of a photo-ionized plasma instead. However, a more detail analysis of the line spectrum is necessary to distinguish between photo-ionized and collisionally ionized plasma.

NGC 424 plays an interesting role among the Compton-thick AGN. It was classified as type I Seyfert galaxy, with evidence of an extended region of high ionization, forbidden optical lines and a broad H β component with $\mathrm{FWHM}_{\mathrm{H}\beta} \sim 3800 \mathrm{km\,s^{-1}}$ (e.g. Boisson & Durret 1986, Murayama et al. 1998). However, X-ray observation of this source show evidence of a heavily obscured continuum and a prominent iron line, favoring a Compton-thick nature with an absorbing column density of $N_{\mathrm{H}} \sim 2 \times 10^{24} \mathrm{cm^{-2}}$ (e.g. Collinge & Brandt 2000, Matt 2000). A *Chandra* and *XMM-Newton* observation by Matt et al. (2003b) revealed an extended soft X-ray and unresolved dominant component in the *Chandra* image. 15% of the soft X-ray emission extended over 5 arcsec, which has a

spectrum consistent with the one of the unresolved component. The 0.5–10 keV spectrum was best described with a cold Compton-reflector, an absorbed primary powerlaw as well as, an absorbed soft X-ray powerlaw with $\Gamma_{\rm soft} \sim 4 \geq \Gamma_{\rm hard}$. Lines for O VII ~ 0.57 keV) and Ne IX ~ 0.9 keV) were detected.
They found that a thermal plasma component cannot explain the soft X-ray spectrum and they find metal abundances of less than 2%. Combining archival *ASCA*, *BeppoSAX* and their *Chandra/XMM-Newton* observations, they conclude that at least two absorber are present: a small-scale Compton.thick one, obscuring the primary X-ray source and a Compton-thin one, associated with a dust lane, observed by *HST* (e.g. Malkan et al. 1998). They further suggest the possibility that the ionized matter coincides with one causing reflection and polarization of photons from the BLR, making it visible from a large inclination angle. Marinucci et al. (2011) (M11, hereafter), studied the RGS and EPIC PN data from 2008, using photoionization models. At least three ionization phases are required for the soft X-ray spectrum, while the hard component is dominated by pure neutral reflection. There is also evidence for iron and nickel overabundance.
The lines detected in the phenomenological fit (Tab. 8.8) are consistent with those found in the RGS data, though, there are more lines resolved in the grating data. The phenomenological fit is thus consistent with earlier observations, confirming the Compton-thick reflector with $N_{\rm H} \sim 10^{24}{\rm cm}^{-2}$ and $\Gamma_{\rm soft} \geq \Gamma_{\rm hard}$. The results of the scattering model are consistent with the thermal model of Collinge & Brandt (2000) and Matt et al. (2003b). They also show a metal abundance of only a few percent. As discussed in Sect. 8.5.2, this might indicate that the model is too simple or the contribution of a thermal plasma is negligible, which is supported by M11. However, the reflection model and M11, require three different ionization phases of the reflector and additional emission of a two-temperature plasma. The contribution of the ionized reflection components to the hard X-ray range is low, but well constrained. Thus, it is possible that at least one of the photoionization phase seen by M11 is consistent with ionized reflection from the inner wall of the torus. Because in the soft X-rays the ionized reflection looks similar to scattering of a photo-ionized plasma, this gives an ambiguous interpretation of the ionized components in the soft X-rays. The additional plasma components with temperatures of $0.86^{+0.02}_{-0.03}$ keV and 0.01 ± 0.01 keV are not consistent with the results for the single-temperature plasma model in M11. Nevertheless, the need for another plasma component might be associated with the extended soft X-ray emission region and possible scattering from the NLR and BLR.

9. Summary and outlook

This thesis presented the systematic study of the 2–10 keV spectrum of 32 Compton-thick AGN, that have been observed with *XMM-Newton* and an additional study of the broad-band spectrum of the four brightest sources of the sample. For this the focus was on comparing two self-consistent descriptions of the 0.3-10 keV range. The main results of the hard X-ray analysis can be summarized as follows.

i) The Compton-thick nature could be confirmed in all of the sources, except for Mrk 231, which was found to be in a Compton-thin state at the time of observation.

ii) The prominent iron line is consistent with fluorescence emission of a neutral Compton-thick absorber. Fluorescence lines of higher ionization states are detected in eleven sources, which suggests a contribution of ionized matter. The equivalent width of the iron line is in good agreement with predictions for Compton-thick AGN. Associating the line width with Doppler broadening corresponds to velocities of $1106 \pm 625\,\mathrm{km\,s^{-1}}$, for well constrained lines. This places the origin of the lines outside the Broad Line Region.

iii) There is a positive trend of the iron line equivalent width against the column density of the Compton-thick absorber. The large scatter of the data is explained by the bias of different ionization states, iron abundances, inclination angles and different contributions of the reflected spectrum that has been absorbed by the Compton-thick matter. The latter, which is mistreated as an absorbed powerlaw by the model, yields that the actual contribution of the primary powerlaw may be smaller than observed and the measured column density can only be regarded as a lower limit. The positive trend itself means, that the iron lines is not seen through the Compton-thick absorber, but is observed directly.

iv) The distribution of the observed total luminosity as a function of redshift demonstrates, that the sample is not yet complete. There appears to be a distinct distribution of sources for which an absorbed powerlaw component is seen in the spectrum. For the same redshift larger than 0.01, these sources are systematically brighter. Since this distribution is not observed for the reflected luminosities, it is concluded that the absorbed powerlaw is the dominant factor of this distribution. However, based on the analysis it cannot be decided to what extend this effect is biased by the incompleteness of the sample or the contribution of the absorbed reflected spectrum. For this, the sample has to be extended and a detailed study of

the primary powerlaw should be attempted. This includes considering supplement data from higher energy ranges. A possibility may offer the recently launched telescope *NuSTAR*, which observes in the 6–79 keV range. Thus, perfectly covering the Compton hump at ~ 30 keV and higher energy ranges, where the primary powerlaw dominates the spectrum.

v) There are indications that the equivalent width of the iron line follows a negative trend as a function of the unabsorbed total luminosity, which is similar to the X-ray Baldwin effect (XBE) of type I AGN. This is the first times this is reported for heavily obscured Seyfert II AGN. A consistency would support the Unified Model, and the fact that type I and II AGN are intrinsically driven by the same engine. Unfortunately, the trend cannot be confirmed quantitatively because of the large uncertainties of the observables. The best-fit parameters, though, are similar to those observed for the XBE. For conclusive results, more sources have to be taken into account, with better quality data. In order to minimize the uncertainties of the equivalent width and luminosity a careful study of the different contributions for the continuum in the hard X-ray spectrum should be performed.

The main results of this analysis are, that a significant contribution of the Compton-reflection arises from neutral matter outside the BLR, which is consistent with the assumption that reflection takes place at the inner visible wall of the neutral torus. Furthermore, there is a bias of the contribution of the absorbed reflected spectrum which has to be considered when measuring the column density of the reflector or strength of the primary continuum. After the hard X-ray analysis, the four brightest sources, were analyzed in the complete 0.3–10 keV spectrum in order to study the origin of the ionized emission lines of iron and to find a self-consistent description of the broad-band spectrum. The results are the following:

i) All spectra are well described by a Compton-reflection component with both neutral and ionized fluorescence lines for the hard component. For two sources, the absorbed powerlaw is detected. The soft X-ray spectrum can be well modeled as a blend of a soft powerlaw and single narrow emission lines. In two cases, Circinus and Mrk 3, the photon indices of the soft and hard component can be linked, thus, indicating that the whole spectrum can be explained by the reprocession of the primary continuum. In the other two cases, additional emission has to be taken into account.

ii) Both the pure scattering and reflection model have problems to account for all the features of the spectrum, even though statistically the fit is good. In comparison, the scattering model is less favorable, because it yields unusually low metal abundances. On the contrary, the reflection model yields iron abundances, which are systematically higher than solar values. Both cases may be indicators that the models are too simple and the unusually low or quite high abundances demonstrate,

that the model tries to compensate this by an overestimation of the continuum. However, since super-solar abundances have been observed in AGN, the reflection model, may be preferred. For the sources, NGC 1068 and NGC 424, for which the soft photon index is not consistent with the one of the hard component, the best fit requires both reflection and scattering components. In comparison with previous work, the reflection scenario is possible to account for part of the observed ionized emission lines, at least in NGC 1068 or NGC 424.

iii) At least two components of a thermal plasma with different temperatures and/or reflection with different ionization states are required in all sources. The necessity of including single emission lines, suggests that even more ionizations states are responsible for the soft X-ray emission.

The results, suggest that the emission of the soft X-rays originates from matter of different ionization or temperature states, which might be coinciding in a multi-phase region. On the other hand it is also possible that the assumption of an equilibrium state is not applicable. There is evidence for jet-like outflows, or shocks in Mrk3 and NGC 1068. The ambiguity of the results also demonstrates the complexity of the spectrum, and that it cannot be distinguished whether scattering or reflection dominates the emission solely based on this analysis. Applying the best-fit model to the RGS data of the respective sources, may yield better insight in the line intensities and help to differentiate between the two scenarios and in addition use higher order line ratios in order to distinguish between collisional and photo-ionized plasma (Kinkhabwala et al. 2002).
Previous studies favor the case of scattering from a photo-ionized plasma, possibly the Narrow Line Region. Since photo-ionization models and the `xillver` model for ionized reflection present a similar line spectrum, with different contributions of the continuum, it is straightforward to compare these two models in a similar analysis. However, in order to distinguish between photo-ionized scattering, the energy range should be extended to energies larger than 30 keV where the Compton-reflection hump can be unambiguously detected. For this again, one could benefit from the recently launched telescope *NuSTAR*, that provides coverage of the 6–79 keV range with better resolution than current mission in this energy range. Another possibility provides *Astro-H* (Takahashi et al. 2010), which is planned to launch in 2014 and will observe at 0.3–600 keV. Both instrument provide good supplements to the 0.3–10 keV spectrum analyzed in this thesis and in effect help to constraint self-consistent models for the emission in Compton-thick AGN.

Bibliography

Abdo A.A., Ackermann M., Ajello M., et al., 2009, ApJ 707, 727

Akylas A., Georgantopoulos I., Nandra K., 2006, Astronomische Nachrichten 327, 1091

Antonucci R., 1993, ArAA 31, 473

Antonucci R., Hurt T., Miller J., 1994, ApJ 430, 210

Antonucci R.R.J., Miller J.S., 1985, ApJ 297, 621

Arnaud K.A., 1996, ASP Conference Series 101, p17

Baldwin J.A., 1977, ApJ 214, 679

Ballero S.K., Matteucci F., Ciotti L., et al., 2008, A&AP 478, 335

Basko M.M., Sunyaev R.A., Titarchuk L.G., 1974, A&AP 31, 249

Bennett C.L., Halpern M., Hinshaw G., et al., 2003, ApJS 148, 1

Bianchi S., Maiolino R., Risaliti G., 2012, Advances in Astronomy 2012

Bianchi S., Matt G., Iwasawa K., 2001, MNRAS 322, 669

Bianchi S., Miniutti G., Fabian A.C., Iwasawa K., 2005, MNRAS 360, 380

Bianchi S., Piconcelli E., Chiaberge M., et al., 2009, ApJ 695, 781

Boisson C., Durret F., 1986, A&AP 168, 32

Braito V., della Ceca R., Piconcelli E., et al., 2004, Nuclear Physics B Proceedings Supplements 132, 153

Brightman M., Ueda Y., 2012, MNRAS 423, 702

Brinkman A.C., Kaastra J.S., van der Meer R.L.J., et al., 2002, A&AP 396, 761

Brinkmann W., Siebert J., Boller T., 1994, A&AP 281, 355

Cappi M., Bassani L., Comastri A., et al., 1999, A&AP 344

Carter J.A., Read A.M., 2007, A&AP 464, 1155

Cash W., 1979, ApJ 228, 939

Chakravorty S., Kembhavi A.K., Elvis M., Ferland G., 2009, MNRAS 393, 83

Chakravorty S., Kembhavi A.K., Elvis M., et al., 2008, MNRAS 384, L24

Collinge M.J., Brandt W.N., 2000, MNRAS 317, L35

Comastri A., 2004, In: Barger A.J. (ed.) Supermassive Black Holes in the Distant Universe, Vol. 308. Astrophysics and Space Science Library, p. 245

de Rosa A., Panessa F., Bassani L., et al., 2012, MNRAS 420, 2087

den Herder J.W., Brinkman A.C., Kahn S.M., et al., 2001, A&AP 365, L7

Elitzur M., Shlosman I., 2006, ApJL 648, L101

Elvis M., Wilkes B.J., McDowell J.C., et al., 1994, ApJS 95, 1

ESA 2012, XMM-Newton Users Handbook Issue 2.10 available from http://xmm.esac.esa.int/external/xmm_user_support/documentation/uhb/index.html

Fabian A.C., Ross R.R., 2010, SSR 157, 167

Fanaroff B.L., Riley J.M., 1974a, MNRAS 167, 31P

Fanaroff B.L., Riley J.M., 1974b, MNRAS 167, 31P

Felsteiner J., Opher R., 1976, A&AP 46, 189

Ferland G.J., Korista K.T., Verner D.A., et al., 1998, PASP 110, 761

Foster A.R., Ji L., Smith R.K., Brickhouse N.S., 2012, ApJ 756, 128

Fukazawa Y., Hiragi K., Mizuno M., et al., 2011, ApJ 727, 19

García J., Kallman T.R., 2010, ApJ 718, 695

García J., Kallman T.R., Mushotzky R.F., 2011, ApJ 731, 131

García J., Mendoza C., Bautista M.A., et al., 2005, ApJS 158, 68

Georgantopoulos I., 2012, ArXiv e-prints 1204.2173

Ghisellini G., Haardt F., Matt G., 1994a, MNRAS 267, 743

Ghisellini G., Haardt F., Matt G., 1994b, MNRAS 267, 743

Goosmann R.W., Matt G., 2011, MNRAS 415, 3119

Griffiths R.G., Warwick R.S., Georgantopoulos I., et al., 1998, MNRAS 298, 1159

Guainazzi M., Bianchi S., 2007, MNRAS 374, 1290

Guainazzi M., Fabian A.C., Iwasawa K., et al., 2005a, MNRAS 356, 295

Guainazzi M., La Parola V., Miniutti G., et al., 2012, A&AP 547, A31

Guainazzi M., Matt G., Antonelli L.A., et al., 1999, MNRAS 310, 10

Guainazzi M., Matt G., Perola G.C., 2005b, A&AP 444, 119

Guainazzi M., Stanghellini C., Grandi P., 2003, In: Hasinger G., Boller T., Parmer A.N. (eds.) XEUS - studying the evolution of the hot universe., p. 261

Guilbert P.W., Rees M.J., 1988, MNRAS 233, 475

Haardt F., Maraschi L., 1993, ApJ 413, 507

Hamann F., Ferland G., 1999, ArAA 37, 487

Henri G., Pelletier G., 1991, ApJL 383, L7

Houck J.C., Denicola L.A., 2000, In: Manset N., Veillet C., Crabtree D. (eds.) Astronomical Data Analysis Software and Systems IX, Vol. 216. Astronomical Society of the Pacific Conference Series, p. 591

Ikeda S., Awaki H., Terashima Y., 2009, ApJ 692, 608

Iwasawa K., Fabian A.C., Matt G., 1997, MNRAS 289, 443

Iwasawa K., Taniguchi Y., 1993, ApJL 413, L15

Jaffe W., Meisenheimer K., Röttgering H.J.A., et al., 2004, Nature 429, 47

Jansen F., Lumb D., Altieri B., et al., 2001, A&AP 365, L1

Kalberla P.M.W., Burton W.B., Hartmann D., et al., 2005, A&AP 440, 775

Kallman T., 1999, XSTAR: A program for calculating conditions and spectra of photoionized gases, Astrophysics Source Code Library

Kallman T.R., Palmeri P., Bautista M.A., et al., 2004, ApJS 155, 675

Kellermann K.I., Sramek R., Schmidt M., et al., 1989, ApJ 98, 1195

Kellermann K.I., Sramek R.A., Schmidt M., et al., 1994, ApJ 108, 1163

Kinkhabwala A., Behar E., Sako M., et al., 2003, ArXiv e-prints astro-ph/0304332

Kinkhabwala A., Sako M., Behar E., et al., 2002, ApJ 575, 732

Koehler T., Groote D., Reimers D., Wisotzki L., 1997, A&AP 325, 502

Koyama K., Inoue H., Tanaka Y., et al., 1989, PASJ 41, 731

Krolik J.H., 1999, Active galactic nuclei : from the central black hole to the galactic environment, Princeton University Press

Laing R.A., Bridle A.H., 1987, MNRAS 228, 557

Lawrence A., Elvis M., 1982, ApJ 256, 410

Leahy D.A., Creighton J., 1993, MNRAS 263, 314

Levenson N.A., Krolik J.H., Życki P.T., et al., 2002, ApJL 573, L81

Liedahl D.A., Osterheld A.L., Goldstein W.H., 1995, ApJL 438, L115

Magdziarz P., Zdziarski A.A., 1995, MNRAS 273, 837

Maiolino R., Comastri A., Gilli R., et al., 2003, MNRAS 344, L59

Maiolino R., Salvati M., Bassani L., et al., 1998, A&AP 338, 781

Malizia A., Stephen J.B., Bassani L., et al., 2009, MNRAS 399, 944

Malkan M.A., Gorjian V., Tam R., 1998, ApJS 117, 25

Marinucci A., Bianchi S., Matt G., et al., 2011, A&AP 526, A36

Marscher A.P., 2009, ArXiv e-prints 0909.2576

Marshall F.E., Netzer H., Arnaud K.A., et al., 1993, ApJ 405, 168

Matt G., 2000, A&AP 355, L31

Matt G., 2002a, ArXiv e-prints astro-ph/0205164

Matt G., 2002b, MNRAS 337, 147

Matt G., Bianchi S., Guainazzi M., et al., 2003a, A&AP 399, 519

Matt G., Bianchi S., Guainazzi M., et al., 2003b, A&AP 399, 519

Matt G., Brandt W.N., Fabian A.C., 1996a, MNRAS 280, 823

Matt G., Fabian A.C., Ross R.R., 1996b, MNRAS 278, 1111

Matt G., Guainazzi M., Frontera F., et al., 1997, A&AP 325, L13

Matt G., Guainazzi M., Maiolino R., et al., 1999, A&AP 341, L39

Matt G., Guainazzi M., Perola G.C., et al., 2001, A&AP 377, L31

Mewe R., Gronenschild E.H.B.M., van den Oord G.H.J., 1985, A&APS 62, 197

Mewe R., Lemen J.R., van den Oord G.H.J., 1986, A&APS 65, 511

Molendi S., Bianchi S., Matt G., 2003, MNRAS 343, L1

Morgan W.W., 1968, ApJ 153, 27

Mukherjee R., Bertsch D.L., Bloom S.D., et al., 1997, ApJ 490, 116

Murayama T., Taniguchi Y., Iwasawa K., 1998, ApJ 115, 460

Nenkova M., Sirocky M.M., Nikutta R., et al., 2008, ApJ 685, 160

Netzer H., Laor A., Gondhalekar P.M., 1992, MNRAS 254, 15

Netzer H., Turner T.J., 1997, ApJ 488, 694

Nousek J.A., Shue D.R., 1989, ApJ 342, 1207

Page K.L., O'Brien P.T., Reeves J.N., Turner M.J.L., 2004, MNRAS 347, 316

Pearson K., 1900, Phil. Mag. Ser. 5,50, 157

Peterson B.M., 1993, PASP 105, 247

Peterson B.M., 1997, An Introduction to Active Galactic Nuclei, Cambridge, New York Cambridge University Press

Peterson B.M., Ferrarese L., Gilbert K.M., et al., 2004, ApJ 613, 682

Piconcelli E., Jimenez-Bailón E., Guainazzi M., et al., 2004, MNRAS 351, 161

Piconcelli E., Miniutti G., Ranalli P., et al., 2013, MNRAS 428, 1185

Pounds K.A., Page K.L., 2005, MNRAS 360, 1123

Raymond J.C., Smith B.W., 1977, ApJS 35, 419

Rees M.J., 1984, ArAA 22, 471

Rees M.J., Volonteri M., 2007, In: Karas V., Matt G. (eds.) IAU Symposium, Vol. 238. IAU Symposium, p.51

Risaliti G., Maiolino R., Salvati M., 1999, ApJ 522, 157

Rosario D.J., Whittle M., Nelson C.H., Wilson A.S., 2008, MdSAI 79, 1217

Ross R.R., Fabian A.C., Young A.J., 1999, MNRAS 306, 461

Rowan-Robinson M., 1977, ApJ 213, 635

Różańska A., Kowalska I., Gonçalves A.C., 2008, A&AP 487, 895

Rybicki G.B., Lightman A.P., 1979, Radiative Processes in Astrophysics, Wiley-VCH

Sako M., Kahn S.M., Paerels F., Liedahl D.A., 2000a, ApJL 543, L115

Sako M., Kahn S.M., Paerels F., Liedahl D.A., 2000b, ApJ 542, 684

Schneider P., 2008, Einführung in die Extragalaktische Astronomie und Kosmologie, Springer Berlin Heidelberg New York

Severgnini P., Caccianiga A., Della Ceca R., 2012, A&AP 542, A46

Seyfert C.K., 1943, ApJ 97, 28

Smith R.K., Brickhouse N.S., Liedahl D.A., Raymond J.C., 2001, ApJL 556, L91

Strüder L., Briel U., Dennerl K., et al., 2001, A&AP 365, L18

Sutherland R.S., Dopita M.A., 1993, ApJS 88, 253

Takahashi T., Mitsuda K., Kelley R., et al., 2010, In: Society of Photo-Optical Instrumentation Engineers (SPIE) Conference Series, Vol. 7732. Society of Photo-Optical Instrumentation Engineers (SPIE) Conference Series

Tarter C.B., Tucker W.H., Salpeter E.E., 1969, ApJ 156, 943

Turner M.J.L., Abbey A., Arnaud M., et al., 2001, A&AP 365, L27

Turner T.J., George I.M., Nandra K., Mushotzky R.F., 1997, ApJ 488, 164

Ueda Y., Akiyama M., Ohta K., Miyaji T., 2003, ApJ 598, 886

Ueno S., Mushotzky R.F., Koyama K., et al., 1994, PASJ 46, L71

Urry C.M., Padovani P., 1995, PASP 107, 803

Wang J., Fabbiano G., Karovska M., et al., 2012, ApJ 756, 180

White T.R., Lightman A.P., Zdziarski A.A., 1988, ApJ 331, 939

Wilms J., Allen A., McCray R., 2000, ApJ 542, 914

Wilson A.S., Elvis M., Lawrence A., Bland-Hawthorn J., 1992, ApJL 391, L75

Wilson A.S., Ulvestad J.S., 1982, ApJ 263, 576

Yang Y., Wilson A.S., Matt G., et al., 2009, ApJ 691, 131

Zhang K., Wang T.G., Gaskell C.M., Dong X.B., 2013, ApJ 762, 51

Życki P.T., Krolik J.H., Zdziarski A.A., Kallman T.R., 1994, ApJ 437, 597

A. Appendix

A.1. Contour Plots

This section presents the contour plots for the best-fit of phenomenological model in the 0.3–10 keV range. For alle sources the photon index is strongly correlated with the normalization of `pexrav` and the absorbing column density, meaning that a flat highly absorbed continuum can appear as a steep mildly absorbed one. For the iron abundance with respect to the normalization of either Ni Kα or Fe Kβ no strong dependence is observed. Contour lines

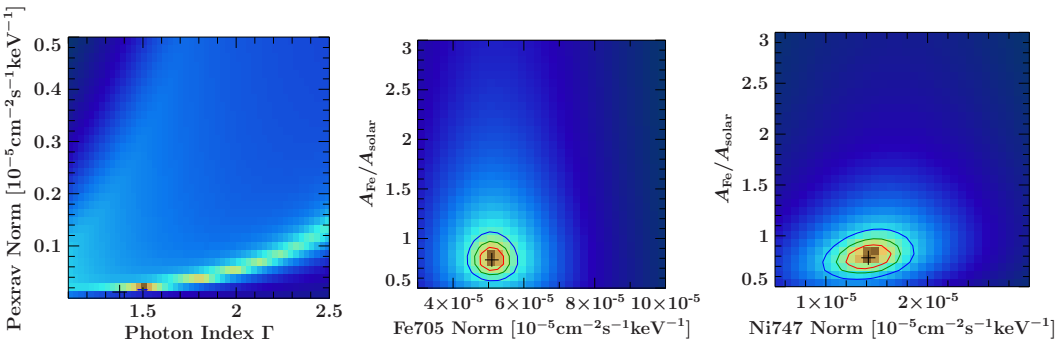

Figure A.1.: Contour plots of Circinus.

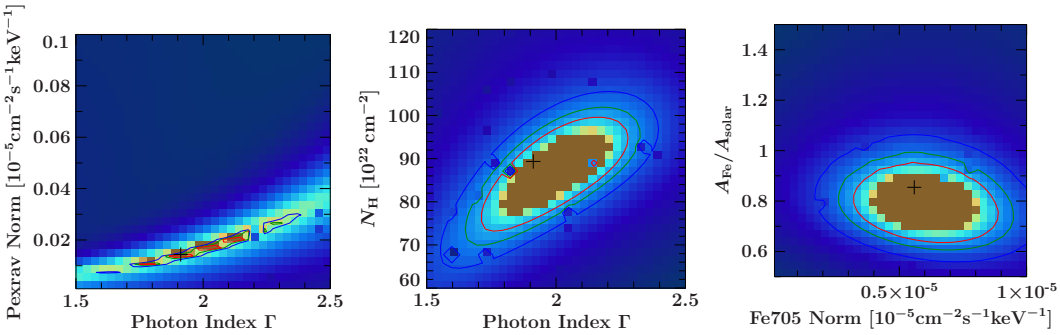

Figure A.2.: Contour plots of Mrk 3

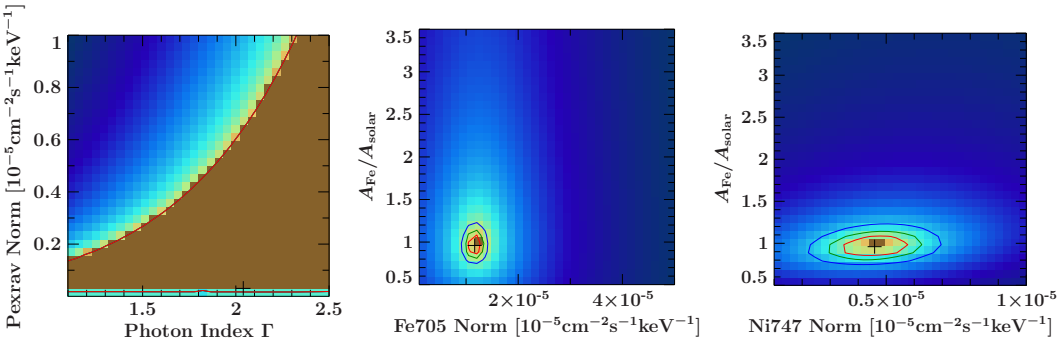

Figure A.3.: Contour plots of NGC 1068

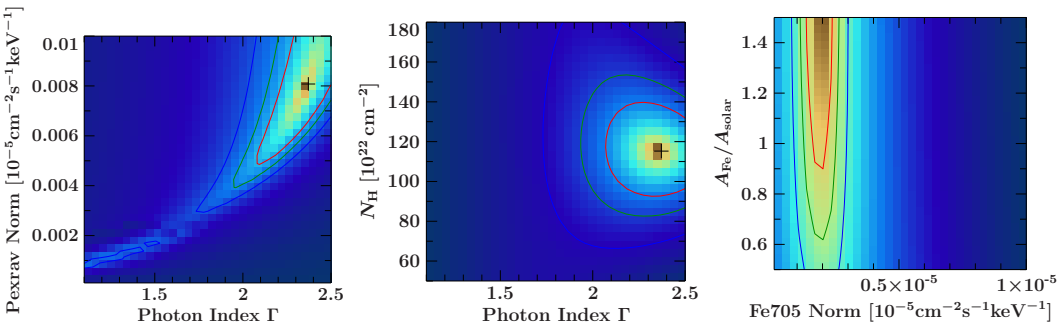

Figure A.4.: Contour plots of NGC 424

A.2. XMM-Newton EPIC PN Spectra

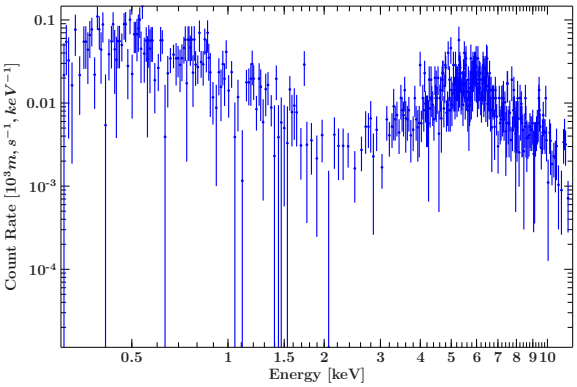

2MASX J1238+0927, ≥ 5 cts/bin

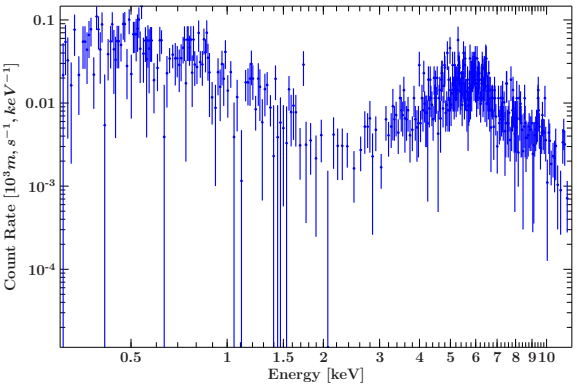

2MASX J11570483_5249036, ≥ 5 cts/bin

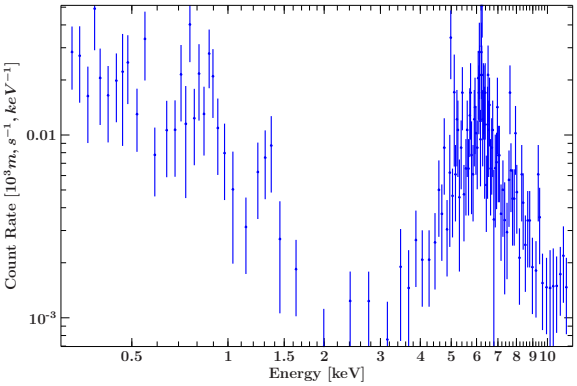

CGCG_218-007, ≥ 5 cts/bin

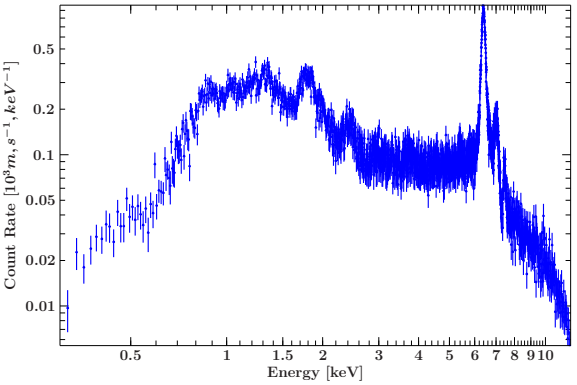

Circinus, ≥ 25 cts/bin

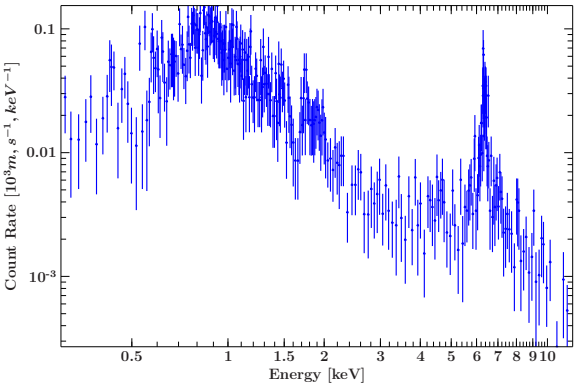

ESO_137-G34, ≥ 5 cts/bin

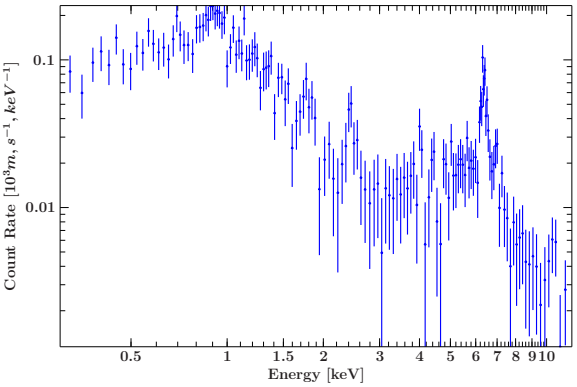

ESO_138-G1, ≥ 25 cts/bin

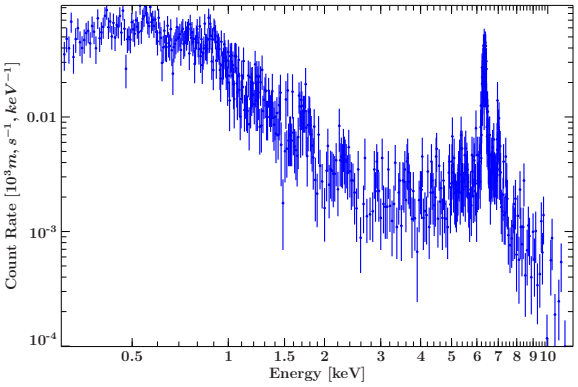

IC 2560, ≥ 5 cts/bin

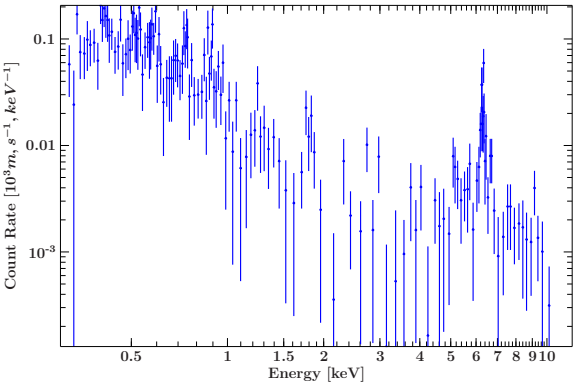

IC 4995, ≥ 5 cts/bin

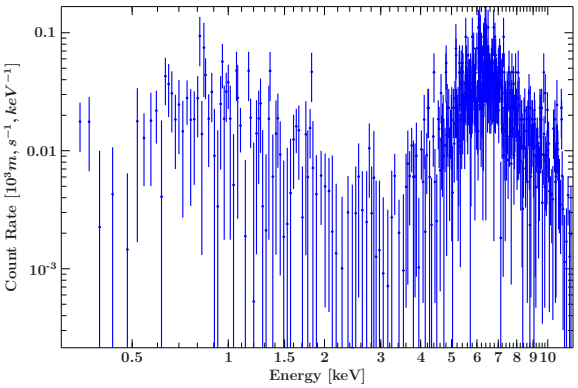

IGR J20286_2544, ≥ 5 cts/bin

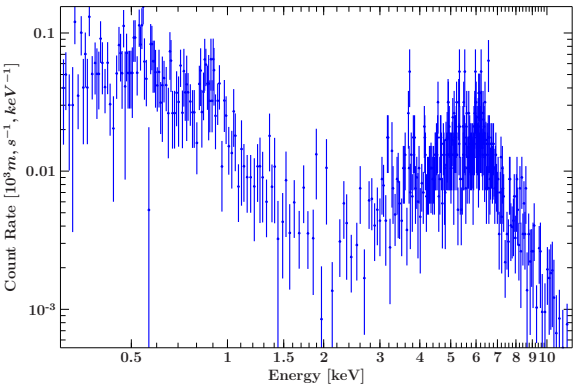

IRAS F08216+3009, ≥ 5 cts/bin

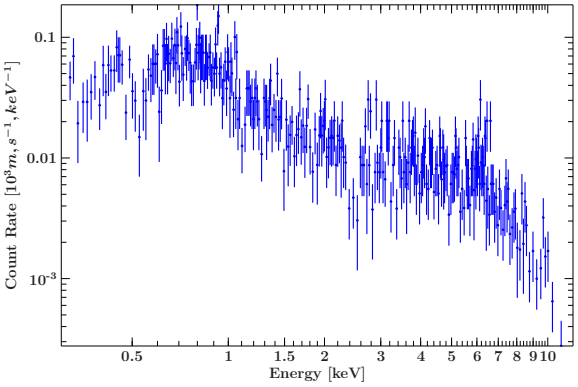

MKN 231, ≥ 5 cts/bin

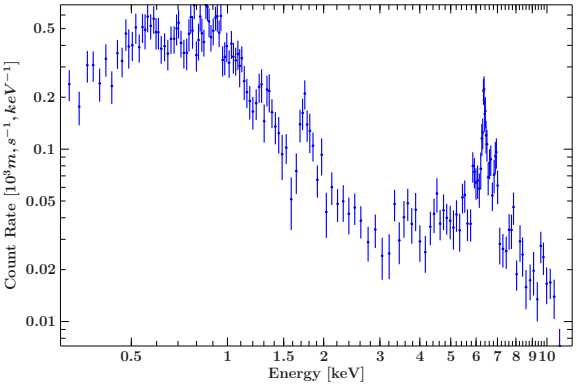

Mrk3, ≥ 25 cts/bin

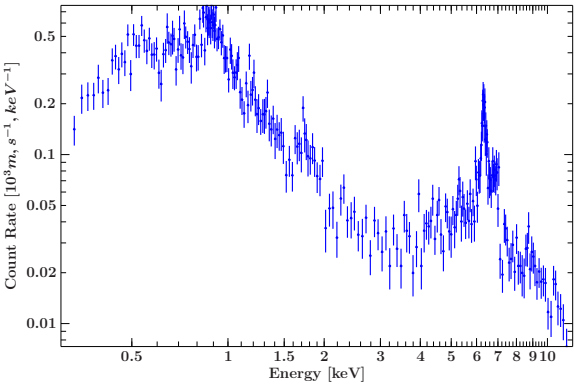

Mrk3, ≥ 25 cts/bin

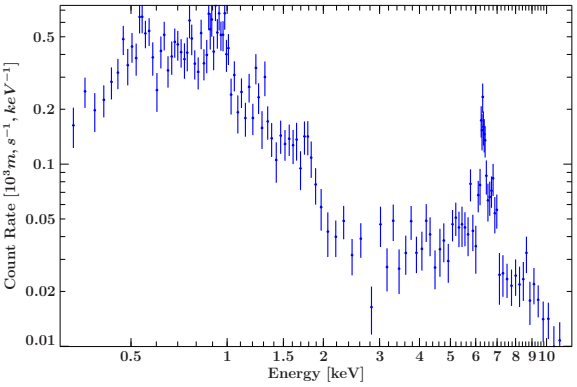

Mrk3, ≥ 25 cts/bin

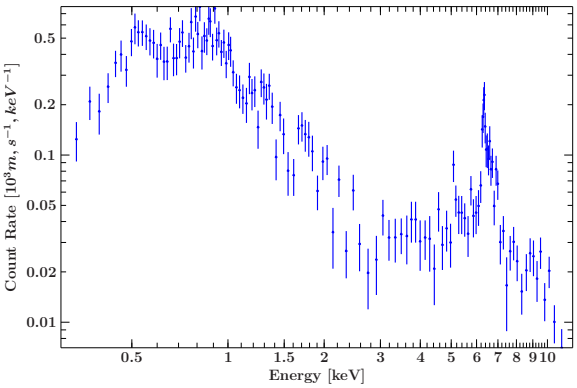

Mrk3, ≥ 25 cts/bin

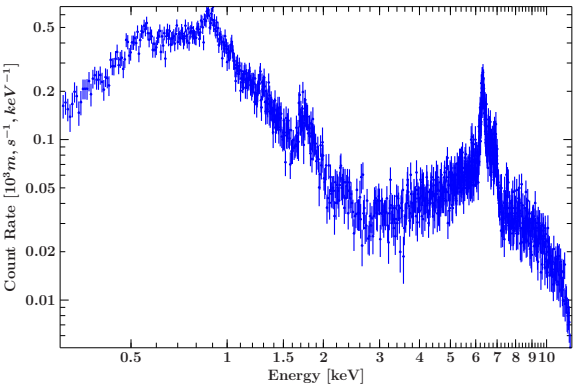

Mrk3, ≥ 25 cts/bin

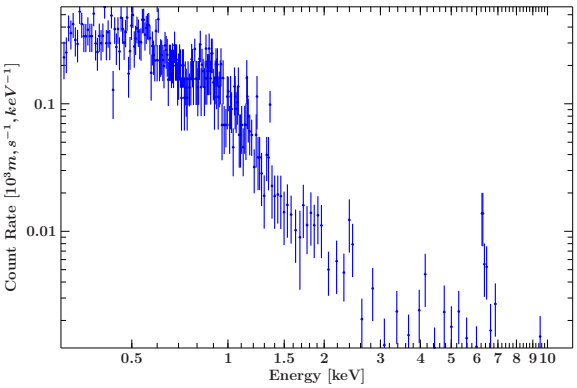

Mrk573, ≥ 5 cts/bin

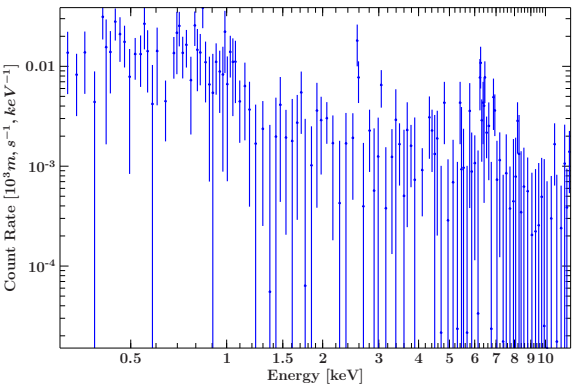

NGC 291, ≥ 5 cts/bin

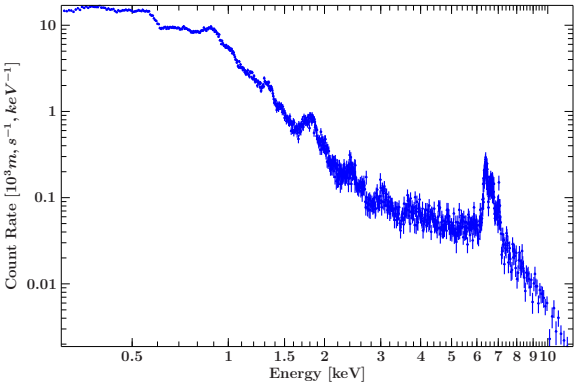

NGC 1068, ≥ 25 cts/bin

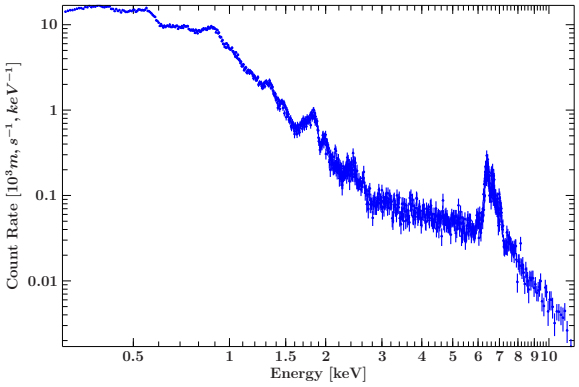

NGC 1068, ≥ 25 cts/bin

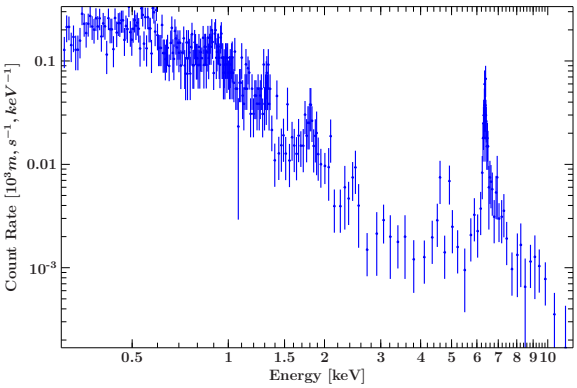

NGC 1320, ≥ 5 cts/bin

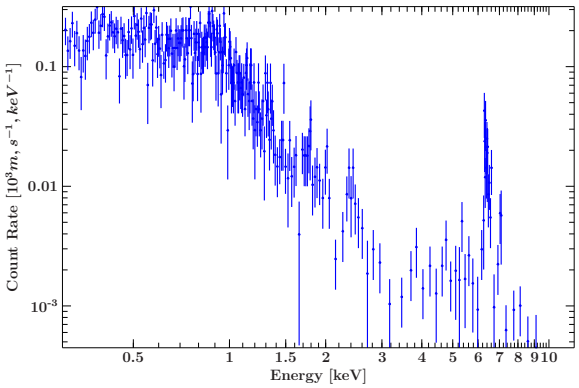

NGC 1386, ≥ 5 cts/bin

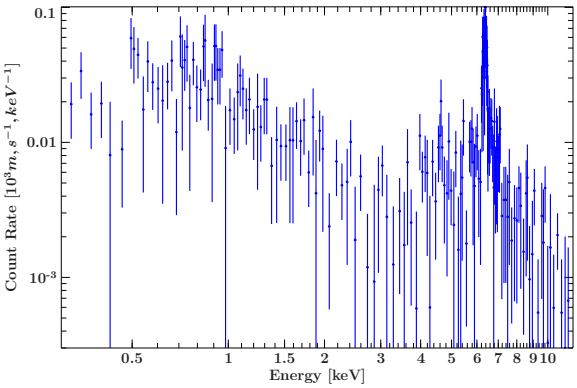

NGC 2273, ≥ 5 cts/bin

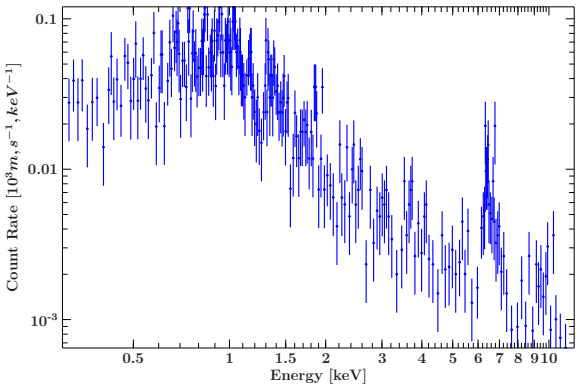

NGC 3079, ≥ 5 cts/bin

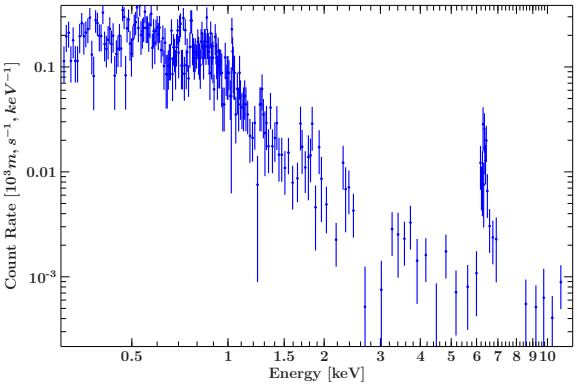

NGC 3393, ≥ 5 cts/bin

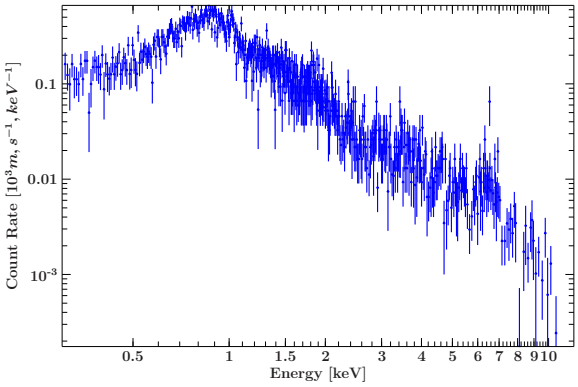

NGC 3690, ≥ 5 cts/bin

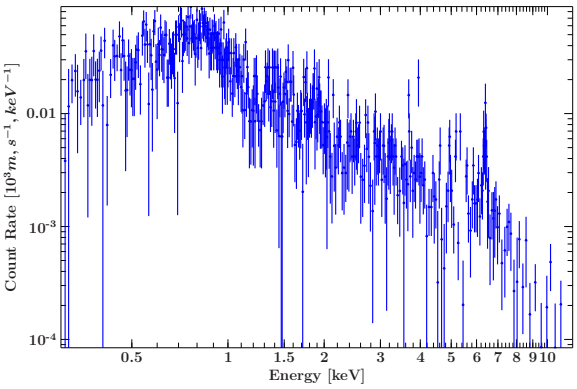

NGC 4666, ≥ 5 cts/bin

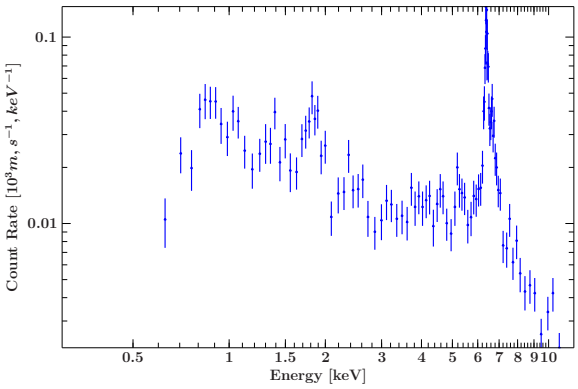

NGC 4945, ≥ 25 cts/bin

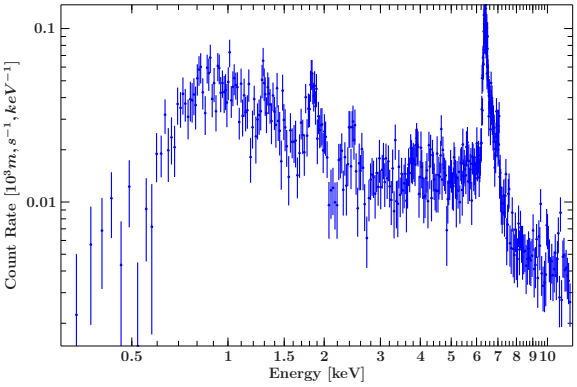

NGC 4945, ≥ 25 cts/bin

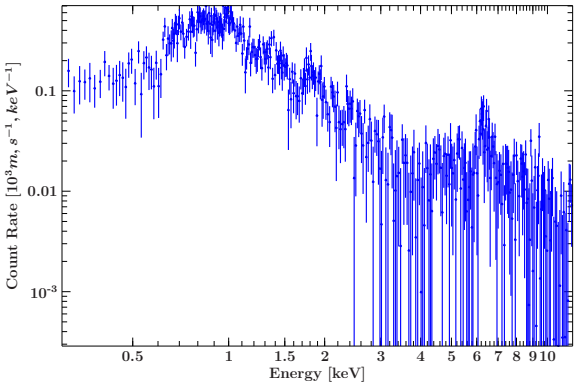

NGC 6240, ≥ 25 cts/bin

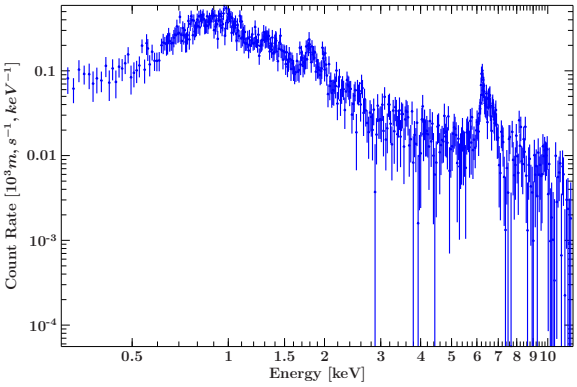

NGC 6240, ≥ 25 cts/bin

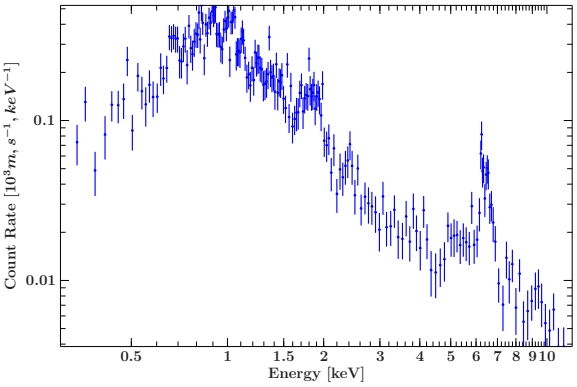

NGC 6240, ≥ 25 cts/bin

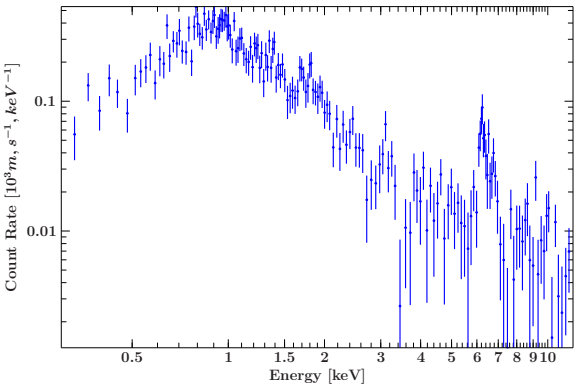

NGC 6240, ≥ 25 cts/bin

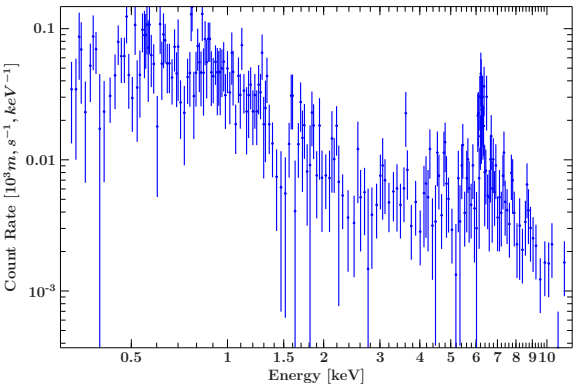

NGC 7212, ≥ 5 cts/bin

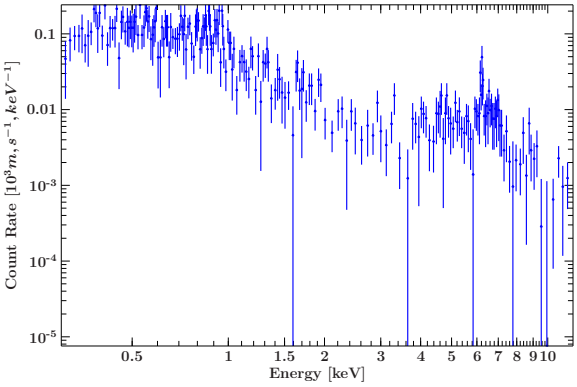

NGC 7674, ≥ 5 cts/bin

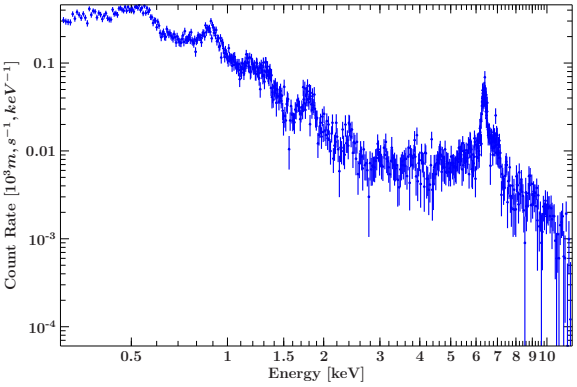

NGC 424, ≥ 25 cts/bin

A.3. Soft X-ray Emission lines

Table A.1.: Emission lines from the X-ray database.

Energy	Interpretation	Energy	Interpretation	Energy	Interpretation	Energy	Interpretation	Energy	Intepretation
0.368	C VI [c]	0.653	O VIII [c]	0.826	Fe L XVII 3d-2p	1.095	Fe XXIII L	2.014	P I [b]
0.395	Ar L XII	0.666	O VII	0.837	O VIII Lyδ	1.096	Fe XXIII L	2.123	Au I [b]1
0.400	Si L XII	0.677	F I [b]	0.845	Fe I L	1.254	Mg I [b]	2.308	S I [b]
0.420	N VI (f)	0.692	Fe XIX L	0.849	Ne I [b]	1.302	Mg I [f]	2.430	S XV (f)
0.425	Ar L XIII	0.698	O VII gamma	0.865	Fe XVIII 3d-2p	1.331	Mg XI (f) [a]	2.447	S XV (i)
0.426	N VI (i)	0.705	Fe I Lα	0.871	O VIII RRC	1.343	Mg XI (i) [a]	2.460	S XV (r)
0.431	N VI (r)	0.711	Fe I L3 2p3/2 edge	0.905	Ne IX (f) [a]	1.344	Mg XI (i) [a]	2.464	S I [f]
0.436	C VI [d]	0.713	O VII delta	0.915	Ne IX (i) [a]	1.352	Mg XI (r) [a]	2.620	S XVI [c]
0.445	Ar L XI	0.715	FeXOY line	0.922	Ne IX (r) [a]	1.473	Mg XII [c]	2.956	Ar I [b]
0.490	C VI RRC	0.719	Fe I Lβ	0.913-0.926	Fe L XIX 3d-2p	1.487	Al I [b]	3.191	Ar I [f]
0.500	N VII [c]	0.726	Fe XVIII 3s-2p	0.965	Fe XX L 3d-2p	1.557	Al I [f]	3.690	Ca I [b]
0.524	O I [b]	0.729	Ca XIX line	1.010	Fe XXI L 3d-2p	1.58	Mg XI [f]	3.861	Ca XIX (f)
0.532	O II [b]	0.739	Fe XVIII 3s-2p	1.022	Ne X [c]	1.740	Si I [b]	3.882	Ca XIX (i)
0.544	O IV [b]	0.739	O VII RRC	1.049	Fe XXI L	1.836	Si I [f]	3.902	Ca XIX (r)
0.546	O IV [b]	0.771	Fe XVIII L 3s-2p	1.053	Fe XXII L	1.839	Si XIII (f)	4.012	Ca 1 [f]
0.561	O VII (f) [a]	0.774	O VIII [d]	1.074	Ne [f] IX	1.854	Si XIII (i)	4.100	Ca XX [c]
0.568	O VII (i) [a]	0.812	Fe XVII L 3d-2p	1.077	Fe XXII L	1.855	Si XIII (i)	5.888	Mn I [b]2
0.569	O VII (i) [a]	0.817	O VIII delta	1.085	Fe XXII L	1.865	Si XIII (r)	5.895	Mn I [b] (avg.)
0.574	O VII (r) [a]	0.819	Fe XVII L	1.085	Fe XXIII L	2.005	Si XIV [c]	5.899	Mn I [b]1

Notes: List of emission lines that were considered in the soft X-ray analysis in Sect. 8.1. [a] Heα, [b] Kα, [c] Lyα, [d] Lyβ, [e] Heβ, [f]. Energies in units of keV.

List of Tables

2.1. Period diagram of AGN classes based on Urry & Padovani (1995) and Antonucci (1993). Also included are Narrow Line Seyfert 1 galaxies (NLS1) and Narrow Emission Line Galaxies (NELG). 10

3.1. List of sources in the XCTA-Sample. For further information about the selection criteria see the text. The list includes source identifications and redshifts, taken from NASA Extragalactic Database (NED, http://ned.ipac.caltech.edu/), as well as information about the extracted observations. This comprises the observation ID number, duration of observation and date. Information about the extraction criteria, i.e. extraction radius, good time intervall filter and final number of counts and exposure time are also given. 30

7.1. Overview: Spectral models 54
7.2. Best-fit continuum parameters 64
7.3. Continuum fluxes and luminosities 65
7.4. Iron Kα line 66
7.5. Neutral emission lines 67
7.6. Ionized emission lines 68
7.7. Results for the X-ray Baldwin effect test 69

8.1. Scattering scenario overview: spectral models 79
8.2. Reflection scenario overview: spectral models 82
8.3. Reduced χ^2 (d.o.f.) for each model and source 95
8.4. The phenomenological model: Best-Fit parameters 95
8.5. The scattering model: Best-Fit parameters 96
8.6. The reflection model: Best-Fit parameters 97
8.7. Mixed reflection and scattering model: 98
8.8. Intensities of the emission lines of the phenomenological model 99

A.1. Emission lines from the X-ray database. 130

Danksagung

In meinem Studium haben mich viele Menschen begleitet und auf die eine oder andere Weise dazu beigetragen, dass ich diese Abschlussarbeit schreiben konnte. An dieser Stelle möchte ich mich bei allen Menschen bedanken, die mich im Studium und in der Zeit der Masterarbeit unterstützt haben. Ein besonderer Dank gilt:

Zunächst möchte ich mich herzlichst bei meinen beiden Betreuern Prof. M. Kadler und Prof J. Wilms bedanken, die mir unermüdlich mit Rat und Tat zur Seite standen. Für das jeweils entgegengebrachte Vertrauen und die motivierenden Diskussionen, die mein Interesse an der Röntgen- und Multiwellenlängenastronomie nur noch verstärkt haben, danke ich sehr und freue mich auf die zukünftige Zusammenarbeit.

At this point I would like to thank my supervisors Matteo Guainazzi and Giovanni Miniutti for giving me the opportunity to work on a joint project during the Students Trainee Project of the European Space and Astronomy Center of ESA. I thank Prof. K. Mannheim and Prof M. Kadler for the support to take part in the Students Trainee Project and the opportunity to continue this project during the master thesis.

I also want to thank all trainees of 2010/2011 for making the Students Project an unforgetable experience. I thank those of you who have become true friends, for the support, motivation and trust.

Des Weiteren möchte ich mich bei den Prof. K. Mannheim, Prof. M. Kadler und Prof. F. Röpke des Lehrstuhls für Astronomie für die interessanten und motivierenden Vorlesungen bedanken sowie der Möglichkeit seit Beginn meiner Studienzeit in Würzburg am Lehrstuhl als Hilfskraft tätig zu sein.

Thomas Dauser und Moritz Boeck danke ich für die Unterstützung und Einführung in ISIS sowie der Beantwortung zahlreicher Fragen und bereitwillige Unterstützung in der Lösung von Problemen.

Letztendlich studiert man nie allein. Daher möchte ich mich bei meinen Freunden und Kommilitonen für die gemeinsame Studienzeit bedanken. Besonderer Dank gilt jenen, die mich, wie selbstverständlich und unermüdlich während und über die Masterarbeit hinaus unterstützt haben: Tobias Beuchert, Marcus Langejahn, Katha Leiter, Sebastian Ohlmann und meinen "A.R.T."-Büro-Mitbewohnern Robert Schulz und Till Steinbring.

Ich danke Selina Storm und Timo Hildebrandt für die Unterstützung während eines Großteils meiner Studienzeit.

Ferner bedanke ich mich bei Prof. W. Duschl, der mir an der Christian-Albrechts-Universität zu Kiel in vielen motivierenden Vorlesungen und Gesprächen die Astronomie näher gebracht hat, und mir ermöglichte im Rahmen einer Miniforschung und Bachelorarbeit erste Erfahrungen in der Forschung zu sammeln. Auöerdem danke ich meinem Lehrer Herrn Albert, der mir zeigte, dass Physik mehr ist als angewandte Mathematik.

Ein herzlicher Dank geht an Janna Klävers und Julia van der Velde für die jahrelange Freundschaft, die gemeinsamen Erlebnisse und dafür, in wichtigen Momenten für mich da zu sein.

Nicht zuletzt danke ich meiner Familie von ganzem Herzen. Ohne die Unterstützung meiner Eltern, würe ein Studium in der Form nicht möglich gewesen. Ich danke für die Liebe, das Vertrauen und Motivation in allen Lebenslagen.

Acknowledgements

This thesis is based on observations obtained with *XMM-Newton*, an ESA science mission with instruments and contributions directly funded by ESA Member States and the USA (NASA).
This research has made use of the NASA/IPAC Extragalactic Database (NED) which is operated by the Jet Propulsion Laboratory, California Institute of Technology, under contract with the National Aeronautics and Space Administration.
This research has made use of the SIMBAD database, operated at CDS, Strasbourg, France.
The data reduction and analysis of the 2–10 keV band in this thesis has been performed under the supervision of Matteo Guainazzi and Giovanni Miniutti during a Students Trainee Project of the European Science and Astronomy Centre of ESA.